

**Evidence for a Complex Order Parameter on the Surface
of (100)-In-plane Oriented $Y_{1-x}Ca_xBa_2Cu_3O_{7-y}$
Superconducting Thin Films From Tunneling Experiments**

**Thesis submitted towards the degree
„Doctor of Philosophy“**

by

Ralph Krupke

Submitted to the Senate of Tel Aviv University

December 1999

Abstract

Tunneling spectra of in-plane oriented (100)- $Y_{1-x}Ca_xBa_2Cu_3O_{7-y}$ /In junctions were studied as a function of temperature, magnetic field and doping. Zero-bias conductance peaks (ZBCP) were observed on optimally doped and underdoped $Y_1Ba_2Cu_3O_{7-x}$ (YBCO), but not on overdoped $Y_{0.8}Ca_{0.2}Ba_2Cu_3O_{7-x}$ (Ca-YBCO). It is shown that the origin of the ZBCP is due to tunneling into Andreev surface bound states with the energy of the bound state determined by the symmetry of the order parameter. On optimally doped YBCO a shifting of the bound state energy from zero to finite value (splitting of the ZBCP) is observed below 6K and is evidence for a spontaneous evolution of a complex order parameter, probably with $d_{x^2-y^2} + is$ or $d_{x^2-y^2} + id_{xy}$ symmetry.

Strong splitting of the ZBCP has been observed if the field is perpendicular to the CuO planes of YBCO ($H||c$). This anisotropy found for the first time, is possibly a support for theoretical explanations of the field splitting due to either a Doppler shift of the bound states energy or to an induced complex order parameter. A sharp crossover to a weak field splitting and hysteresis present at higher fields were not predicted theoretically. We relate the phenomena to vortex dynamics and Zeeman splitting. Problematic for the tested theories is the observation of an anisotropic field enhancement of a sub-gap structure in overdoped Ca-YBCO and the absence of a strong field splitting in underdoped YBCO.

In light of the data a complex order parameter that depends on temperature, doping level and magnetic field has to be considered.

Concerning the YBCO thin film growth, the mechanism for hole formation has been resolved as due to a lack of atomic oxygen. A proper adjustment of the sputtering power and H_2O additive prevents hole formation. A pressure template process was developed to prevent macroscopic growth defects as well. Deposition of YBCO onto CeO buffered Nickel tapes yielded epitaxial c-axis growth of the superconducting layer with high onset transition temperature. Zero resistance however was not achieved due to grain boundaries already present in the substrate.

Preface

All efforts in tunneling spectroscopy are not worth the time, if the quality of the samples, which are analysed, is not high and reproducible. This is not always the case with cuprate superconductors. A great time has therefore been spent to improve the film growth.

The thesis starts with a general introduction into the relevant physics of the cuprates and the impact on tunneling spectroscopy (chapter 1 and 2). The work continues with a presentation of the basics of thin film growth and the sample characterisation tools (chapter 3 and 4), before new insights, which were gained during the optimisation of the growth process are presented, discussed and summarised in chapter 5.

The tunneling spectroscopy data is then presented in chapter 7 after discussing tunneling contacts in chapter 6. Chapter 8 is devoted to the discussion of the tunneling data only, which is finally concluded in chapter 9.

Parts of the work have already been published in the following papers:

- "On the origin of hole formation in YBCO films", R.Krupke, Z.Barkay and G.Deutscher, Physica C 289 (1997) 146-150
- "A systematic approach to reduce macroscopic defects in c-axis oriented YBCO films", R.Krupke, Z.Barkay and G.Deutscher, Physica C 315 (1999) 99-106, Physica C 317-318 (1999) 536-539
- "Anisotropic Magnetic Field Dependence of the Zero-Bias Anomaly on In-Plane Oriented [100] $Y_1Ba_2Cu_3O_{7-x}$ / In Tunnel Junctions", R.Krupke and G.Deutscher, Phys. Rev. Lett. 83 (1999) 4634-4637
- "Spontaneous and Field Enhanced Sub-Gaps in In-Plane Oriented (100) $Y_{1-x}Ca_xBa_2Cu_3O_{7-y}$ / In Tunnel Junctions", R.Krupke and G.Deutscher, J. Low. Temp. Phys. (2000)

This work was carried out under the supervision of Prof. Guy Deutscher.

Table of Contents

| | |
|---|-----------|
| 1 INTRODUCTION | 6 |
| 1.1 PHASE DIAGRAM OF $Y_1BA_2CU_3O_7$ | 6 |
| 1.2 $D_x^2-y^2$ -WAVE SYMMETRY AND BOUND STATES..... | 7 |
| 1.3 COMPLEX ORDER PARAMETER SCENARIO..... | 11 |
| 2 THE DIFFERENTIAL CONDUCTANCE SPECTRUM | 14 |
| 2.1 ISOTROPIC ORDER PARAMETER | 14 |
| 2.2 ANISOTROPIC ORDER PARAMETER | 18 |
| 3 FUNDAMENTALS OF YBCO THIN FILM DEPOSITION | 25 |
| 3.1 THE STRUCTURE OF $Y_1BA_2CU_3O_{7-\delta}$ | 25 |
| 3.2 EPITAXIAL GROWTH..... | 27 |
| 3.3 SPUTTERING | 30 |
| 3.4 THE SPUTTER SYSTEM..... | 30 |
| 4 CHARACTERISATION TOOLS | 32 |
| 4.1 RESISTANCE VS. TEMPERATURE | 32 |
| 4.2 INDUCTIVE Tc MEASUREMENT..... | 33 |
| 4.3 X-RAY DIFFRACTION | 33 |
| 4.4 SCANNING ELECTRON MICROSCOPE (SEM) | 35 |
| 4.5 ENERGY DISPERSIVE X-RAY ANALYSIS (EDAX) | 35 |
| 4.6 ATOMIC FORCE MICROSCOPE (AFM)..... | 36 |
| 5 SAMPLE PREPARATION | 37 |
| 5.1 C-AXIS ORIENTED YBCO FILMS..... | 37 |
| 5.2 A-AXIS ORIENTED $Y_{1-x}CA_xBA_2CU_3O_{7-y}$ FILMS..... | 52 |
| 5.3 YBCO ON CEO BUFFERED NI TAPES..... | 58 |
| 6 YBCO TUNNEL JUNCTIONS | 63 |
| 6.1 CEO BARRIER | 63 |
| 6.2 YBCO/AG CONTACT..... | 64 |
| 6.3 YBCO/IN CONTACT | 64 |
| 7 TUNNELING INTO A-AXIS ORIENTED YBCO FILMS | 66 |
| 7.1 TEMPERATURE DEPENDENCE AT $\mu_0H=0T$ | 66 |
| 7.2 MAGNETIC FIELD DEPENDENCE AT $T=4.2K$ | 70 |
| 7.3 TEMPERATURE DEPENDENCE OF THE CROSSOVER FIELD H^* | 79 |
| 7.4 CONDUCTANCE SPECTRA WITH AG CONTACTS ON OPTIMALLY DOPED YBCO..... | 83 |
| 8 DISCUSSION | 87 |
| 8.1 EVIDENCE FOR ELASTIC TUNNELING IN IN/YBCO JUNCTIONS..... | 87 |

| | |
|--|------------|
| 8.2 THE ZBCP IN OPTIMALLY DOPED YBCO: EVIDENCE AGAINST PRESENCE OF MAGNETIC IMPURITIES IN THE TUNNELING BARRIER..... | 88 |
| 8.3 THE FIELD SPLITTING: DOPPLER SHIFTED BOUND STATES OR INDUCED FINITE GAP? | 91 |
| 8.4 THE ZERO-FIELD SPLITTING | 98 |
| 8.5 THE DOPING DEPENDENCE | 100 |
| 9 CONCLUSION..... | 102 |
| 10 REFERENCES | 104 |

1 Introduction

1.1 Phase Diagram of $\text{Y}_1\text{Ba}_2\text{Cu}_3\text{O}_7$

$\text{Y}_1\text{Ba}_2\text{Cu}_3\text{O}_{7-\delta}$ (YBCO) is a ceramic, which belongs to the family of cuprate superconductors. These materials are quasi two-dimensional doped insulators. The basic building blocks are conducting CuO_2 planes separated by insulating layers (see chapter 3.1). The conductivity of the planes changes dramatically with the carrier concentration. By either changing the oxygen concentration, or by partially substituting the rare-earth atom with an atom of lower valence, electrons are attracted from the CuO_2 planes and holes are induced which can carry current. A schematic phase diagram of cuprate superconductors is given in Fig 1.

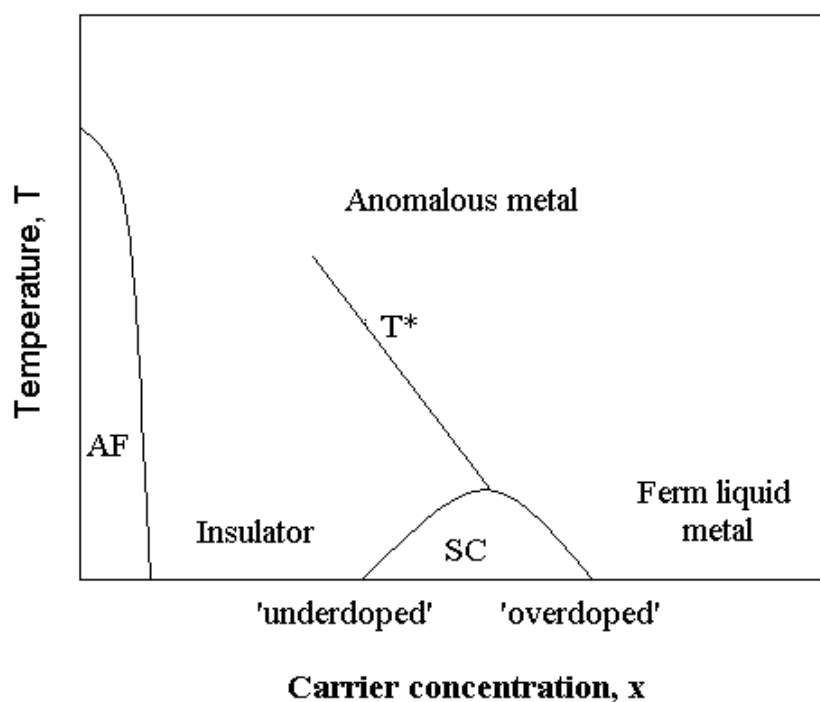


Fig 1: Schematic phase diagram of cuprate superconductors.

In the heavily underdoped regime with low carrier concentration, the cuprates are antiferromagnetic insulators below the Neel temperature. Within a certain doping range cuprates become superconducting below T_c with the highest T_c at 'optimum doping'. At higher temperatures cuprates are so called 'anomalous metals' due to their unusual normal state properties such as the linear temperature dependence of the resistivity and the quasiparticle lifetime. Heavily overdoped cuprates behave like usual Fermi liquid metals with conventional normal state properties, such as a parabolic temperature dependence of the resistivity and the quasiparticle lifetime.

In the weakly underdoped regime an additional temperature scale, T^* , is observed. It is the temperature, below which a gap-like feature, the pseudo-gap, is observed in tunneling spectroscopy and ARPES as well. At similar doping levels, pseudo-gap values have been consistently larger than the energy coherence range measured e.g. by Andreev reflection or penetration depth measurements. Recently it has been proposed by Deutscher [1], to distinguish between a single particle excitation gap, Δ_p , and a coherence, gap Δ_c . In the underdoped regime, the pseudo-gap would be identified as the single particle excitation gap Δ_p , which would be the energy to excite preformed pairs or, more generally, a preformed pairing amplitude at temperatures where phase coherence is not yet established.

In fact strong fluctuation effects are likely to exist in the cuprates, due to the small coherence length, ξ , and the low superfluid density, n_s . In that respect the specific symmetry of the order parameter is however irrelevant.

1.2 $D_{x^2-y^2}$ -Wave Symmetry and Bound States

In many experiments it has been shown that the order parameter of the hole doped cuprates has predominantly $d_{x^2-y^2}$ -wave symmetry [2,3]. However, whether $d_{x^2-y^2}$ -wave symmetry is universal to the cuprate superconductors (SC) or whether the pairing symmetry depends on certain parameters remains an open question and will be discussed later.

$D_{x^2-y^2}$ -wave ordering means that the energy Δ , which is required to remove one electron from the superconductor varies as a function of wavevector as shown in Fig 2. The order parameter is crucial for the identification of the pairing interactions $V_{kk'}$, since they are connected by the general BCS gap equation [4]:

$$\Delta_k = \sum_{k'} \frac{V_{kk'} \Delta_{k'}}{\sqrt{\xi_{k'}^2 + \Delta_{k'}^2}}, \text{ where } \xi_{k'} \text{ is the energy of a quasi-particle in the state } k'.$$

The most basic feature of the superconducting order parameter is that it has an amplitude $|\Delta|$ and a phase φ . In the case of $d_{x^2-y^2}$ -wave ordering, $\Delta(\varphi) = |\Delta| \cos(2\varphi)$, the gap has a maximum in the $\langle 100 \rangle$ and $\langle 010 \rangle$ directions and has nodes in the $\langle 110 \rangle$ direction. At the nodes the phase changes between two discrete values 0 and π , also labeled as + and -, respectively (Fig 6-Fig 13, $\varepsilon=0$).

In a conventional s-wave SC the pairing energy is isotropic and not wavevector dependent.

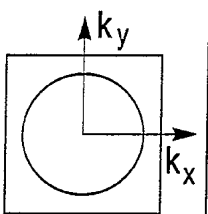
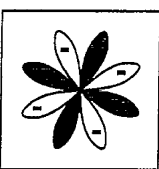
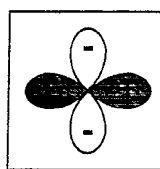
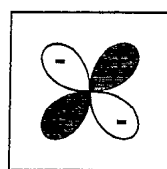
| Group-theoretic notation | A_{1g} | A_{2g} | B_{1g} | B_{2g} |
|---|---|---|--|---|
| Order Parameter basis function | constant | $xy(x^2-y^2)$ | x^2-y^2 | xy |
| Wavefunction name | s-wave | g | $d_{x^2-y^2}$ | d_{xy} |
| Schematic representation of $\Delta(k)$ in B.Z. |  |  |  |  |

Fig 2: Possible even-parity singlet pair states in a square lattice. The lower row is a schematic representation of $\Delta(k)$ in the Brillouin zone with the full lobes $\varphi=0$ and the open lobes $\varphi=\pi$ [3].

The $d_{x^2-y^2}$ -order parameter can be suppressed by the vicinity of a barrier, if the interface is a pair-breaking surface. For the surface to lattice angle $\alpha=0$, the (100)-surface, the gap amplitude is not suppressed by the presence of the wall. This is analogous to the isotropic s-wave case. However as the surface to lattice angle increases the gap amplitude rapidly becomes suppressed in the vicinity of the wall and it completely vanishes at the wall for $\alpha=45^\circ$, the (110)-surface.

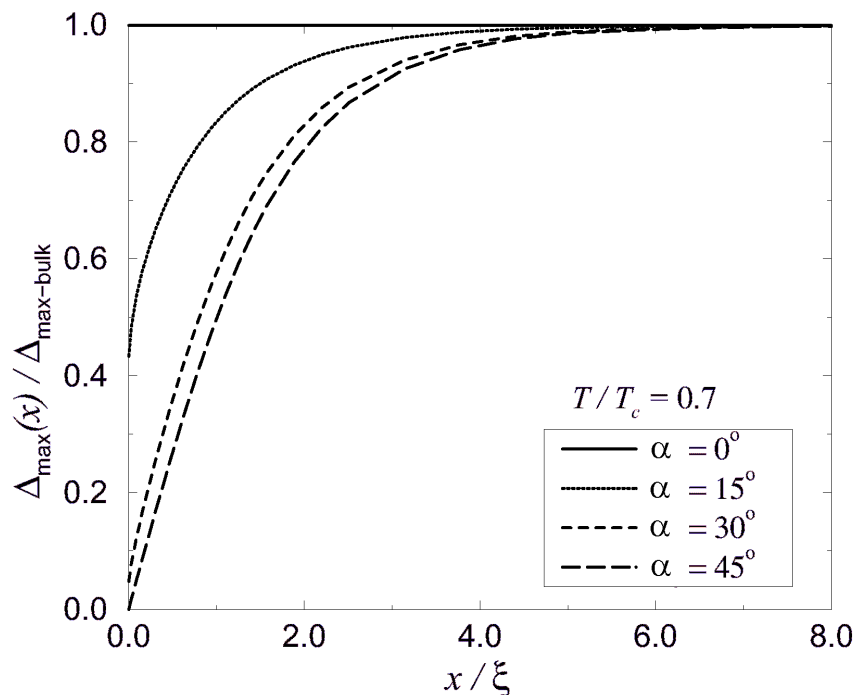


Fig 3: The $d_{x^2-y^2}$ -order parameter amplitude as a function of position for various surface to lattice orientation angles α [5].

Although the amplitude of the order parameter has to be evaluated self-consistently, the angular dependence of the gap suppression can be understood within the framework of the quasiclassical approximation. A quasiparticle approaches the surface along a classical (straight) incoming trajectory θ_{in} and is reflected into the outgoing trajectory θ_{out} . θ is the angle between the trajectory and the surface normal. At a specular surface the outgoing trajectory is fixed by the conservation of parallel momentum (ideal reflection). Surfaces with roughness lead to a statistical distribution of outgoing trajectories. Along the trajectory the quasiparticle experiences the local order parameter. For a surface parallel to one of the crystal axes, e.g. the (100)-surface, the local order parameter is constant along the trajectory because $\Delta(\theta_{in})=\Delta(\theta_{out})$ and the solution of the transport equation along this trajectory is identical to the corresponding solution in the bulk. As a consequence, the self-consistently determined order parameter is identical to the bulk order parameter and therefore not suppressed at a (100)-surface, except for short ξ effects. For any other surface orientation $\Delta(\theta_{in})\neq\Delta(\theta_{out})$, and the self-consistent order parameter will be suppressed at the surface.

A typical trajectory at a (120) surface is shown in Fig 4a). An excitation moving along the trajectory experiences changes in the order parameter due to (i) the depletion of the order parameter at the (120)-surface, and (ii) the change in momentum direction of the excitation when hitting the surface. The change of momentum direction leads in this case also to a sign change of the order parameter as shown in Fig 4b). This is not the case for all trajectories. A sign change of the order parameter occurs only if $\theta > 45^\circ - \alpha$. Fig 5 shows a sketch of the order parameter along the trajectory of the excitation.

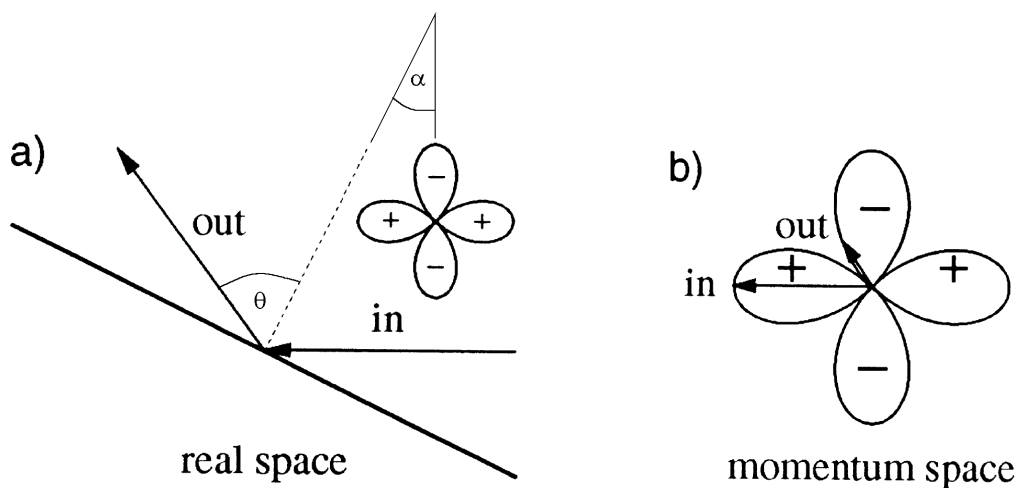


Fig 4: An excitation moving along the trajectory in (a) towards an ideal (120) surface of a $d_{x^2-y^2}$ superconductor. The change of momentum direction leads in this case to a sign change of the order parameter as shown in (b) [21].

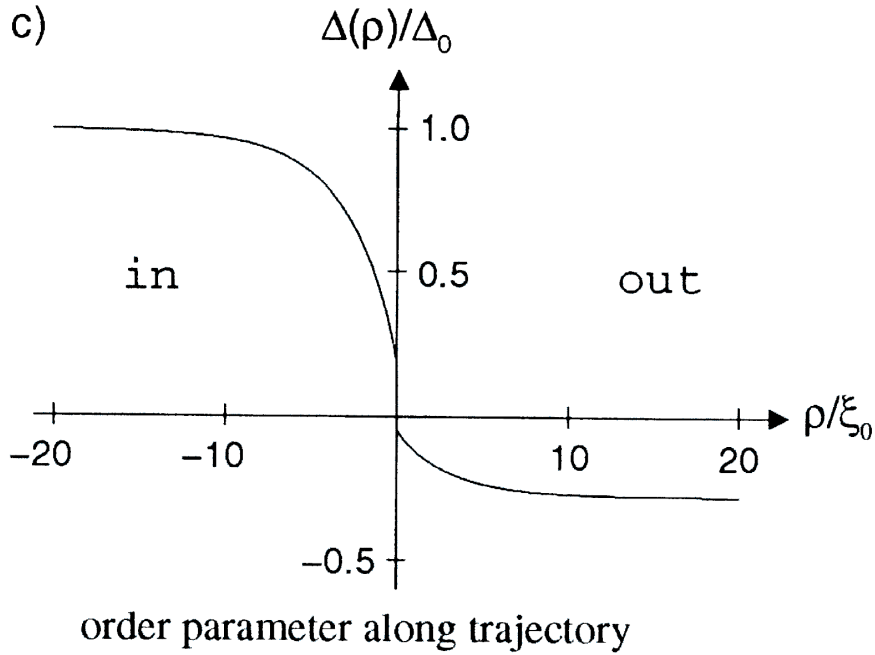


Fig 5: A sketch of the order parameter along the trajectory of the excitation [21].

On a pair-breaking surface, a quasiparticle excitation can be trapped due to multiple Andreev reflection within the region of suppressed order parameter and form a bound state. The energy of the bound state depends on the phase difference between the local order parameter, that the quasiparticle experiences before and after the specular reflection. Kashiwaya et al.[6] have calculated the bound state energy by using a pseudo-quantum well model, in which the excitation is trapped in a normal conducting layer of thickness d_n between two superconductors with different order parameter :

$$-\arctan\left(\frac{\sqrt{|\Delta_1|^2 - E^2}}{E}\right) - \arctan\left(\frac{\sqrt{|\Delta_2|^2 - E^2}}{E}\right) \pm \delta\vartheta + 2\varphi_d(E) = 2j\pi \quad (j, \text{ integer})$$

Here $\delta\vartheta$ is the phase difference between the two superconductors ($\delta\vartheta = \arg[\Delta_1] - \arg[\Delta_2]$). $\varphi_d(E) = md_n E / (\hbar^2 k_f)$ with $d_n \approx \pi \hbar k_F / (m\Delta)$. $+\delta\vartheta$ corresponds to the p-process and $-\delta\vartheta$ to the n-process. If $\delta\vartheta$ is a multiple of π , the bound states for the p-process and the n-process are degenerated.

For $\delta\vartheta = \pi$, the bound state energy is exactly zero, or in other words a zero-energy bound state is formed. This is exactly the case for a quasiparticle trajectory $\theta > 45^\circ - \alpha$. Since the local density of states has peaks at the energy levels of bound states, a zero-energy bound state gives rise to a zero bias conductance peak (ZBCP) in the tunneling spectrum (Fig 17).

1.3 Complex Order Parameter Scenario

1.3.1 Surface Induced Complex Order Parameter

There exist now several experimental results in the literature showing that a $d_{x^2-y^2}$ -wave order parameter can not be universal. Angle resolved photoemission (ARPES) and tunneling on BSSCO [7,8,9] as well as tunneling on YBCO [10] indicate that in a certain range of temperature and doping a small finite gap is present. Since these measurement techniques probe only a surface layer with a thickness of several Ångström, they can not give information about the bulk. Therefore the additional s -wave or id_{XY} -wave component may be present only at pair-breaking surfaces or interfaces.

A theoretical framework, which enables to determine if such a surface state is energetically favorable, is provided by the phenomenological Ginsburg-Landau (GL) theory [11].

The starting point of the calculation is the assumption that two order parameters η_1 and η_2 exist. In the calculation of Sigrist and co-authors [12] the two order parameters belong to pairing states of different symmetry, $d_{x^2-y^2}$ and d_{XY} , which are nondegenerate under the tetragonal (D_{4h}) as well as orthorhombic (D_{2h}) crystal field symmetry: i.e., the transition temperature of the two order parameters are different. The crystal symmetry of YBCO is D_{2h} in the superconducting phase. The GL free energy functional of η_1 and η_2 can then be derived as $F=F_1+F_2+F_{12}$ with

$$F_1 = \int d^3x \left[\alpha_i(T) |\eta_i|^2 + \beta_i |\eta_i|^4 + K_i \left| (\vec{\nabla} - i2\pi\vec{A}/\phi_0) \eta_i \right|^2 \right],$$

$$F_{12} = \int d^3x \left[\gamma |\eta_1|^2 |\eta_2|^2 + \delta (\eta_1^{*2} \eta_2^2 + \eta_1^2 \eta_2^{*2}) \right],$$

where $\alpha_i(T) \propto T - T_{ci}$ (T_{ci} , the bare bulk transition temperature of the order parameter η_i) and β_i, K_i, γ , and δ are real phenomenological parameters which contain all of the relevant physical information of microscopic origin. It is assumed that in the bulk only the single component $\eta_1 = u_1 e^{i\phi_1}$ exists, while $\eta_2 = u_2 e^{i\phi_2}$ vanishes for all temperatures. It can then be shown that the only energetically possible values for the relative phase shift $\theta = \phi_1 - \phi_2$ of the two order parameters are $\theta = \pm\pi/2$ and $\theta = 0, \pi$. A state of the form $d_{x^2-y^2} \pm id_{XY}$ ($\theta = \pm\pi/2$) (Fig 6 and Fig 7) has a nodeless quasiparticle excitation gap and would gain more condensation energy than a state like $d_{x^2-y^2} \pm d_{XY}$ ($\theta = 0, \pi$) (Fig 8 and Fig 9) which has nodes

in the gap.

It should be stressed that this calculation has been made only for a surface induced complex order parameter.

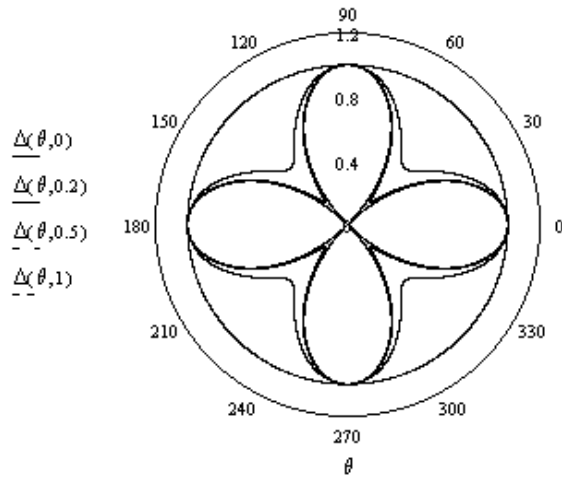


Fig 6: Amplitude Δ of the $d_x^2-y^2+i\epsilon dxy$ OP for $\epsilon=0,0.2,0.5,1$ as a function of angle θ .

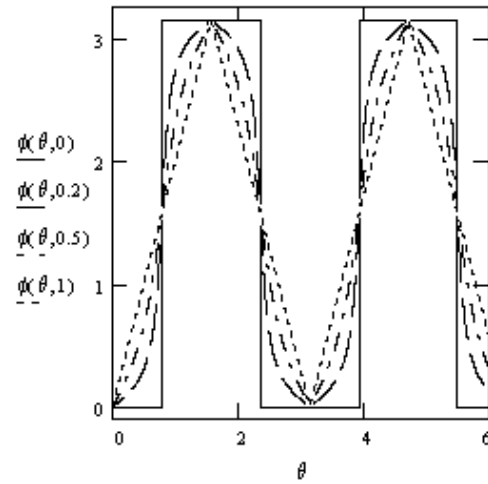


Fig 7: Phase ϕ of the $d_x^2-y^2+i\epsilon dxy$ OP for $\epsilon=0,0.2,0.5,1$ as a function of angle θ .

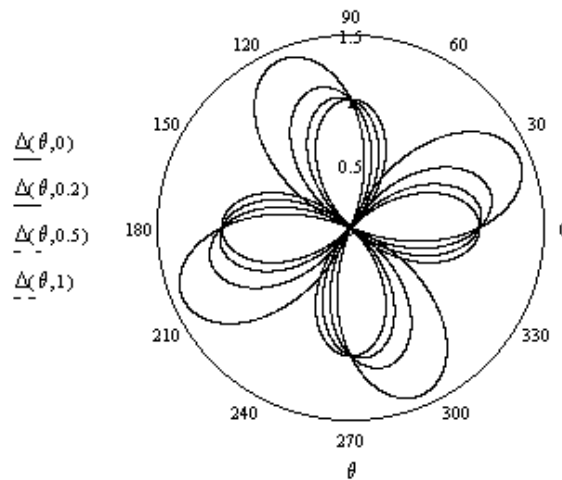


Fig 8: Amplitude Δ of the $d_x^2-y^2+\epsilon dxy$ OP for $\epsilon=0,0.2,0.5,1$ as a function of angle θ .

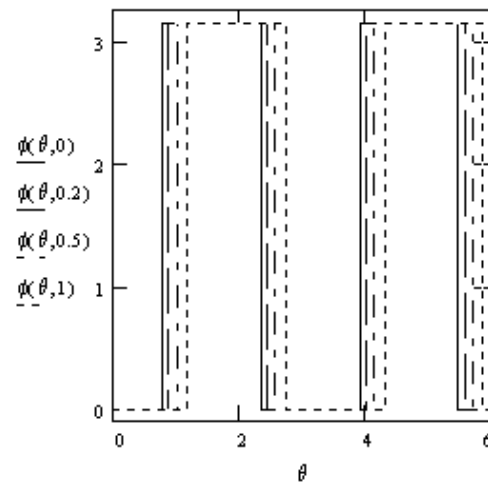


Fig 9: Phase ϕ of the $d_x^2-y^2+\epsilon dxy$ OP for $\epsilon=0,0.2,0.5,1$ as a function of angle θ .

1.3.2 Bulk Complex Order Parameter

So far indications for a complex order parameter in zero magnetic field come from tunneling [7,8,9] and ARPES [10], which are surface sensitive experiments. However the thermal conductivity experiment of Krishana et al. [13] on BSSCO, which probes the bulk, can be explained by magnetic induction of a small id_{XY} superconducting order parameter phased by $\pi/2$ with respect to the principal $d_x^2-y^2$ one to produce a finite gap [14]. Since this experiment measures the bulk it can not be due to a surface effect. Another experiment, which would be consistent with a bulk complex order parameter, is STM data taken on the c-axis

surface of YBCO single crystal [15]. A finite gap in the tunneling spectra has been observed at the center of a vortex, something that would not be expected for pure $d_{x^2-y^2}$. Although this measurement is surface sensitive, the origin of the finite gap must be in the bulk since the measured c-axis surface is not pair breaking.

The important difference between the two ‘bulk’ experiments and the ‘surface’ experiments is that the ‘bulk’ experiments probe a finite gap in magnetic field while the ‘surface’ experiments measure a finite gap in zero magnetic field.

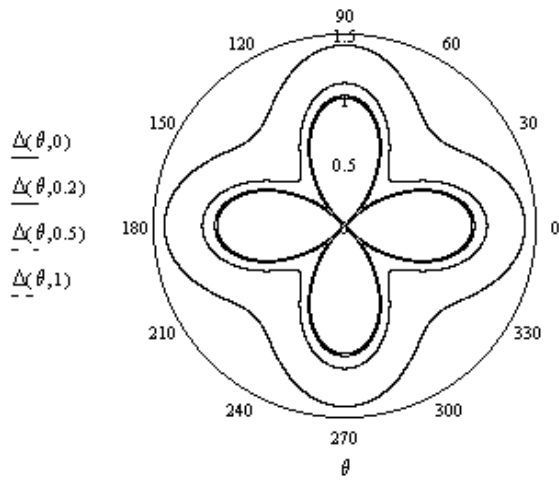


Fig 10: Amplitude Δ of the $d_{x^2-y^2}+i\epsilon s$ OP for $\epsilon=0,0.2,0.5,1$ as a function of angle θ .

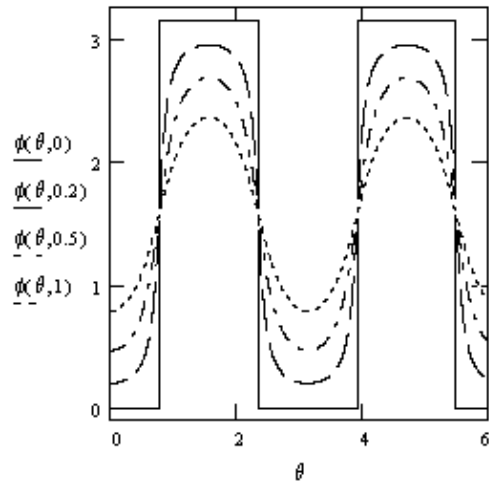


Fig 11: Phase ϕ of the $d_{x^2-y^2}+i\epsilon s$ OP for $\epsilon=0,0.2,0.5,1$ as a function of angle θ .

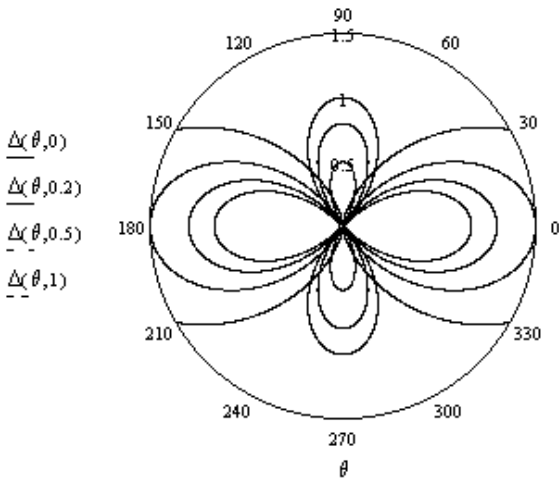


Fig 12: Amplitude Δ of the $d_{x^2-y^2}+\epsilon s$ OP for $\epsilon=0,0.2,0.5,1$ as a function of angle θ .

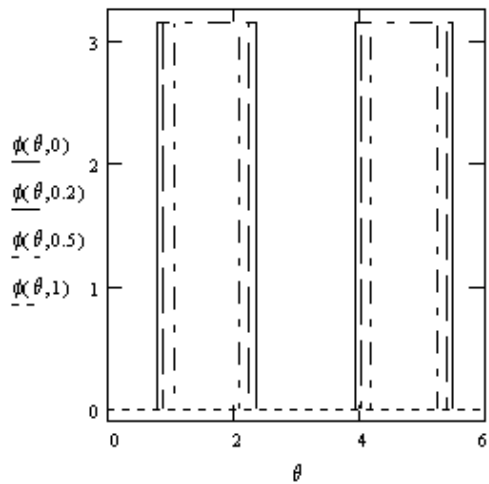


Fig 13: Phase ϕ of the $d_{x^2-y^2}+\epsilon s$ OP for $\epsilon=0,0.2,0.5,1$ as a function of angle θ .

2 The Differential Conductance Spectrum

2.1 Isotropic Order Parameter

The differential conductance spectrum is a powerful measurement to obtain information about the properties of a superconductor. In this chapter we review the case of an isotropic s-wave superconductor / metal contact.

If one applies a voltage V between two electrodes and measures the current I , then the differential conductance is defined as $g(V)=dI/dV$. Such a spectrum can only be taken in quasi-equilibrium if the interface between the two electrodes is a weak link, which means that the probability for an electron to go from one electrode to the other is small. Experimentally this can be achieved by creating an insulating layer or by limiting the contact area between the electrodes. In order to understand how such a measurement can give information about the properties of a SC, two extreme cases, the tunneling contact and the Sharvin contact, are discussed, before treating the intermediate cases in the framework of the theory of Blonder, Tinkham and Klapwijk (BTK) [16]. In all of the following calculations $T=0K$ is assumed.

2.1.1 Sharvin Contact

The term Sharvin contact is used if there is a small, direct contact between the metal and the superconducting material. A small contact area causes the resistance due to the finite number of quantum channels. If no voltage is applied between the two electrodes, then an electron coming from the normal metal can not enter as a quasiparticle (qp.) into the SC, unless it has minimum energy equal to the sc gap Δ , otherwise it has to undergo Andreev reflection. In the case of an Andreev reflection the electron is reflected as a hole in the normal metal and a pair is added to the sc. condensate. The incoming electron carries a current equal to $e v_F$, the reflected hole carries a current $(-e)(-v_F)$. Current conservation shows that the added pair carries a current $2e v_F$. If the applied voltage is larger than Δ , then the incoming electron can enter the SC as a qp excitation. In this case, the total current is equal to $e v_F$. Therefore in a Sharvin contact the conductance for the case $V<\Delta$ has to be twice the conductance for the case $V>\Delta$.

2.1.2 Tunneling Contact

The term tunneling contact is used, if an insulating layer separates two electrodes. In this case, an incoming electron with energy smaller than Δ , is reflected back into the normal metal and no current passes. The conductance for $V<\Delta$ is therefore zero. However if a voltage larger

than Δ is applied, then the electron can enter the SC as a qp excitation carrying a current equal to $e v_F$. Therefore in a tunneling contact the conductance has to be zero for the case $V < \Delta$ and finite for the case $V > \Delta$.

2.1.3 BTK Theory

Since experiments are not ideal, a whole spectrum of different results ranging between the two limiting cases presented above are expected. The origin of the variety can be due to different barrier thickness, barrier height or pinholes. For s-wave superconductors, Blonder, Tinkham and Klapwijk (BTK) [16] have given a detailed calculation of the differential conductance, including the temperature dependence, also for the intermediate cases. They introduced a dimensionless parameter describing the insulating barrier strength, Z . The Sharvin limit is then given by $Z=0$ and the tunneling limit by $Z \gg 1$. The BTK theory is described briefly in the following.

The calculation has been done by BTK for the normal conducting electrode since there all current is carried by single particles, and none has supercurrent, however since the current must be conserved, it can be calculated at any point. The current through the contact, which is proportional to the number of electrons passing per unit time, is then given by

$$I = 2 \cdot N(0) \cdot e \cdot v_F \cdot A \cdot \int_{-\infty}^{\infty} [f_{\rightarrow}(E) - f_{\leftarrow}(E)] dE ,$$

where A is an effective-neck cross-sectional area, including a numerical factor for angular averaging which will depend on the actual 3D geometry. $N(0)$ refers to the one-spin density of states at the Fermi energy ϵ_F . $f_{\rightarrow}(E)$ is the distribution function for electrons travelling towards the SC electrode and $f_{\leftarrow}(E)$ is the distribution function for electrons moving in the opposite direction. It is assumed that the distribution functions in each electrode, for incoming electrons, are given by the Fermi distribution. The applied voltage taken into account, one gets in the normal metal the distribution function $f_F(E - eV)$ and in the SC $f_F(E)$. It follows

$$f_{\rightarrow}(E) = f_F(E - eV)$$

$$f_{\leftarrow}(E) = A(E) \cdot [1 - f_F(-(E - eV))] + B(E) \cdot f_F(E - eV) + T(E) \cdot f_F(E)$$

The first term describes electrons coming from the normal metal, being Andreev reflected into holes, where $A(E)$ is the probability of Andreev reflection. The second term describes electrons coming from the normal metal being normally reflected, where $B(E)$ is the probability of normal reflection. The third term, $T(E)=C(E)+D(E)$, describes electrons which are transmitted into the SC as electron-like qp, and as hole-like qp, with the probability $C(E)$ and $D(E)$, respectively, as depicted in Fig 14.

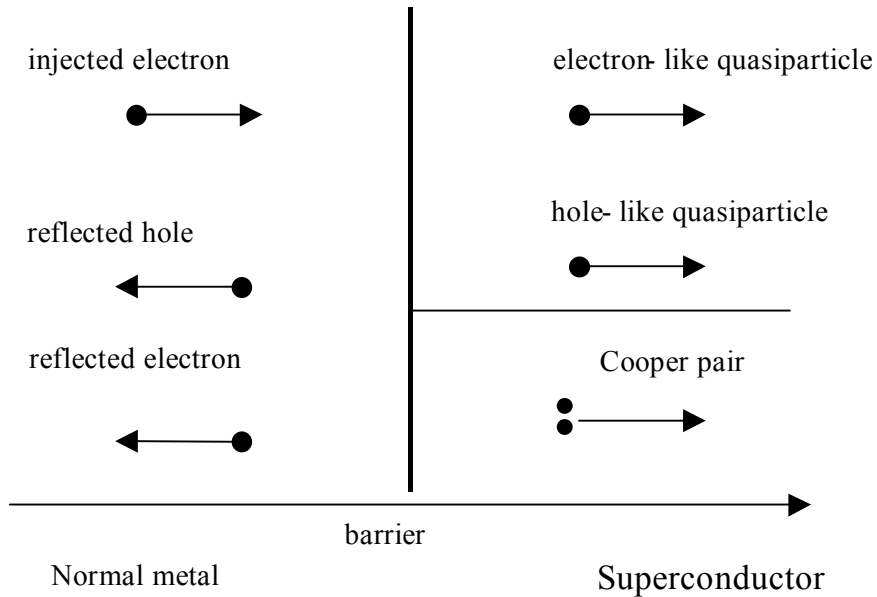


Fig 14: Schematic illustration of the reflection and transmission processes of qp at the interface in a one-dimensional model.

The final form is obtained by combining the equations using $A+B+T=1$, which implies that the sum of the probabilities for the different processes is equal to one.

$$I = 2 \cdot N(0) \cdot e \cdot v_F \cdot A \cdot \int_{-\infty}^{\infty} [f_F(E - eV) - f_0(E)] \cdot [1 + A(E) - B(E)] dE$$

In order to calculate $A(E)$ and $B(E)$ the quantum mechanical equation of the interface has to be solved. Here comes in the key innovative of BTK to use the Bogoliubov De-Gennes equations which are in the SC ($\Delta \neq 0$) the equivalent to the Schrodinger equation in the normal metal ($\Delta = 0$).

$$Eu(x) = h_0 u(x) + \Delta(x) \cdot v(x)$$

$$Ev(x) = -h_0 v(x) + \Delta(x) \cdot u(x)$$

$$\text{with } h_0 = -\hbar^2 \nabla_x^2 / 2m - \mu + U(x).$$

Δ , $U(x)$, and μ are the pair potential, Hartree-Fock potential and the chemical potential, respectively. The quantities $u(x)$ and $v(x)$ are wave functions of an electron-like qp and a hole-like qp respectively. $U(x)$ and $\Delta(x)$ are given as

$$U(x) = H\delta(x), \quad \Delta(x) = \begin{cases} 0 & x < 0 \\ \Delta_0 & x > 0 \end{cases}$$

The two component wave function is explicitly expressed as

$$\Psi(x) = \begin{pmatrix} u(x) \\ v(x) \end{pmatrix}.$$

The reflection coefficients $A(E)$ and $B(E)$ are determined by the boundary conditions,

$$\Psi(x)|_{x=0^-} = \Psi(x)|_{x=0^+},$$

$$\frac{d\Psi(x)}{dx}|_{x=0^-} = \frac{d\Psi(x)}{dx}|_{x=0^+} - \frac{2mH}{\hbar^2} \Psi(x)|_{x=0^+}$$

The conductance is then given by

$$g(E, Z, \Delta) \propto \frac{\partial}{\partial V} \int_{-\infty}^{\infty} f_F(E - eV) [1 + A(E, Z, \Delta) - B(E, Z, \Delta)],$$

as calculated in Fig 15. Z is the barrier strength defined by $Z = H / \hbar v_F$.

It has to be stressed that the whole calculation is based on the assumption that the superconductor has an isotropic s-wave order parameter, which is not momentum dependent. Therefore also the conductance $g(V)$ does not depend on the direction in which the electron

moves. This is certainly correct for many LTSCs, in which also the electron-phonon interaction is isotropic. However in the HTSC materials this is certainly not correct due to their large anisotropy.

Kashiwaya and Tanaka [17] have therefore extended the BTK theory to superconductors with anisotropic order parameters, which is presented in the following.

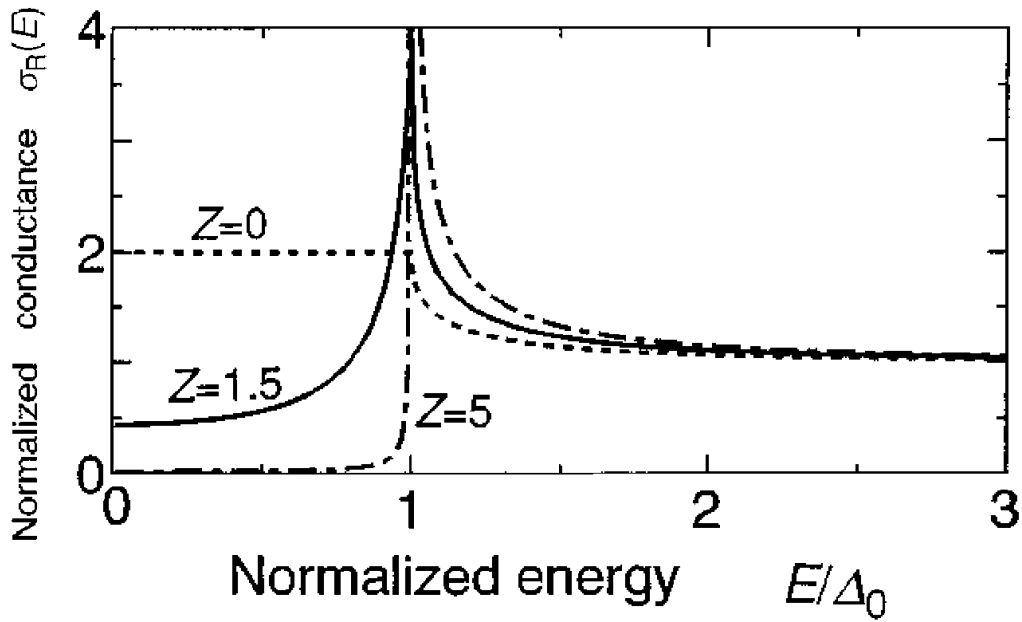


Fig 15: Differential conductance vs voltage for various barrier strengths Z at $T=0$ [17].

2.2 Anisotropic Order Parameter

In this chapter, we describe the tunneling theory of Tanaka and Kashiwaya [17] of normal metal / insulator / anisotropic SC (N/I/S) junctions. In particular, the normal metal / insulator / d-wave SC (N/I/d) junction is emphasized as a prototype of anisotropic SCs.

It is found that the tunneling conductance strongly depends on the angle between the normal to the interface and the crystalline axes of the anisotropic superconductor. Specifically, the existence of the ZBCP's as well as the gap-like conductance spectra can be naturally and systematically explained by assuming d-wave symmetry.

The important point of the theory of Tanaka and Kashiwaya is to include the angular dependence, which enters the calculation in two ways, as depicted in Fig 16. Firstly, the relative position of the d-wave order parameter with respect to the surface normal has to be defined. For example in the case of a $\langle 100 \rangle$ surface, the surface normal is the direction along which the magnitude of the pair potential becomes a maximum. This case is denoted as $\alpha=0$. In the case of a $\langle 110 \rangle$ surface, the surface normal is the direction along which the magnitude of the pair potential becomes zero. That case is labelled as $\alpha=\pi/4$. Secondly, the angle θ

between the electron trajectory and the normal to the surface has to be considered.

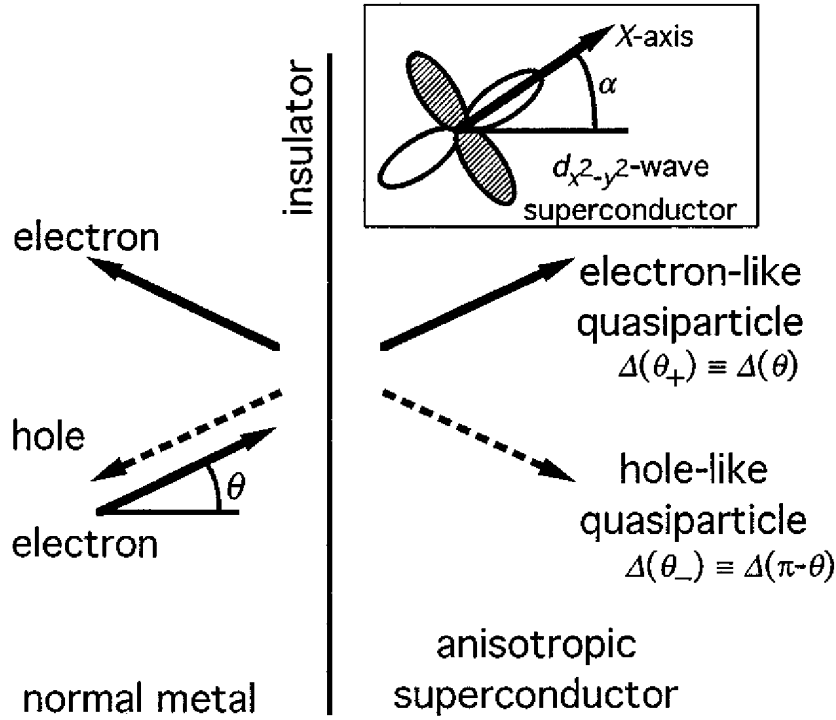


Fig 16: Schematic illustration of the reflection and transmission processes at the interface. In this figure the quantities θ and α express the injection angle of the electron and the angle between the normal vector of the interface and the x-axis of the $d_{x^2-y^2}$ -wave SC, respectively [18].

In all cases it has to be taken into account, that the momentum parallel to the interface and the group velocity are both conserved at the interface. As in the case of a s-wave SC the electron injected from the normal metal is reflected as an electron (normal reflection) and a hole (Andreev reflection). However the transmitted hole-like particle and electron-like particle experience different effective pair potentials $\Delta(\theta_+)$ and $\Delta(\theta_-)$, respectively, with $\theta_+=\theta$ and $\theta_-=\pi-\theta$. This is a feature peculiar to anisotropic superconductors and gives rise to an anomalous interference effect in the tunneling conductance.

Similar to the previous s-wave calculation, the reflection coefficients of the Andreev reflection $a(E,\theta,\Delta,Z)$ and normal reflection $b(E,\theta,\Delta,Z)$, which are now angular dependent, are calculated by the use of the Bogoliubov De-Gennes equations and the constraints of the boundary conditions.

$$a(E,\theta,\Delta,Z) = \frac{4 \cos^2 \theta \sqrt{E + \Omega_-} \sqrt{E - \Omega_+} \exp(-i\phi_+)}{(4 \cos^2 \theta + Z^2) \sqrt{E + \Omega_+} \sqrt{E + \Omega_-} - Z^2 \sqrt{E - \Omega_+} \sqrt{E - \Omega_-} \exp[i(\phi_- - \phi_+)]}$$

$$b(E, \theta, \Delta, Z) = \frac{-Z(Z + 2i \cos \theta) \left\{ \sqrt{E + \Omega_+} \sqrt{E + \Omega_-} - \sqrt{E - \Omega_+} \sqrt{E - \Omega_-} \exp[i(\phi_- - \phi_+)] \right\}}{(4 \cos^2 \theta + Z^2) \sqrt{E + \Omega_+} \sqrt{E + \Omega_-} - Z^2 \sqrt{E - \Omega_+} \sqrt{E - \Omega_-} \exp[i(\phi_- - \phi_+)]}$$

$$\text{with } \exp(i\phi_{\pm}) = \Delta(\theta_{\pm}) / |\Delta(\theta_{\pm})|, \quad \Omega_{\pm} = \sqrt{E^2 - |\Delta(\theta_{\pm})|^2}, \quad Z = 2mH / \hbar^2 k_F.$$

Using the coefficients a and b, the normalized tunneling conductance $\sigma(E)$ is calculated according to the formula given by BTK

$$\sigma(E) = \frac{\bar{\sigma}_S(E)}{\bar{\sigma}_N(E)}, \quad \bar{\sigma}_i(E) = \frac{1}{\pi} \int_{-\pi/2}^{\pi/2} \tilde{\sigma}_i(E, \theta) d\theta \quad (i = S, N),$$

$$\tilde{\sigma}_S(E, \theta) = 1 + |a(E, \theta)|^2 - |b(E, \theta)|^2, \quad \tilde{\sigma}_N(E, \theta) = \frac{4 \cos^2 \theta}{4 \cos^2 \theta + Z^2},$$

where $\bar{\sigma}_N(E)$ and $\tilde{\sigma}_S(E, \theta)$ are the tunneling conductance in the normal state and in the superconducting state, respectively.

The normalized bulk density of states of a anisotropic SC, is given by

$$\sigma_0(E) = \frac{1}{2\pi} \int_{-\pi/2}^{\pi/2} d\theta \left(\frac{E}{\sqrt{E^2 - |\Delta(\theta_+)|^2}} + \frac{E}{\sqrt{E^2 - |\Delta(\theta_-)|^2}} \right).$$

2.2.1 $d_x^2 - d_y^2$ -Wave, In-plane Tunneling

When the transmitted qp is in the crystal ab-plane, the effective pair potentials $\Delta(\theta_+)$ and $\Delta(\theta_-)$, for the d-wave case, can be expressed as

$$\Delta(\theta_+) = \Delta_0 \cos(2\theta - 2\alpha), \quad \Delta(\theta_-) = \Delta_0 \cos(2\theta + 2\alpha)$$

In Fig 17a-c, $\sigma(E)$ is calculated for various values of Z and α . For $Z=0$, $\sigma(E)$ does not depend on α , and decreases from 2 with increasing E . For nonzero α and Z , $\sigma(E)$ at $E=0$ is enhanced compared with the case of $Z=0$. For large Z and nonzero α , $\sigma(E)$ does not approach the NDOS $\sigma_0(E)$, contrary to the conventional tunneling spectra of s-wave superconductors.

2.2.2 d_x^2 - d_y^2 -Wave, c-Axis Tunneling

In general, $\sigma(E)$ can be obtained for any surface orientation, by extending the theory to a three-dimensional system [19]. In the specific case of c-axis tunneling, the interface is perpendicular to the z-axis (= c-axis) and is located at $z=0$. It is assumed, that the pair potential depends on the azimuthal angle φ in the xy-plane (= ab-plane) as $\Delta_0 \cos(2\varphi)$. In this case, the hole-like qp and the electron-like qp, transmitted into the SC, feel the same effective pair potentials for all directions and consequently ZBCP's are not expected. Qualitatively $\sigma(E)$ depends on Z as shown in Fig 17a, however this result may be not valid, if focusing has to be taken into account, as in the case of planar tunneling through a thick barrier. Then electrons are injected with $k_a \cong k_b \cong 0$, while due to the two-dimensional electronic structure, the final state is at $k_a^2 + k_b^2 = k_F^2$. Such tunneling requires energy equal to the Fermi energy and can therefore be only inelastic. This process can significantly change the conductance spectrum and is extensively discussed by Dagan et al [20].

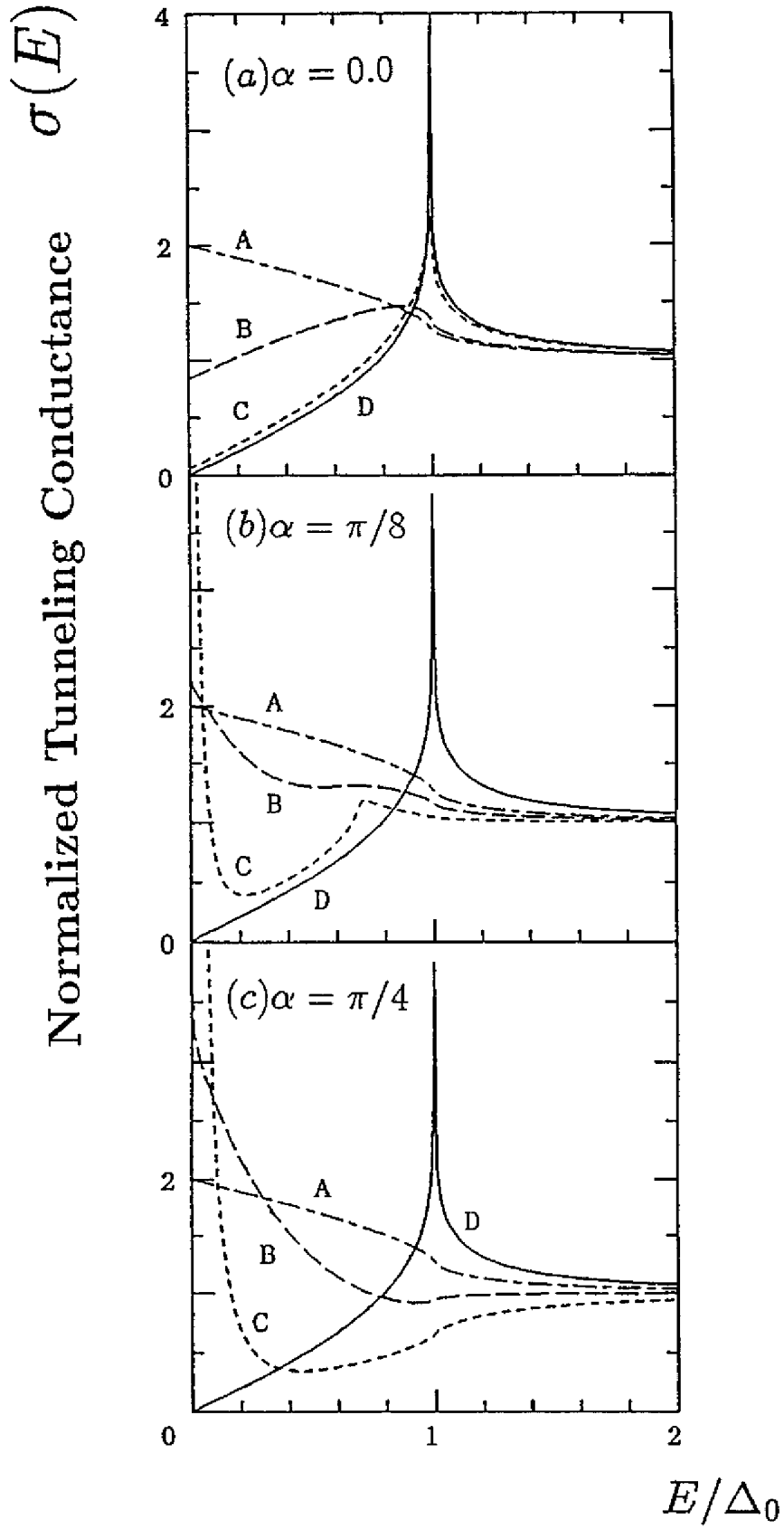


Fig 17a-c: Normalized tunneling conductance $\sigma(E)$ plotted as a function of E/Δ_0 for a normal metal / insulator / $d_x^2 - y^2$ -wave SC junction with the transmitted qp in the crystal ab -plane: (a) $\alpha=0$, (b) $\alpha=\pi/8$, and (c) $\alpha=\pi/4$. A: $Z=0$, B: $Z=1$, C: $Z=5$, D: $\sigma_0(E)$ [18].

2.2.3 $s+d_x^2-d_y^2$ -Wave and Extended s-Wave, In-plane Tunneling

Within the same formalism $\sigma(E)$ can also be obtained for $(s+d_x^2-d_y^2)$ -wave and extended s-wave SC where the pair potentials are expressed as $\Delta_S+\Delta_0\cos(2\theta)$ and $\Delta_S+\Delta_0\cos(4\theta)$, respectively. In the case of $(s+d_x^2-d_y^2)$ -wave SC, when $\Delta_0>\Delta_S$ is satisfied, a ZBCP is expected, since $\Delta(\theta_+)$ and $\Delta(\theta_-)$ change sign on the Fermi surface and $\exp[i(\phi_--\phi_+)]\rightarrow-1$ for some value of θ .

The ZBCP's are also expected for extended s-wave SCs under the same conditions. However, since there are eight nodes on the Fermi surface, the α dependence of $\sigma(E)$ is qualitatively different.

2.2.4 Complex Order Parameter, In-plane Tunneling

The conductance spectrum for a complex order parameter can be calculated by adding a complex component to the pair potential. From theoretical considerations, two possible complex order parameters may be stabilised at a pair-breaking surface of a $d_x^2-d_y^2$ superconductor [21], namely $d_x^2-d_y^2 + is$ or $d_x^2-d_y^2 + id_{XY}$.

For the $d_x^2-d_y^2 + is$ wave, the effective pair potentials $\Delta(\theta_+)$ and $\Delta(\theta_-)$ are

$$\Delta(\theta_+) = \Delta_d \cos(2\theta - 2\alpha) + i\Delta_s, \quad \Delta(\theta_-) = \Delta_d \cos(2\theta + 2\alpha) + i\Delta_s$$

and for the $d_x^2-d_y^2 + id_{XY}$ wave, the effective pair potentials $\Delta(\theta_+)$ and $\Delta(\theta_-)$ are

$$\Delta(\theta_+) = \Delta_{d1} \cos(2\theta - 2\alpha) + i\Delta_{d2} \sin(2\theta - 2\alpha),$$

$$\Delta(\theta_-) = \Delta_{d1} \cos(2\theta + 2\alpha) - i\Delta_{d2} \sin(2\theta + 2\alpha).$$

For both cases of in-plane tunneling the conductance spectrum is calculated as a function of surface orientation α and barrier strength Z , as shown in Fig 18.

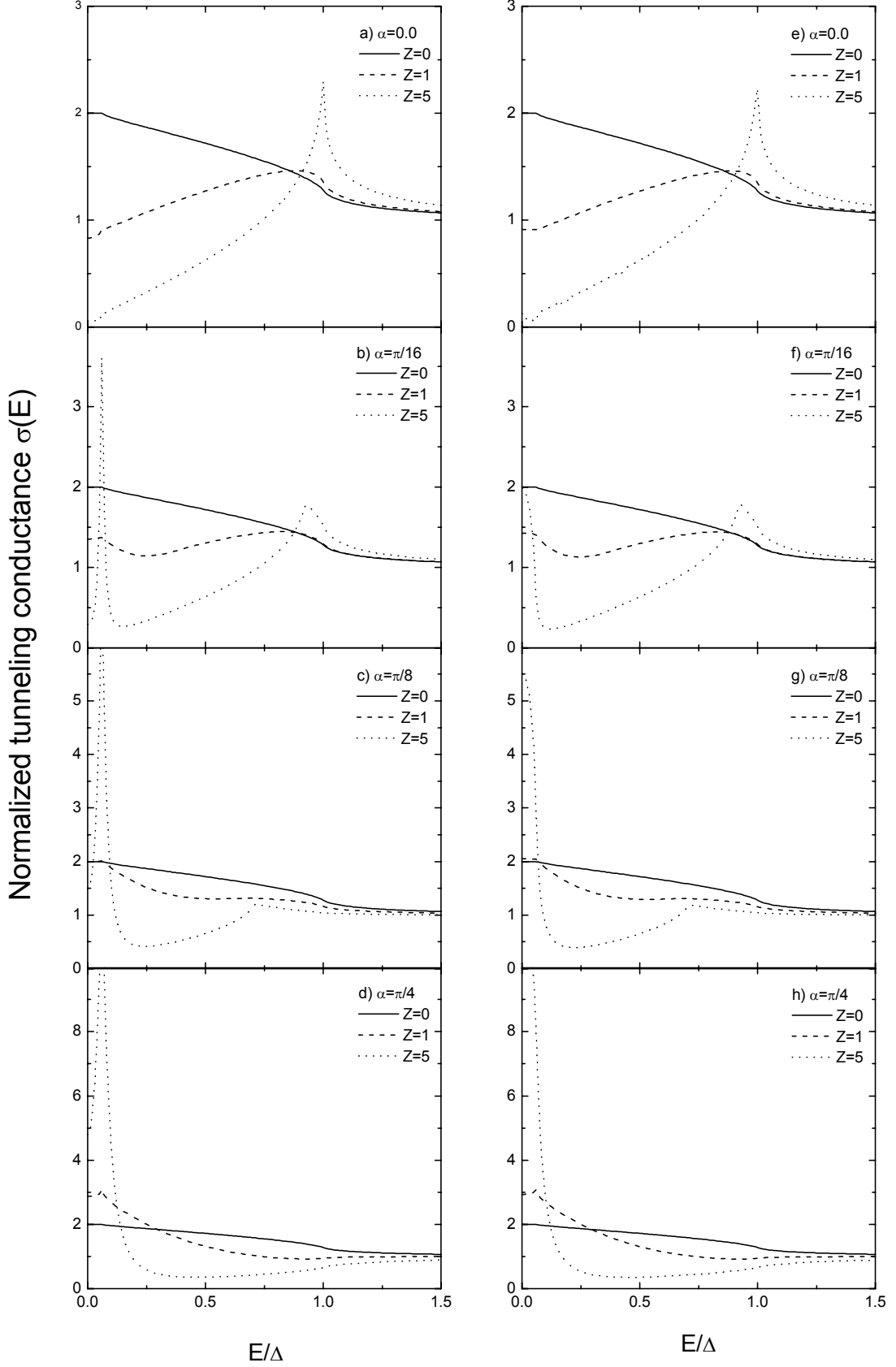


Fig 18: Normalised tunneling conductance $\sigma(E)$ plotted as a function of E/Δ_0 for a normal metal / insulator / superconductor junction with the transmitted qp in the crystal ab -plane for $\alpha = 0, \pi/16, \pi/8, \pi/4$ and $Z = 0, 1, 5$. The symmetry of the complex order parameter is $d_X^2 - Y^2 + i0.06s$ in a)-d) and $d_X^2 - Y^2 + i0.06d_{XY}$ in e)-f).

3 Fundamentals of YBCO Thin Film Deposition

3.1 The Structure of $Y_1Ba_2Cu_3O_{7-\delta}$

Compounds of the type $RE_1Ba_2Cu_3O_7$ (RE=rare earth) have at atmospheric pressure an orthorhombic structure (space group Pmmm), as illustrated in Fig 19. The unit cell of $RE_1Ba_2Cu_3O_7$ can be depicted as a stack of three perovskite cells, with copper atoms located at each corner of the cube. In the center of the cube is located in the middle perovskite a rare earth atom and in the upper and lower perovskite each a barium atom. The copper atoms have with respect to the oxygen environment two different positions. On the Cu(1) position the copper atom is surrounded by four oxygen neighbours, two oxygen atoms on each of the O(1) and O(4) positions. The second copper place Cu(2) is located somewhat above the base of a four sided pyramid, with oxygen atoms sitting in each of its corners. The oxygen at the tip is called O(4)- or apex-oxygen. The pyramids are connected by the corners and create the CuO planes.

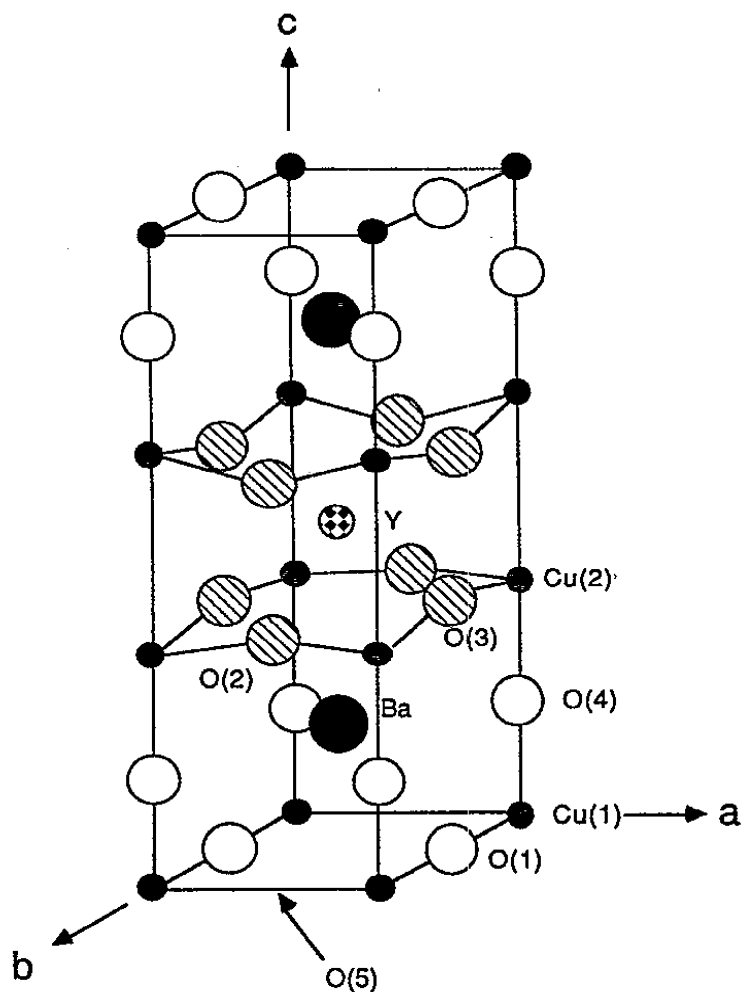


Fig 19: Structure model of $RE_1Ba_2Cu_3O_7$ [22]

The CuO chains are located along the b-axis. The oxygen in these chains is labelled as O(1)- or chain-oxygen. The oxygen on the O(5) position along the a-axis is missing. The lattice parameter of the b-axis is therefore larger than the lattice parameter of the a-axis.

For superconductivity in the $\text{RE}_1\text{Ba}_2\text{Cu}_3\text{O}_7$ systems the CuO planes as well as the CuO chains are viewed as important elements. In this work the system $\text{Y}_1\text{Ba}_2\text{Cu}_3\text{O}_{7-\delta}$ and $\text{Y}_{0.8}\text{Ca}_{0.2}\text{Ba}_2\text{Cu}_3\text{O}_{7-\delta}$ has been used.

In $\text{Y}_1\text{Ba}_2\text{Cu}_3\text{O}_{7-\delta}$ it has been well established that by changing the oxygen content δ the doping level changes from optimally to underdoped (Fig 20) [22]. The overdoped side can not be explored by oxygen doping, but with Ca doping, where Ca replaces partially Y within the solubility limit reached in $\text{Y}_{0.8}\text{Ca}_{0.2}\text{Ba}_2\text{Cu}_3\text{O}_{7-\delta}$ (Fig 21) [23].

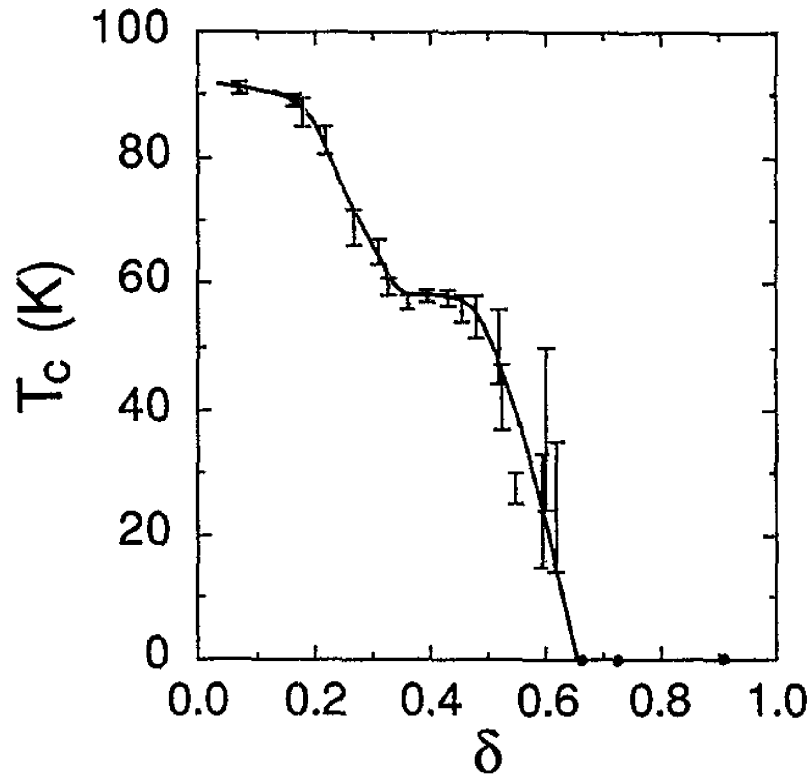


Fig 20: Superconducting transition temperatures, T_c , for oxygen-deficient samples $\text{Y}_1\text{Ba}_2\text{Cu}_3\text{O}_{7-\delta}$ [22]

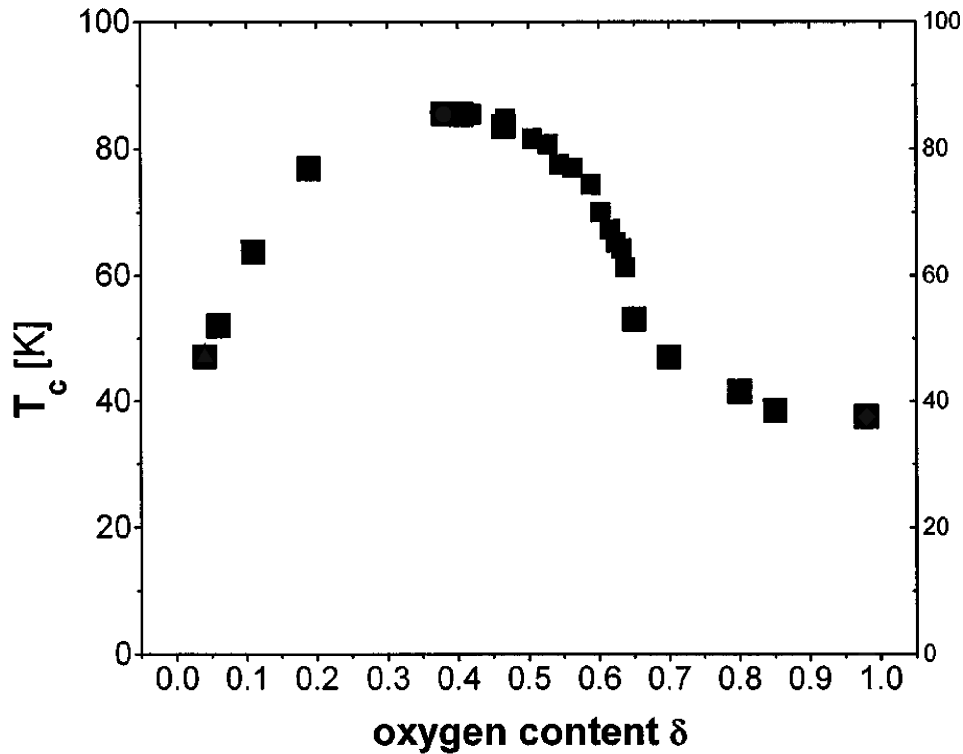


Fig 21: The critical temperature T_c vs. the oxygen deficiency, δ , in the CuO chains for $Y_{0.8}Ca_{0.2}Ba_2Cu_3O_{7-\delta}$ [24].

3.2 Epitaxial Growth

The term ,epitaxial‘ growth is used if a film grows on a single crystalline substrate with similar structure as the substrate [25]. Depending whether film and substrate are of the same or of different material one distinguishes between homoepitaxy or heteroepitaxy. If during growth the film has reached a thickness such that the substrate has no influence anymore on the film orientation, then heteroepitaxy goes over into homoepitaxy.

Therefore for the growth of YBCO mainly substrates with a perovskite structure are used. The lattice matching between film and substrate is an important parameter for epitaxial growth. A measure for the quality of the lattice matching is the quantity m_a with respect to an axis a :

$$m_a = \frac{a_S - a_F}{1/2 \cdot (a_S + a_F)}, \quad \text{with S: Substrate, F:Film}$$

Furthermore the thermal stability of the substrate is crucial. Chemical reactions between substrate and film, which disturb epitaxy or lead to the creation of secondary phases, have to be avoided.

Due to different lattice matching the choice of the substrate and its cut have a strong influence on which orientation the YBCO film is growing. On (100) oriented cubic substrates such as SrTiO_3 (STO) or LaAlO_3 (LAO) two growth modes compete which are favoured due to the small lattice mismatch: the thermodynamically favourable c-axis growth (c-axis \perp substrate surface) and the kinetically favourable a-axis growth (a-axis \perp substrate surface) (Fig 22).

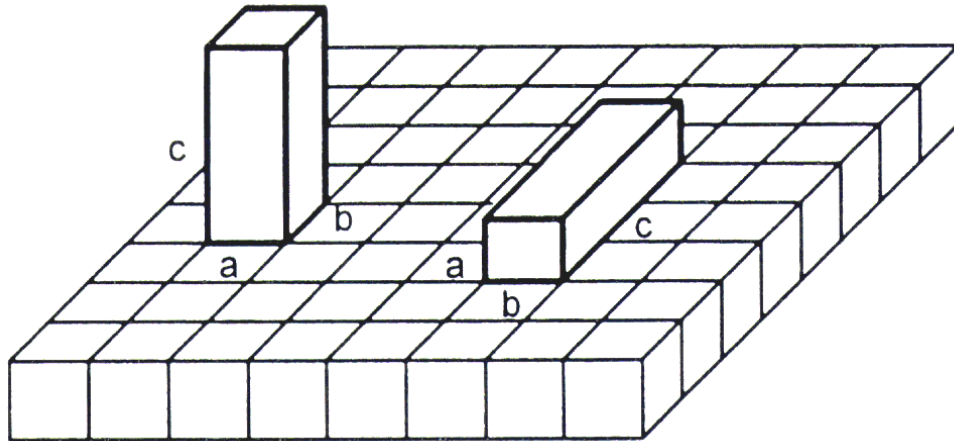


Fig 22: Schematic representation of c- and a-axis oriented growth. The label of the growth orientation depicts the axis, which stands perpendicular to the substrate surface [26].

The formation of a specific orientation of a YBCO film is not yet completely resolved. However it is very likely that epitaxy originates in nucleation sites and that therefore the significance of nucleation for the epitaxy growth lies in the nucleation speed which reaches for specific orientation of the nucleus very large values [27]. In principle it has been shown, that an enlargement of the migration length of the adsorbed atoms due to an increase of the substrate temperature, or to a reduction of oxygen partial pressure or of the deposition rate favors the c-axis growth [28]. In general, a-axis growth is therefore limited to a low substrate temperature, which is unfavourable due to a larger disorder and lower T_c in such films. However it has been shown that the transition temperature between a- and c-axis growth can be shifted to higher temperatures by a proper choice of substrates [29]. Finally, a-axis oriented films can be grown at similar temperatures as for the growth of c-axis oriented films by the use of a $\text{Pr}_1\text{Ba}_2\text{Cu}_3\text{O}_7$ template layer [30]. Very important for this work is the fact that by the use of a tetragonal substrate such as (100)-oriented LaSrGaO_4 (LSGO), in-plane orientation of the a-axis film can be achieved [30] (Fig 23). Such a film is with respect to its crystallographic structure similar to untwinned single crystal, in contrast to films grown on cubic (100)-oriented STO, where the films are twinned (Fig 23). The substrates used in this work have been purchased from Komatsu Ltd. (LSGO, out of production) and from Crystal

(LSGO,STO,LAO).

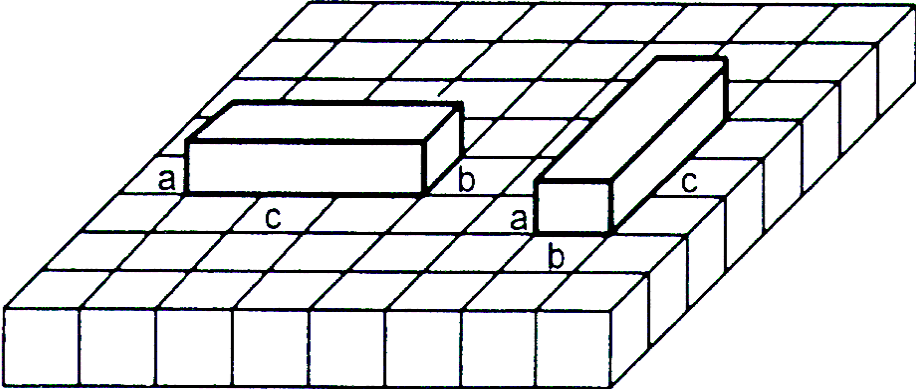


Fig 23: Schematic representation of the orientation of an a-axis oriented film on a cubic substrate surface: the two orientations of the c-axis in the plane are equally probable [26].

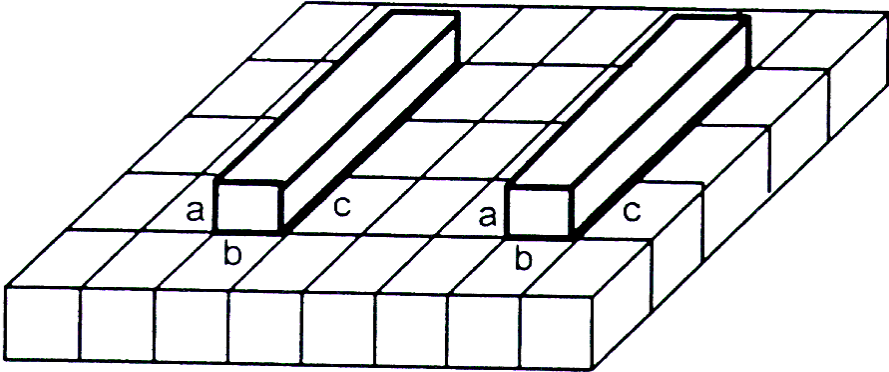


Fig 24: Schematic representation of the in-plane orientation of a-axis oriented films on a tetragonal substrate surface: the b-axis and the c-axis are aligned in the plane [26].

3.3 Sputtering

The preparation of superconducting films can be done by different deposition methods such as laser ablation [31], chemical vapor deposition [32], thermal or electron beam evaporation [33] and sputtering [34]. In this work, YBCO films have been grown by sputtering.

Sputtering, or more accurately, cathodic sputtering, means the erosion of a target by means of bombardment with positively charged ions. A possibility to generate positive ions is the self-generated gas discharge. A dc voltage is applied between a conducting target as a cathode and an anode. Above a certain voltage plasma is generated. The positive ions within the plasma are accelerated with the cathode dark space towards the target. At impact particles are ejected from the target. Additionally secondary electrons are generated due to direct momentum transfer or neutralization of ions (Auger-effect). These electrons are accelerated away from the target and create by impact ionization new positive ions. The threshold energy for sputtering is several 10eV. The particle flux ejected from a metal target contains up to 95% neutral particles, the rest are negative and positive ions [35]. However in the case of an oxide target 20-30% of the particles can be negatively charged. In the case of a YBCO target it is known that negatively charged oxygen atoms cause severe bombardment damage of the growing film. For that reason the substrate should not be opposite to the target surface. This is guaranteed by the use of either a combination of the on-axis geometry with an inverted cylindrical target [34], or the off-axis geometry with a planar target. However, if the sputter system operates at very high gas pressure, effectively slowing down energetic particles, the substrate can oppose the target surface. In general sputtering targets are mounted on a permanent magnet which confines the plasma and enhances the sputtering rate. In this work magnetron sputtering in off-axis geometry has been used.

3.4 The Sputter System

The sputter system is depicted schematically in Fig 25. The core of the system is composed of three sputter guns purchased from U.S. Gun, which are mounted with 2“ planar targets purchased from Superconductive Components Inc. The sputter guns can be tilted from outside, parallel to the base plate, and therefore enabling consecutive or simultaneous growth of different compounds. The guns are operated with rf- or dc-power supplies. A resistive heater, which is powered and controlled by a ‘Eurotherm’ temperature controller, is placed onto the base plate in off-axis geometry. A conventional thermocouple senses the temperature of the heater plate. The gas flow is controlled by mass flow meters and the inlet is located above the heater plate, enabling a fast cooling in gas flow if necessary. When necessary, water

vapor was introduced from a vacuum tight glass bowl through a needle valve. The system is pumped by a combination of a diaphragm pump, turbo pump and cryogenic pump and can be evacuated below $1\text{E-}6\text{mbar}$. To load and unload samples, the system has to be exposed to air.

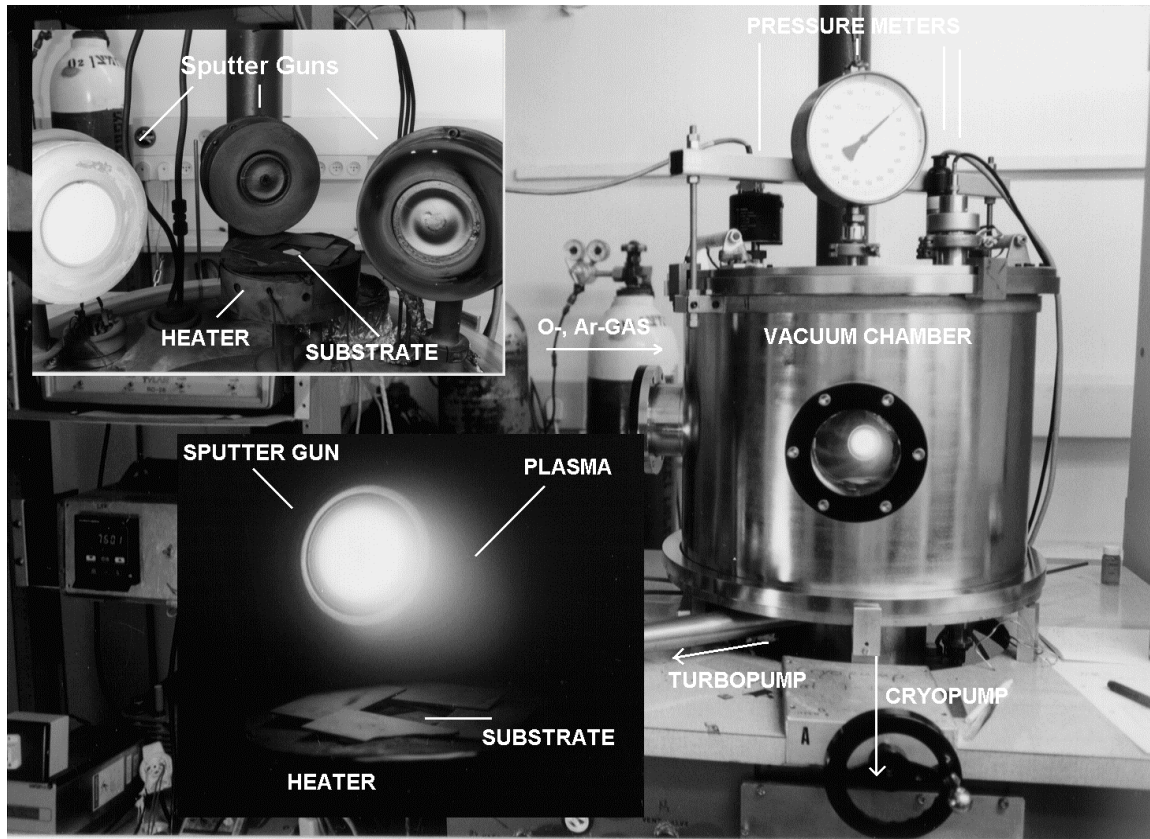


Fig 25: The sputter deposition system. Vacuum chamber height 50cm. Lower inset is a close look through the window onto an operating gun . Upper inset shows the inner configuration of the chamber prior deposition.

4 Characterisation Tools

4.1 Resistance vs. Temperature

Resistance measurements have been done with a four-point probe. Electrical wires were glued with silver paint to the film surface with contacts arranged in a square geometry. To ensure good thermal contact the samples were attached to a copper sample holder. The measurement current was limited to $10\mu\text{A}$ in order to prevent heating of the contacts. In a resistive measurement one superconducting path is enough to short the whole sample. Therefore even in a very inhomogeneous sample, a high T_C with a narrow transition width can be observed. The temperature is measured with a Platinum resistor between 60K and 300K, and below 60K with a carbon glass resistor. To ensure quasi equilibrium the temperature is changed at a rate of 0.1K/s.

The square geometry enables to measure anisotropies in the normal state resistance by alternating the current between the principal axis (Fig 26). In the limit of a film thickness, z , much smaller than the distance between electrodes, the two values of resistance, R_1 and R_2 , depend on the in-plane resistivities, ρ_1 and ρ_2 , as follows [36]:

$$R_1 = \frac{1}{2\pi} \frac{1}{z} \ln\left(1 + \frac{\rho_1}{\rho_2}\right) \sqrt{\rho_1 \rho_2}$$

$$R_2 = \frac{1}{2\pi} \frac{1}{z} \ln\left(1 + \frac{\rho_2}{\rho_1}\right) \sqrt{\rho_1 \rho_2}$$

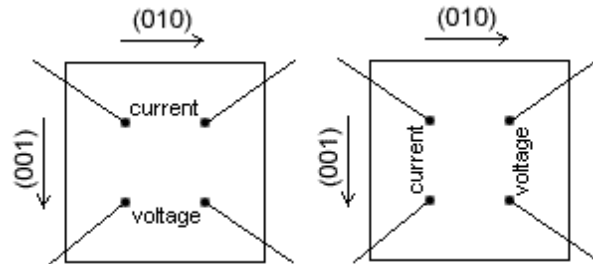


Fig 26: Resistance measurement in square geometry.

ρ_1 and ρ_2 have to be calculated numerically since the inverse function, g , of the resistance ratio is not analytic.

$$\frac{\rho_1}{\rho_2} = g(R_1, R_2), \quad \text{with} \quad \frac{R_1}{R_2} = \frac{\ln\left(1 + \frac{\rho_1}{\rho_2}\right)}{\ln\left(1 + \frac{\rho_2}{\rho_1}\right)}.$$

It follows that

$$\rho_1(R_1, R_2) = \frac{2\pi \cdot z \cdot R_2}{\ln(1 + g(R_1, R_2))\sqrt{g(R_1, R_2)}}$$
$$\rho_2(R_1, R_2) = \frac{2\pi \cdot z \cdot R_1}{\ln(1 + g(R_1, R_2)^{-1})\sqrt{g(R_1, R_2)^{-1}}}$$

The calculation has been done within a computer program [37].

4.2 Inductive Tc Measurement

In the inductive measurement the sample is clamped between an excitation coil and a sense coil. To amplify the induced voltage at the sense coil, a lock-in-amplifier is used. Above the superconducting transition the sample screens the field only weakly due to the finite resistance of the sample. As the resistance drops with temperature, the induced currents increase and enhance the screening. When the sample becomes superconducting the currents can flow unhindered. These surface currents produce a magnetic field, which compensates the applied field. The induced voltage drops then sharply. Since the sample does not enclose the main coil, a residual voltage remains which becomes the larger, the smaller the sample is.

The inductive measurement enables to probe a large fraction of the sample since the applied ac-magnetic field induces screening currents in the whole sample, which shield the field. Since large magnetic fields may be applied, the screening currents in the sample can be much larger than the measurement currents in the resistive measurement. The transition width of the inductive measurement is therefore influenced by a much larger superconducting volume, than in the case of a resistive measurement. An advantage of the inductive measurement is that it does not need contacts on the sample.

4.3 X-Ray Diffraction

X-ray diffraction (XRD) is a standard method used to investigate the microscopic structure of matter. In this work XRD has been performed with a two-circle diffractometer in Bragg-Brentano-Geometry.

4.3.1 Two Angle Diffractometer

The two angle diffractometer is suitable to investigate samples with a high degree of texture with respect to their growth direction, the degree of texture and the calculation of the lattice

parameter. From a x-ray tube a diverging ray (CoK_α and CoK_β radiation) hits a metal filter which transmits only CoK_α radiation. The sample sits in the center of the ray and creates the center of the detector circle. A ray, which falls under the angle θ onto the sample, is diffracted by 2θ . If the detector moves twice as fast as the sample, those planes are in reflection, which are perpendicular to the bisector between incoming and outgoing ray. In general theta contains two terms. 1) ω , the angle between incoming ray and the sample surface, and 2) ϕ , the offset angle. ϕ is determined by the misalignment of the sample in the sample holder and by the miscut of the substrate, which occurs if the substrate surface is not cut exactly with respect to the crystal orientation. Only for $\phi=0$ is the angle omega equal to the Bragg angle θ , and $\theta=\omega+\phi$ otherwise. The offset angle ϕ is determined by an ω scan over the substrate peak. It is thereby assumed that the film does not grow tilted which would result in a shift of the film peaks to different angles. The adjustment of the angle θ and ω is done by a two axis goniometer with an accuracy of 0.005° .

4.3.2 θ - 2θ Scan

In the θ - 2θ scan the detector moves with twice the speed of the sample holder. After the correction of the offset angle, it is ensured that the incoming ray hits the sample under the angle θ and is diffracted by 2θ . Therefore only those planes are detected which are parallel to the sample holder surface. The diffraction spectrum contains the reflections of similar, parallel planes of different order.

4.3.3 ω -Scan

At an ω scan the detector is moved to the 2θ angle of a known reflection. The sample is then moved by an angle ϕ on the ω circle. The difference between the measured intensity maximum and the theoretical one is equal to phi and therefore measures the tilt of the planes with respect to the sample holder surface. Furthermore such a rocking curve gives information about grains which are tilted with respect to the normal and which are in reflex position. This deviation is determined by the full width at half maximum (FWHM) of the rocking curve and is a measure for the quality of the growth (mosaic spread). However for the evaluation of the growth quality, the total shape of the rocking curve is also important, since even in the case of a small FWHM there can exist tails of the curve which originate from high angle grain boundaries. The used XRD setup however enables only the determination of the FWHM.

4.3.4 Evaluation of the Lattice Parameters

The evaluation of the lattice parameter follows from the diffraction peaks in the diffraction spectrum. The Bragg equation gives the relation between the plane distance d and the diffraction angle Θ .

$$2 \cdot d_{hkl} \cdot \sin \Theta = n \cdot \lambda$$

λ : the wavelength of the x-ray

n : order of the reflex

The plane distance d_{hkl} is calculated in an orthorhombic unit cell as

$$d_{hkl} = \frac{1}{\sqrt{\left(\frac{h}{a}\right)^2 + \left(\frac{k}{b}\right)^2 + \left(\frac{l}{c}\right)^2}}$$

h,k,l : Miller indices

a,b,c : lattice parameters

In all methods the highest accuracy is achieved at high reflexion angles.

4.4 Scanning Electron Microscope (SEM)

The scanning electron microscope (SEM) enables to take pictures of sample surfaces at a magnification up to 50000x. Only conducting samples are suitable. Insulators are getting charged negatively due to the electron bombardment and lead to featureless, bright shining pictures. The interpretation of SEM pictures is non-trivial. For example a dark spot means merely, that from the concerned region less secondary electrons were emitted, than from the neighboring regions. The reason may be a hole or a region of different composition with different secondary electron coefficient.

4.5 Energy Dispersive X-ray Analysis (EDAX)

The energy dispersive x-ray analysis (EDAX) [38] involves the generation of x-rays by high-energy electron probes. The analysis is usually performed in a scanning electron microscope. In general the technique is capable of detecting elemental species to about the 0.1 at.-% (about 1000ppm) range. Because the input probe is a well-focused electron beam,

spatially resolved compositional data can be gained. Depth resolution is possible if the energy of the incoming electron beam is varied, which changes the penetration depth of the input probe. When a sample is bombarded with an energetic electron beam, both radiative and non-radiative emission processes occur. The non-radiative mechanisms result in the generation of Auger electrons. Vacancies are created in the electronic shells of atoms as a result of the incoming electrons. Electrons from outer shells fill the inner-shell vacancies to keep the atom in a lower energy state. If the energy differences between the transition electron and the vacancy shells are large enough, characteristic radiation in the form of x-rays are emitted. The creation of these x-rays and their detection constitute the basis for EDAX.

4.6 Atomic Force Microscope (AFM)

The main advantage of an atomic force microscope (AFM) is the possibility to extract values of the surface roughness. The height resolution is several orders of magnitude better than that of a conventional alpha-step scanner. The core of the AFM is a very fine tip which is attached to a very thin arm with an extremely small spring constant. The tip scans the surface in x-y direction and the piezo crystal for the z direction regulates the distance in such a way, that the force on the tip remains constant. This enables to depict the geometrical surface profile of a sample. The interaction between the tip and the surface is at small distances dominated by the repulsive electron electron interaction and at large distances by attractive Van-der-Waals forces. An AFM can therefore be operated either in the so called contact mode or non-contact mode respectively. In this work scans have been made mainly in the contact mode in the range of order of μm . However atomic resolution can be achieved in general.

5 Sample Preparation

All samples in this work have been grown by dc- and rf-sputtering from planar YBCO targets. The task of growing YBCO thin films with high transition temperature, high crystallinity and smooth morphology is difficult, since many deposition parameters have to be optimized, such as substrate temperature, total pressure, oxygen partial pressure, gas flow, distance plasma–substrate, power dissipation at the target. In general it is much easier to grow good c-axis oriented films than a-axis oriented films, since they form at higher substrate temperature where disorder is reduced. The optimization of the system has therefore been started with c-axis oriented films before moving on to a-axis oriented films.

5.1 c-Axis Oriented YBCO Films

After optimization, films with $T_c=90\text{K}$ have been grown, however with limited reproducibility. In order to keep the T_c high, the target had to be exchanged long before its expected lifetime had been reached. To understand this rather expensive drawback, changes in YBCO film properties related to the age of the target have been investigated. A correlation between reduced T_c , the appearance of holes in films and the deviation from stoichiometric film composition has been found. This has been published in [39] and will be shown in the following section.

5.1.1 Ageing of YBCO Targets

The subject of this investigation are YBCO films, which have been grown on (100) oriented LaAlO_3 , YSZ and MgO substrates. The substrates, which were glued on a heater plate with silver paint, were positioned at a horizontal and vertical distance to the center of the target of 3-4cm and 3cm, respectively. The rf-power was adjusted to 175W and the films were grown at a temperature of 740C and a pressure of 500mTorr oxygen. The samples were annealed for 30min at 500°C in 1atm oxygen to guarantee optimal oxygen doping. The typical film thickness after two hours of growth was 120nm as determined with an AFM. The samples are fully c-axis oriented as can be seen from Fig 27.

In this work, we observed that the quality of YBCO films was changing over many film growths although sputter parameters such as temperature, pressure, distance and rf-power were kept constant. Films grown with a new target have T_c values with an inductive downset about 90K while films grown after prolonged use of a target have T_c values not higher than 85K. This effect was also reported by other groups and seems to be typical for planar magnetron sputtering [40,41]. Beyond that it was observed in this work, that also the

morphology of these films depends on the target age. Films grown with a new target have a surface with or without CuO-particles, depending on the pressure used. Films grown with a target, used for more than 100 hours, have holes, which in density and size are getting bigger with the time of use of a target. In order to establish the origin of hole formation we tried to correlate the morphology of YBCO-films with results from EDAX analysis and X-ray diffraction. In Fig 28a-d we show the surface of four films grown on LaAlO_3 with different hole concentration. The hole formation as in Fig 28d is typical for films grown with an old target and occurs on all substrates that have been used, with differences only in the shape of the boundaries between holes and film. From these films the percentage of surface containing holes was determined by an image analysis. The obtained parameter is defined as hole fraction. One observes that with increasing hole fraction the hole size increases from submicron to micron and the boundary of a hole becomes irregular.

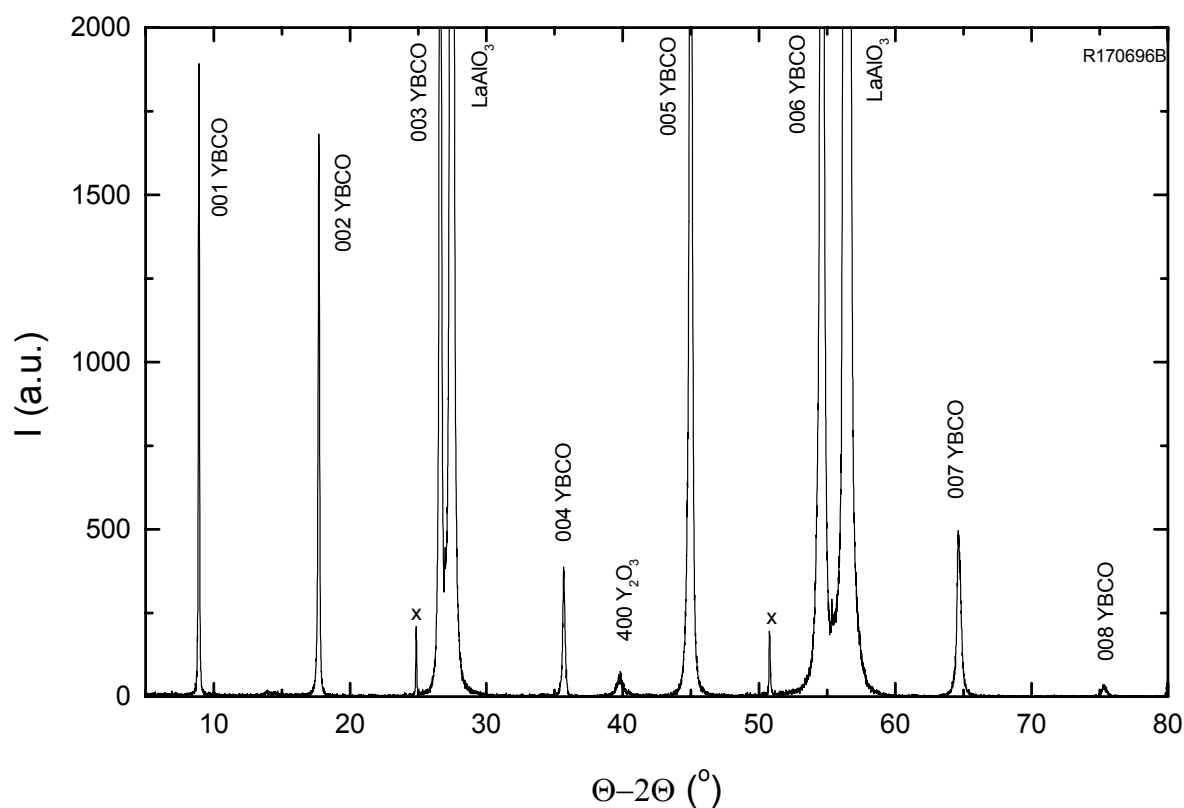


Fig 27: XRD pattern of a c-axis oriented film grown (100)- LaAlO_3 .

Changes of the film composition versus the hole fraction are shown in Fig 29. The EDAX measurement area was adjusted to $100\mu\text{m}^2$ size giving therefore an average value of the whole surface. The ratios of the peak integrals of Yttrium, Barium and Copper were calculated and normalized to the values of a film with low hole fraction. In this way qualitative changes of the composition with the hole fraction are determined.

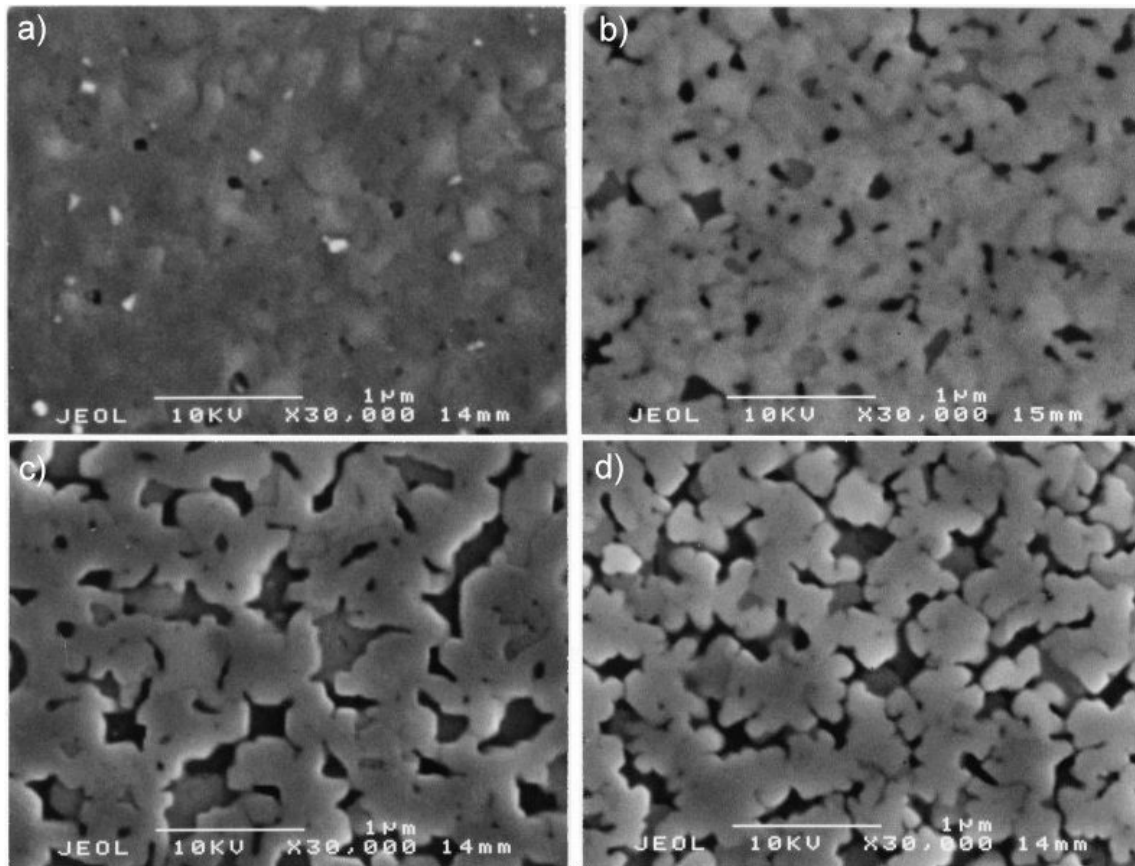


Fig 28: SEM images of four YBCO films with increasing hole fraction from (a) to (d). The white bar equals $1\mu\text{m}$.

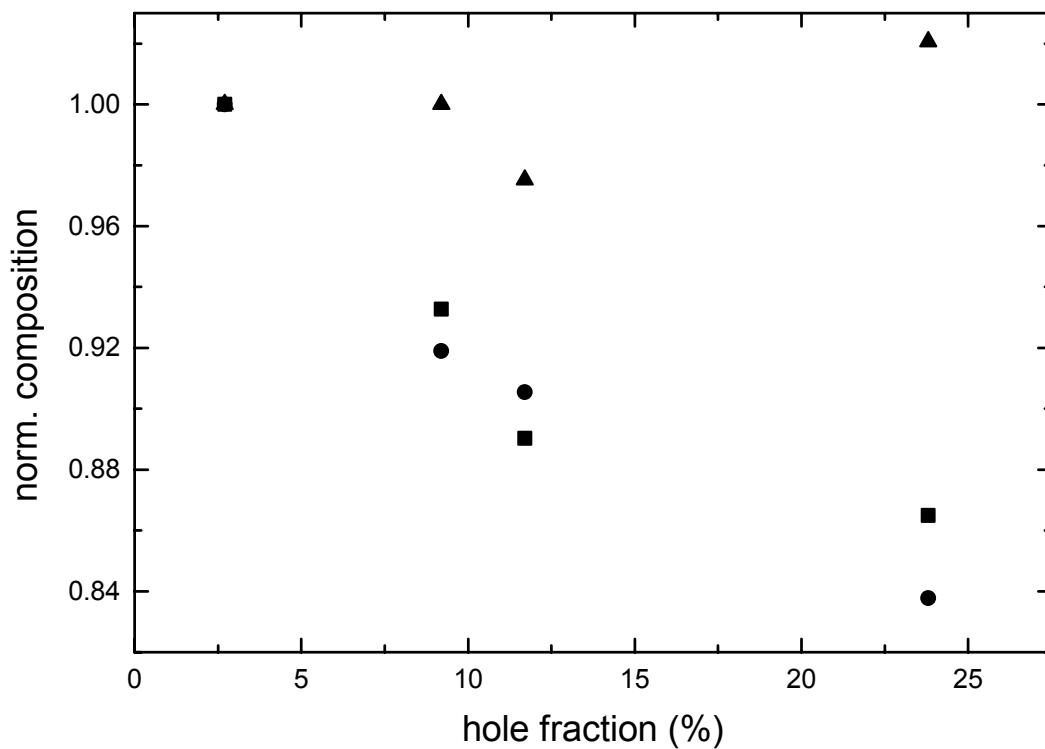


Fig 29: Ratio of EDAX peak intensities vs. hole fraction. Plotted are the intensity ratios of Cu/Ba (▲), Cu/Y (■) and Ba/Y (●) normalized to a film with 3% hole fraction.

It appears that with increasing hole fraction the ratio of Cu/Y and Ba/Y decreases, while the ratio Ba/Cu shows no significant change. This indicates that films with a higher hole fraction contain mainly an excess of Yttrium. Limiting the EDAX measurement area to $1\mu\text{m}^2$, it appears that the Yttrium excess is concentrated in the holes. The ratios of Cu/Y, Ba/Y and Ba/Cu inside a hole, normalised to areas besides a hole, were 48%, 41% and 85% respectively. Furthermore the peak intensity of substrate elements was stronger if measured in a hole. This shows that the film thickness in those film regions is indeed smaller. The XRD pattern of all films match the pattern of c-axis oriented YBCO films. Films with big hole fraction have additional peaks at $d=3.36, 2.64, 2.50, 2.08, 1.61, 1.53, 1.44, 1.34$ and 1.32\AA . These peaks match the pattern of polycrystalline Y_2O_3 with the 400-reflex ($d=2.64\text{\AA}$) being the strongest. As shown in Fig 30, the peak intensity of the 400-reflex increases with the hole fraction.

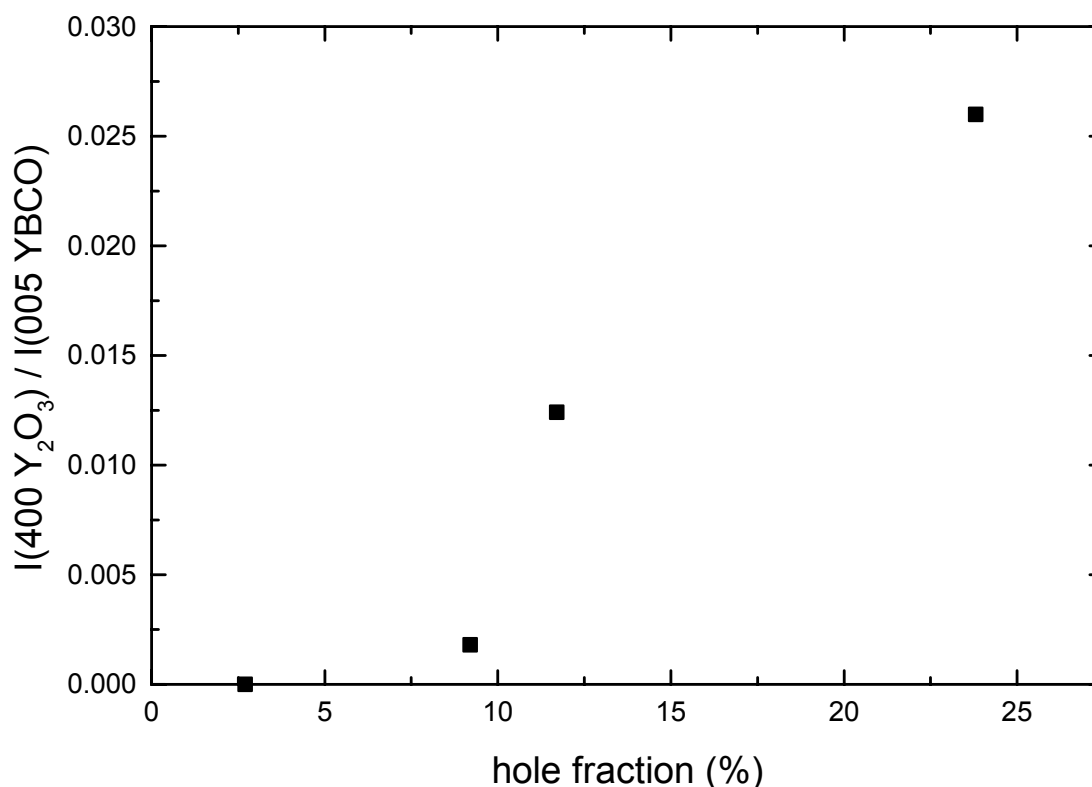


Fig 30: Ratio of XRD peak intensities of (400) Y_2O_3 and (005) YBCO vs. hole fraction.

Excluding the possibility of a further undiscovered secondary phase it is highly probable that the detected excess of Yttrium which appeared mainly in holes is located in the secondary phase Y_2O_3 . Therefore it can be assumed that the existence of Y_2O_3 itself is at the origin of hole formation. The irregular shape of the holes implies, that the secondary phase Y_2O_3 does not minimize its surface unlike as e.g. the secondary phases CuO whose particles are found to

have a typical size of 100-200nm in width and height. The tendency of wetting allows the Y_2O_3 to cover areas with a comparably small amount of material. What creates a hole, is that YBCO obviously prefers not to grow on Y_2O_3 . The effect of excess Yttrium on the film morphology is therefore bigger than the excess of Copper. It should be mentioned, that the EDAX spatial resolution did not allow to observe if Y_2O_3 is accumulated in nanoparticles as reported by Verbist et al.[42].

The dependence of T_c on the hole fraction is demonstrated in Fig 31. All films have a resistive transition onset above 90K. Films with holes which are as deep as the film thickness have a reduced inductive transition downset of 84-85K, while films with shallow holes and films without holes have transition widths of less than 1K.

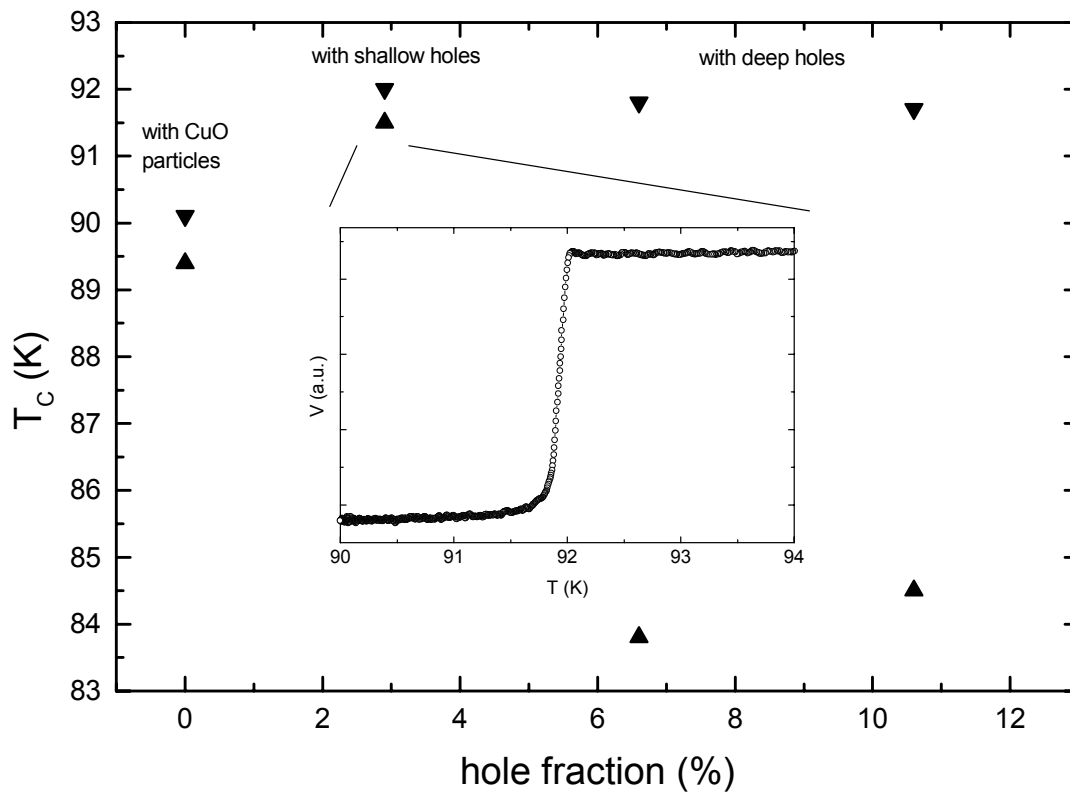


Fig 31: T_c vs. hole fraction. Plotted are the values of the resistive onset (\blacktriangledown) and the inductive downset (\blacktriangle). The inset shows the inductive transition of the film with the highest T_c .

The reduced inductive transition downset in films with deep holes may be explained by a cationic disorder in parts of the YBCO-phase [43] due to an incomplete phase separation between the 123-phase and Y_2O_3 . The degree of disorder in the YBCO-phase should decrease with distance from a hole explaining the high resistive onset of those samples caused by high T_c paths remote from holes. The high inductive transition downset in films with shallow holes can be understood, if a high T_c layer below the top layer containing holes shields regions of low T_c . It should be pointed out, that films with shallow holes indicate a significant change in

growth conditions within one growth.

In summary, a correlation between the appearance of holes, the secondary phase Y_2O_3 and an Yttrium rich film composition was found. The results indicate that Y_2O_3 is at the origin of hole formation. Its tendency of wetting together with the suppressed growth of YBCO on Y_2O_3 creates big holes. Films with deep holes have a reduced transition downset, which might be explained in terms of a cationic disorder in the YBCO-phase induced by an incomplete phase separation.

From these results it is clear, that long term stability of the composition of the growing layer has to be achieved in order to deposit in a reproducible way high quality YBCO-films.

The target was finally subjected to further investigation in order to conclude on the origin of the yttrium rich material flux. The results have been published in ref. 44,,45 and are summarised in of the next chapter.

5.1.2 The Influence of H_2O on the Target Lifetime

Further investigations have excluded that changes of the film properties are triggered by enhanced bombardment from the grooves, or by changes in the cationic composition of the target. Instead a lack of 10% oxygen in the target surface was detected by EDAX. It implies that sputtering of an old target enriches the plasma with less atomic oxygen than sputtering of a new one. This lack of atomic oxygen is probably the origin of a modified film composition, since Lecøer et al. [46] showed, that the oxidation of Ba and Cu is strongly reduced if the amount of atomic oxygen in the plasma falls below a certain value. This again should lead to a reduced sticking coefficient of Ba and Cu and therefore to an excess of Yttrium.

It had to be proved that atomic oxygen triggers the film composition by increasing the atomic oxygen pressure. According to Kaufmann et al. [47] the dissociation of O_2 in microwave discharges is almost entirely due to nitrogenous or hydrogenous impurities. This was confirmed by Costa et al. [48] to be valid also in a dc glow discharge although in that work it was shown that the enhanced atomic oxygen content in the plasma was caused by a reduced recombination rate of atomic oxygen at the chamber walls. In any case, each hydrogen atom introduced produces about 300 extra oxygen atoms. Therefore, if the assumption is correct, the film composition should not have an excess of Yttrium if an old target is sputtered in the presence of hydrogenous impurities. For that purpose a few milli Torr H_2O to the Ar/ O_2 mixture have been added, similar to Gavaler et al. [49]. As a result YBCO films without holes (Fig 32b) were obtained and no excess Yttrium was detected. Furthermore, typically concomitant features when sputtering with an old target, like sensitivity to previous growth conditions and decreasing dc-bias, are absent when adding

water vapour. The T_C of such films depends on the molecular oxygen pressure, which is discussed later.

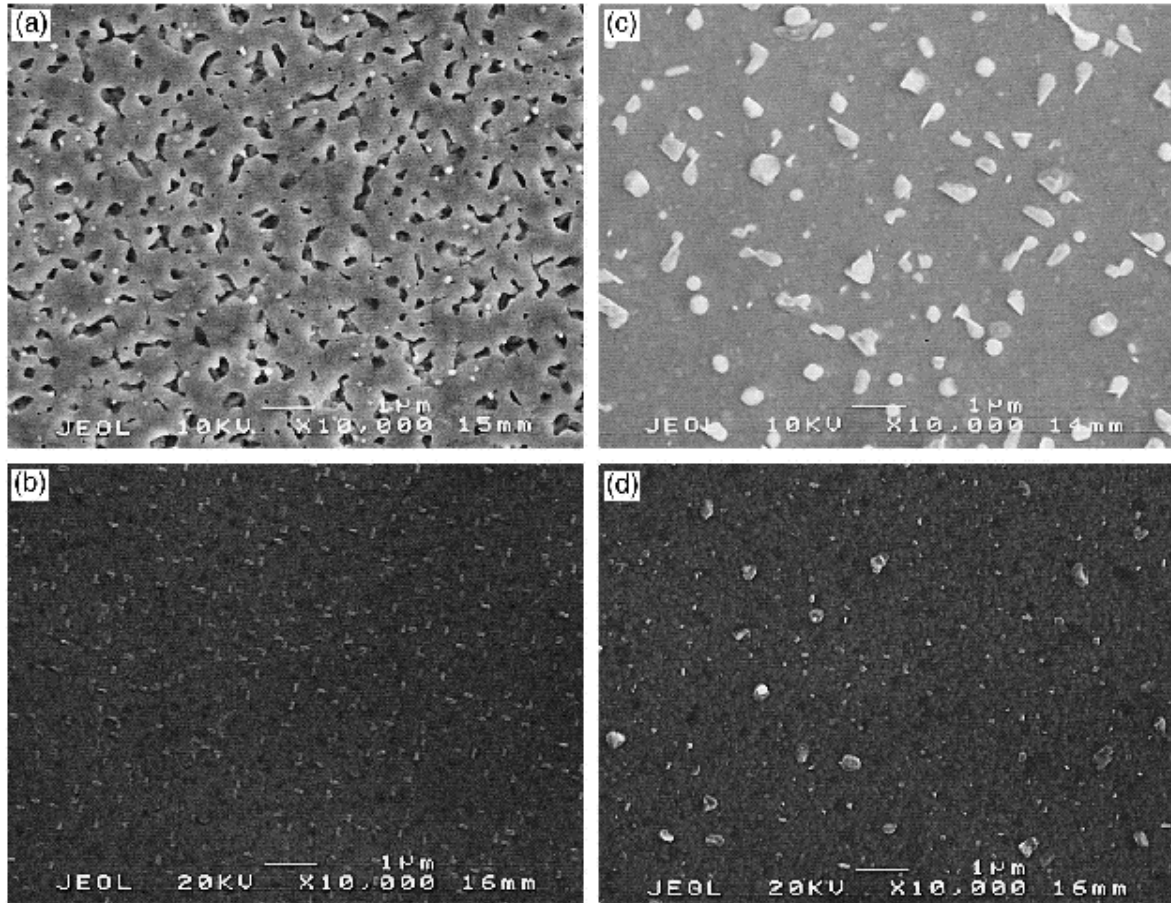


Fig 32: Scanning electron microscope pictures showing the surface morphology of YBCO films grown under different conditions: (a) film with holes and $T_C=84K$ grown with a prolonged used target, (b) film without holes and $T_C=85K$ after optimisation of rf-power and H_2O -pressure, (c) film with CuO -particles and $T_C=90K$ grown at high oxygen pressure, (d) film without CuO -particles or holes and $T_C=90K$ grown with the PST process.

First, we focus on the dc-bias as a function of water vapor pressure and rf-power. The dc-bias, V_{dc} , is a voltage that builds itself up in a rf-sputtering system [50]. Its value is very sensitive to the sputter parameters including the target surface, and therefore it is useful to control identical conditions of growth. Any deviation from its original values signals a drift of at least one parameter. In the case of a magnetron cathode, the dc voltage can be represented as a first approximation by $V_{dc} = P_{rf} / (P_0 + P_{rf})$, reaching a constant value for $P_{rf} > P_0$, P_0 is a constant [46]. This value has to be constant also in time. The dc-bias vs. sweeping rf-power and H_2O pressure is plotted in Fig 33. After a transient phenomenon between 0 and 30W, during which the plasma is not stable, the dc-bias drops monotonously with power. This anomalous behavior is very pronounced for sputtering without H_2O . With increasing H_2O pressure the curve is getting more flat, approaching the expected behavior.

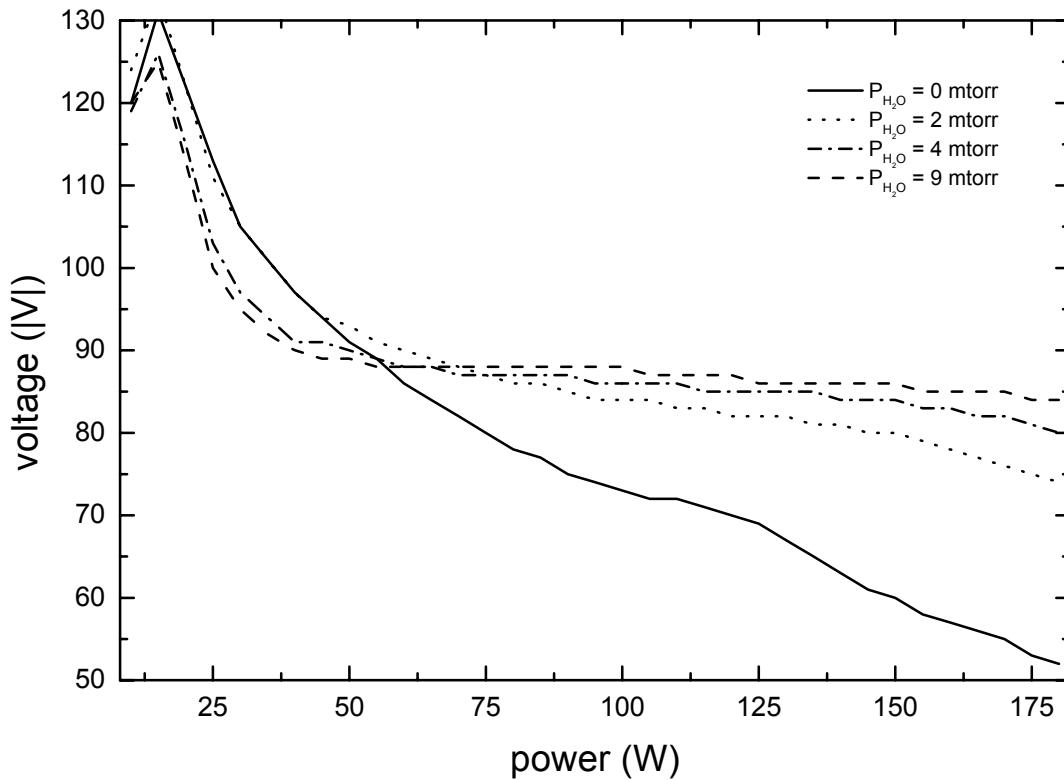


Fig 33: Bias voltage vs. rf-power measured for different H_2O pressure at $P_{O_2} = 20$ mtorr and $P_{Ar} = 190$ mtorr.

The dc-bias drops also with time. More exactly the voltage decreases logarithmically with a timescale of several hours. This voltage drop becomes smaller if H_2O is added (Fig 34). It is found that $V_e \sim \ln(P_{H_2O})$, where V_e is the near equilibrium voltage measured after long sputtering (Fig 35).

In this investigation any drift in the usual sputter parameters was excluded, and therefore the dc-bias anomaly has to be related to a nonequilibrium process which changes the target surface properties. It is known that loss of oxygen drives YBCO from the metallic state into the insulating state [51]. Further, the secondary electron emission coefficient of an insulator in general bigger than that of a metal [52], which gives a smaller dc-bias for insulating targets than for metallic ones. An oxygen depletion of the target surface can therefore explain a lower dc-bias. From the observation the following has to be concluded:

The target surface is in equilibrium only at sufficiently high atomic oxygen pressure. This conclusion is supported by the logarithmic dependence of the dc-bias on the H_2O pressure, pointing out to the catalytic effect of H_2O for obtaining a high atomic oxygen pressure. With increasing rf-power, the target surface temperature increases, and a higher atomic oxygen pressure is needed to preserve the oxygen content of the target surface. If the atomic oxygen pressure is too low, the target loses oxygen in excess and the dc-bias finally drops. It is the small ratio between atomic oxygen and cations that reduces the probability that sputtered

cations are oxidized. Different sticking coefficients of metals and oxides give finally a nonstoichiometric composition of the film, if grown at elevated temperatures.

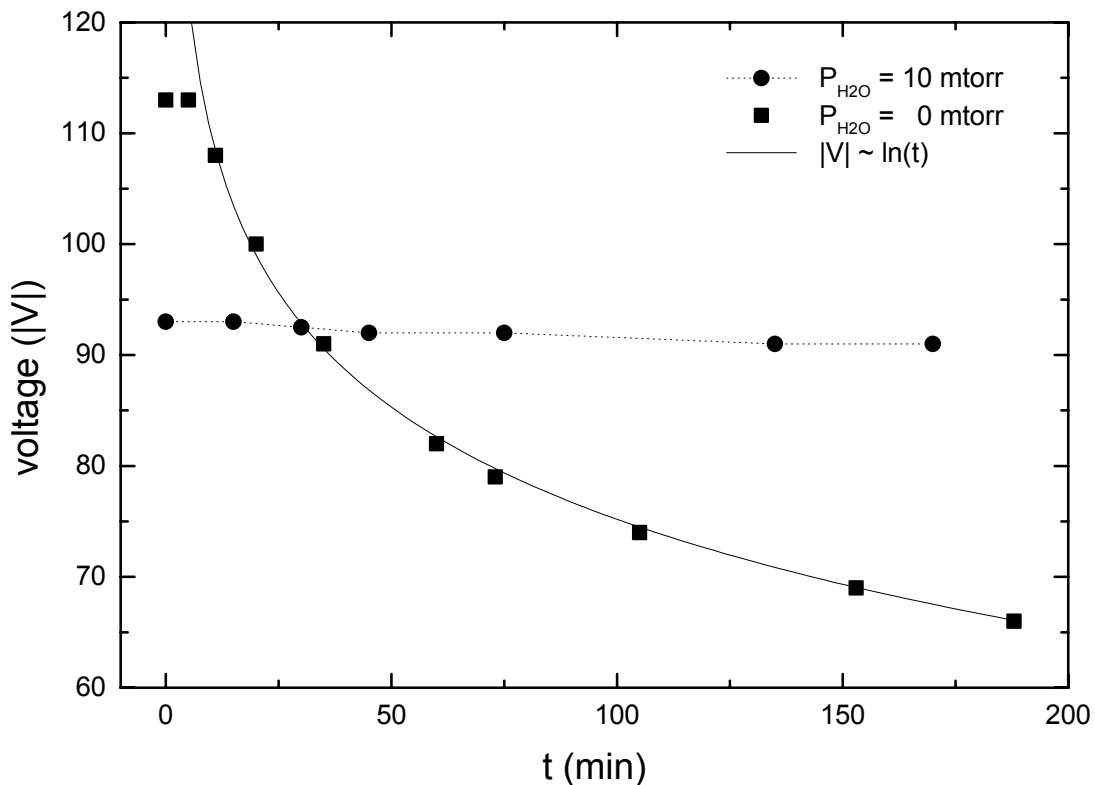


Fig 34: Bias voltage vs. Time t , with and without H_2O additive. Rf-power was set to 175W. The data obtained with $P_{H_2O} = 0$ mtorr is fitted to a logarithm (—).

Therefore for all growths of YBCO, we have chosen a rf-power equal to 100W and an H_2O -pressure to 2-4 mTorr. Under these conditions holes are absent in the film surface and the target does not have to be replaced prematurely. The growth conditions are also very reproducible, resulting in only a small variation of dc-bias of 3% within a growth, and from growth to growth. One has to believe that this is due to the H_2O -pressure being higher than the intrinsic one caused by desorption from the chamber wall and from the target itself. Since no load lock was used, the chamber was exposed to the atmosphere in-between each run.

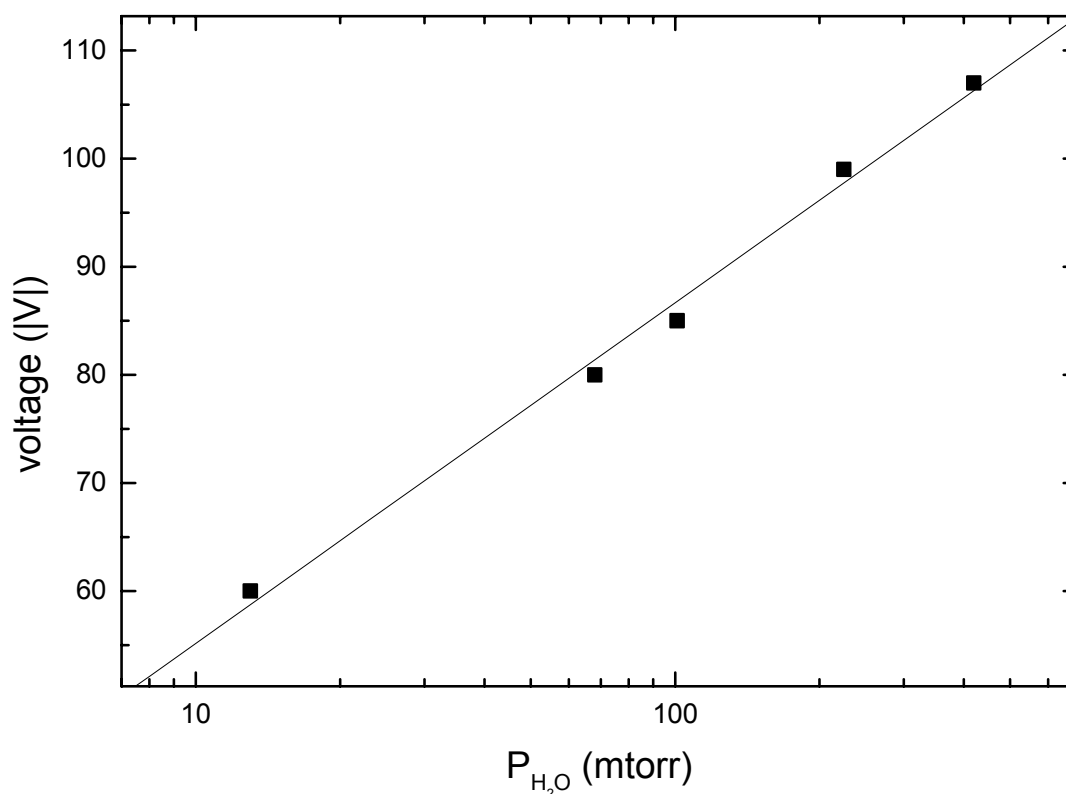


Fig 35: Bias voltage vs. the H_2O pressure, P_{H_2O} , on a semi-logarithmic scale. The data is fitted to a line (—).

5.1.3 Influence of the Molecular Oxygen Pressure on T_c

As has been shown, a proper adjustment of rf-power and H_2O -pressure guarantees the absence of holes in YBCO films and a long lifetime of YBCO targets. However, a remaining problem was still the presence of particles in YBCO films with $T_c=90K$. Typically such a film, as shown in Fig 32c, contains two kinds of particles. A combination of EDAX and XRD analysis resolved the particles of size $\geq 0.5\mu m$ as CuO and the smaller particles as $BaCuO_2$.

A variation of several sputter parameters revealed that the amount of the secondary phase CuO mostly depends on the molecular oxygen pressure, P_{O_2} , applied during growth. Therefore, several samples grown at different molecular oxygen pressure and at constant substrate temperature, as shown in Fig 36, were investigated. The fraction of substrate area covered with particles will be defined as particle fraction for easy quantification. It is found that the particle fraction is small in films grown at low oxygen pressure, close to the stability line of YBCO. With increasing P_{O_2} towards the stability line of CuO , the particle fraction increases (Fig 37). The residual particle fraction obtained at low oxygen pressure is caused by $BaCuO_2$ particles and is independent on specific growth conditions. Those particles are present also in films with holes as seen in Fig 32a. In addition it is observed that T_c increases with P_{O_2} from 83K to 90K (Fig 38), and the c-axis lattice constant decreases from 1.1712nm to 1.1682nm.

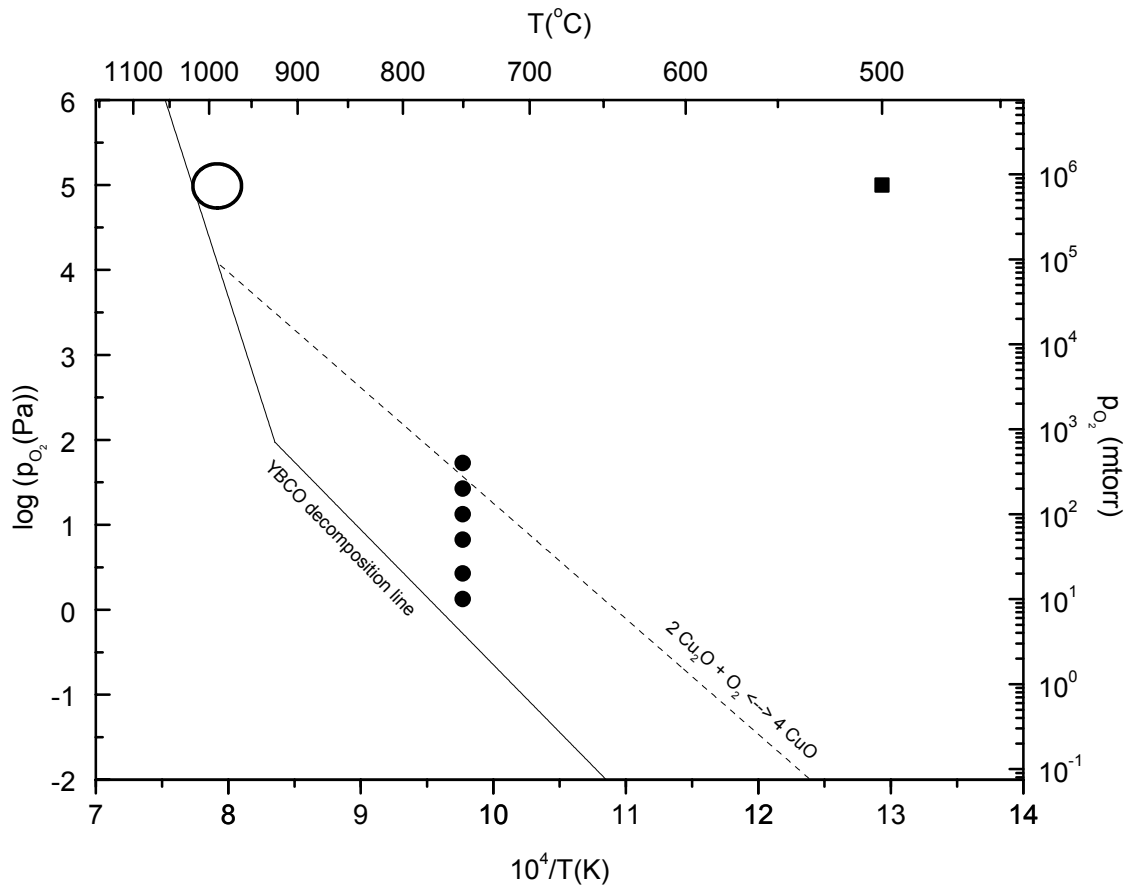


Fig 36: Growth conditions for YBCO single crystals (O) and films (●) plotted in a $\log PO_2$ vs. $1/T$ diagram, included is the annealing condition (■) and the thermodynamic stability line of the YBCO-123-phase (—) and CuO (---) from Lindemer et al. [53].

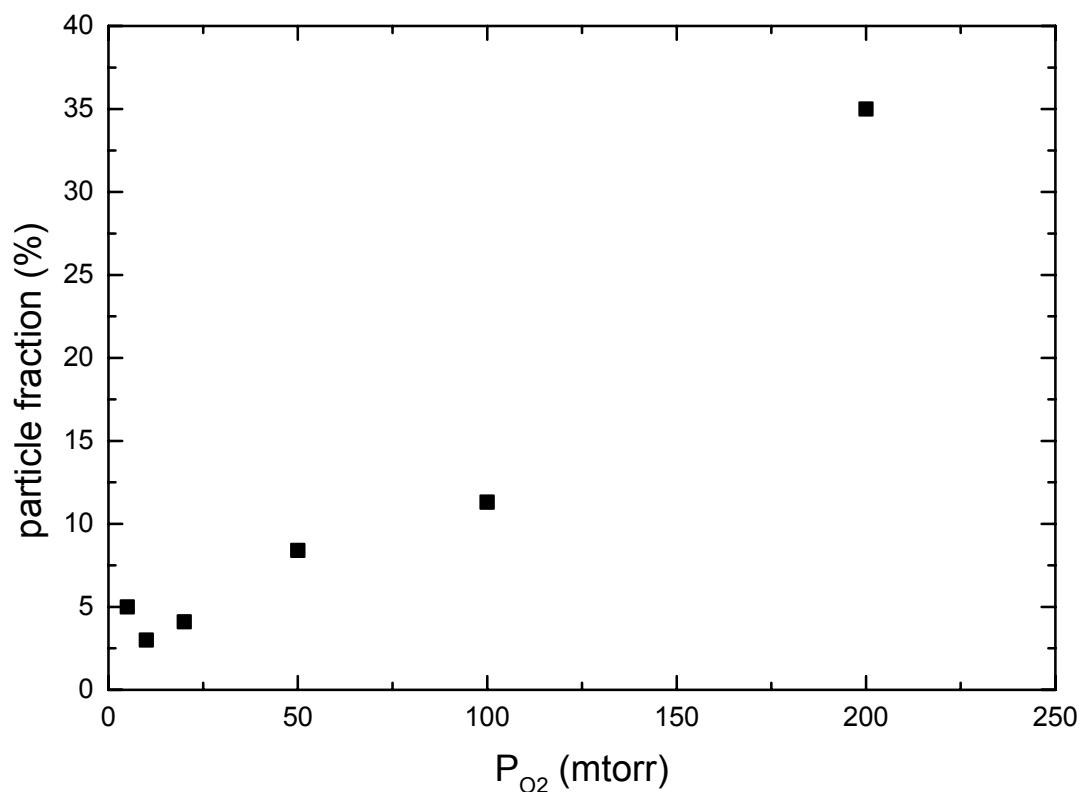


Fig 37: Particle fraction vs. oxygen pressure P_{O_2} .

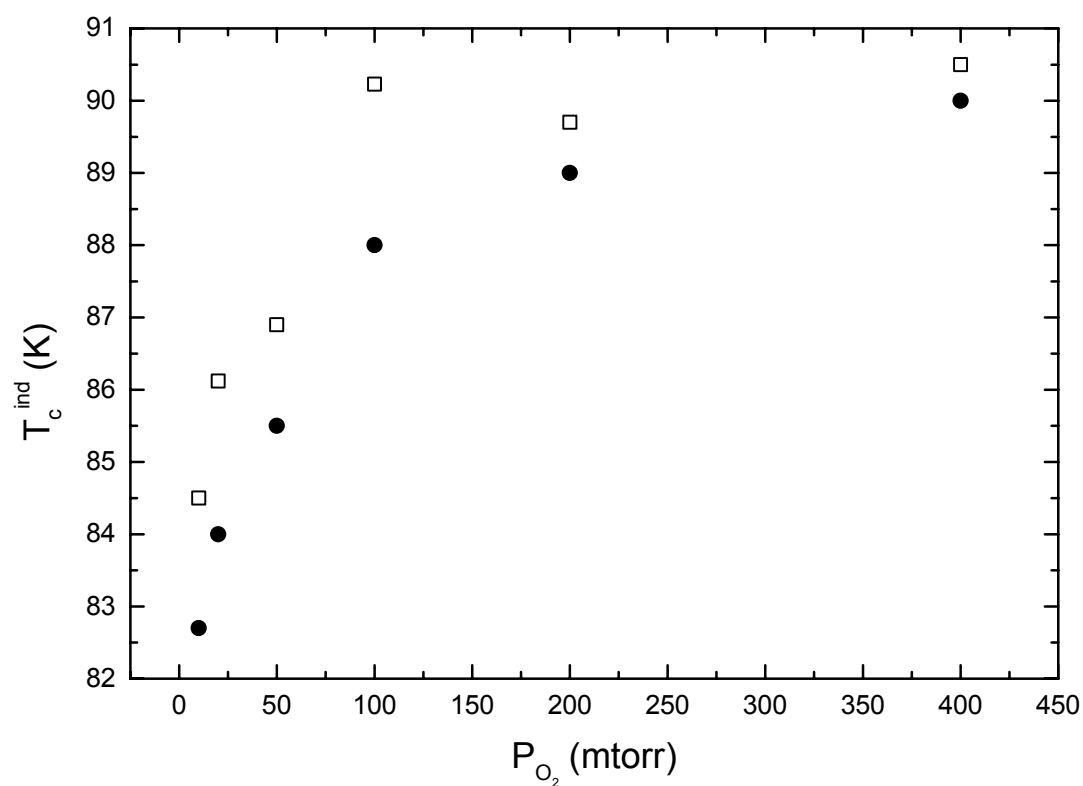


Fig 38: Onset (□) and zero-point (●) of the inductively measured superconducting transition, T_C^{ind} , vs. the oxygen pressure P_{O_2} .

A linear correlation has been found between T_C and the c-axis lattice constant (Fig 39),

which is distinctly different from dependencies obtained either for bulk material, where T_C has been reduced by oxygen deficiency [54], or by 300keV proton irradiation [55]. Instead the correlation between T_C and the c-axis lattice parameter found in this work coincides with that obtained by Schneider et al. [56] and Krupke et al. [57]. In [56] YBCO-films were deposited under controlled ion bombardment using a bias sputtering process and in [57] $Gd_1Ba_2Cu_3O_{7-x}$ films were deposited in an electron cyclotron supported sputtering system, at different target voltages, and with different copper content.

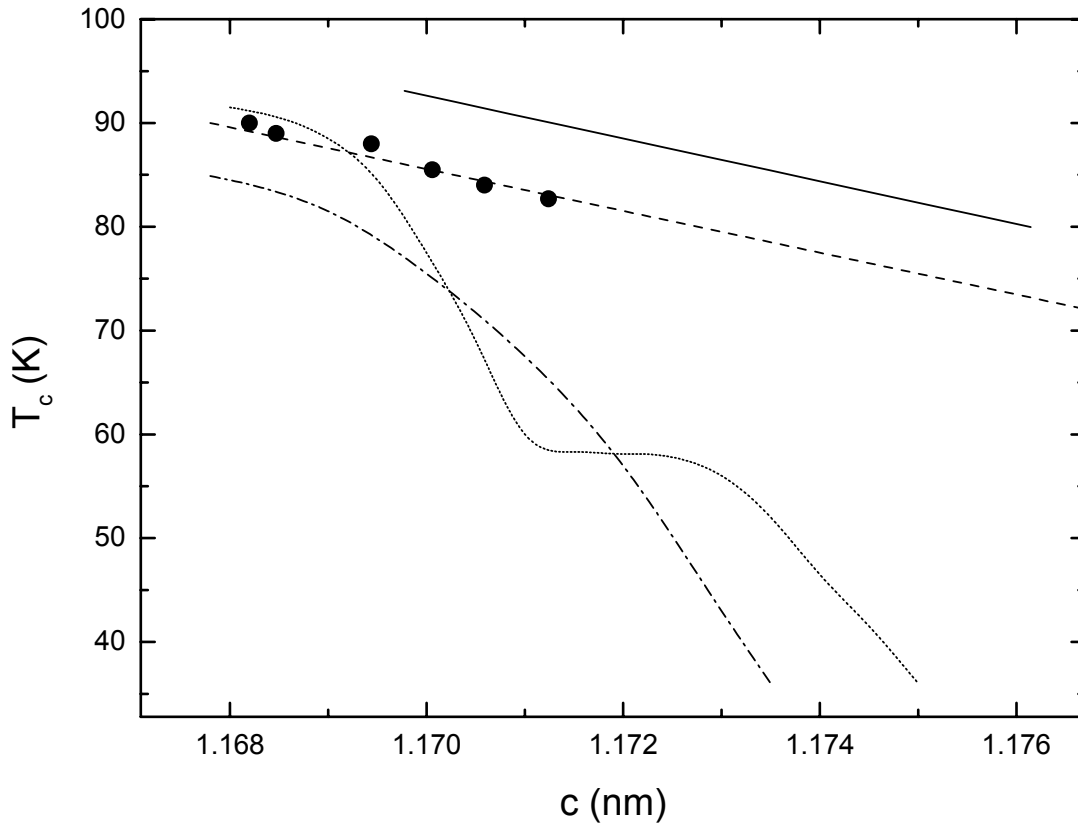


Fig 39: Superconducting transition temperature, T_C , vs. c-axis lattice constant, c , for films deposited at different oxygen pressure (●). Included are data of oxygen depleted material (···) [54], irradiated films (---) [55], films prepared by bias sputtering (-·-) [56] and films prepared at different target voltages (—) [57].

The fact that the relation between T_C and c-axis lattice constant is similar in oxygen deficient, copper deficient, and low energetic ion bombardment damaged films may indicate that the underlying defect structure [58,59] is the same, or that different defect structures can cause the same correlation. This subject however has not been further explored.

For this work the more important result is the fact, that YBCO films with $T_C=90K$, could only be grown with P_{O_2} close to the stability line of CuO. This is perhaps not surprising if one keeps in mind that the growth conditions of single crystals are also located within the stability region of CuO (Fig 36). Yet c-axis oriented YBCO films contain the secondary phase CuO

while single crystals do not. The absence of the secondary phase CuO in stoichiometric single crystals can be explained by YBCO being the thermodynamically more stable compound. Thin film deposition, however, is a non-equilibrium process in which thermodynamic has to compete with kinematics. In that case the fast growth rate of CuO enables the compound to compete against c-axis oriented YBCO, if the growth conditions are close to the stability region of CuO and if CuO nucleation sites are present.

The conclusion is that c-axis oriented YBCO films with $T_c=90\text{K}$ can be grown without CuO particles, only if the growth is a quasi-equilibrium process, which means growing at an ultralow rate as done by Tazoh et al. [60], or in the absence of CuO nucleation sites. For practical reasons the film process should be as short as possible. Therefore it was tried to satisfy the last condition. During that work the PST process was developed which is introduced in the next paragraph.

5.1.4 The Pressure Controlled Self-Template Process (PST)

It is known that CuO nucleates on the surface of substrates used for the growth of high temperature superconductors. Several authors report on the influence of the substrate surface on the density of CuO particles [61,62]. However, from those reports it is not clear if YBCO itself provides nucleation sites for CuO. The PST process offers a way to study this question.

The underlying idea of the PST process is to grow first a few unit cells thick YBCO film under conditions for which CuO particles do not nucleate, even if nucleation sites are present. As shown above this can be achieved at P_{O_2} away from the CuO stability region and close to the YBCO decomposition line. This thin layer shields any CuO nucleation sites on the substrate and acts as a buffer layer. In a second step, without interrupting the growth, P_{O_2} is raised to the CuO stability region, and stabilised. If CuO nucleation sites are present at the YBCO surface CuO particles will nucleate and the surface would not be different from that of a film grown at high P_{O_2} from the beginning. Fig 32d shows the surface of a film grown with the PST process. The surface is relatively smooth and there are no CuO particles present, except for few $BaCuO_2$ particles as identified with EDAX. This demonstrates clearly that YBCO provides no CuO nucleation sites. The same result is also obtained for different substrates and different substrate cleaning procedures. This is not in contradiction with publications describing the influence of the substrate surface on CuO particle nucleation [62], because in this work the first thin YBCO layer acts as a buffer layer against imperfections and intrinsic nucleation sites. The superconducting transition of PST films occurs at $T_c=90\text{K}$, the same temperature as for films which were grown at high P_{O_2} from the beginning. It was not possible to detect any sign of the superconducting transition of the thin YBCO-buffer layer,

which may have a lower T_C .

In summary it has been shown that a proper adjustment of the rf-power and of the H_2O pressure provides hole free YBCO films and an enhanced target lifetime. The function of the H_2O additive is either to enhance the dissociation of molecular oxygen or to reduce the recombination of atomic oxygen, which in both cases gives a high atomic oxygen pressure. The high atomic oxygen pressure, together with a low rf-power, guarantees oxidation of all cations, including Barium and Copper. Under these conditions an excess of Yttrium due to different vapour pressures is prevented and no hole formation is observed. The optimised sputter conditions are reflected by a constant and reproducible dc-bias, a high reproducibility of the film properties and an enhanced target lifetime.

The film properties versus the molecular oxygen pressure have been investigated. At low oxygen pressure, close to the stability line of YBCO, films were grown with fewer particles, but the lattice constant was enhanced and the T_C reduced. With increasing oxygen pressure towards the stability region of CuO, T_C increases and the lattice constant decreases but the surface becomes very rough due to CuO particles. The observed linear correlation between T_C and lattice constant was pointed out as well as the connection between growing in the stability region of CuO and obtaining defect free YBCO.

The PST process was introduced in order to merge the benefits of the low and high oxygen pressure regimes. In that method the first layers of YBCO are grown at a low oxygen pressure, far away from the stability region of CuO. This prevents nucleation of CuO on the substrate surface. Then the oxygen pressure is raised to the stability region of CuO and films with $T_C=90K$ are obtained. The fact that films grown with the PST do not include CuO particles leads us to the conclusion that there are no nucleation sites for CuO particles on YBCO.

5.2 a-Axis Oriented $Y_{1-x}Ca_xBa_2Cu_3O_{7-y}$ Films

5.2.1 The Template Process

For many years a-axis oriented YBCO films had inferior transition temperatures. The reason for that is the low deposition temperature at which the phase grows preferentially. Although the maximum deposition temperature depends in a complex manner on the substrate material, the rate and oxygen pressure [28,29] it was not possible to reach deposition temperatures close to those for c-axis orientation.

The breakthrough came with the use of a $Pr_1Ba_2Cu_3O_7$ (PBCO) template layer by Hontsu et al. [30]. The growth of the template layer starts at low temperature to ensure a-axis orientation. Then the temperature is raised to deposition temperatures typical for c-axis orientation. Finally the YBCO is grown onto the template layer. In this way a-axis oriented YBCO with T_C above 80K can be grown.

In this work that process has been optimised within the limitations of the sputtering system. In that way, the best a-axis oriented films have been grown at 160mtorr O_2/Ar at 95W rf/dc power, where the PBCO growth started at 625°C before and ended at 690°C. The whole YBCO layer was grown at 690°C. The characterisation of these films yielded that the YBCO layer was purely a-axis oriented with a resistive transition onset of 90K. However the samples were not useful for tunneling experiments since the zero resistance temperature was very low and irreproducible, varying between 20K and 75K, and the surface roughness was very large and varied between 300Å and 500Å.

A more promising process included the variation of pressure instead of temperature. Non c-axis growth of the PBCO template layer was enforced by a reduced total pressure of 80mtorr, causing an increased growth rate. Only after the initial growth of YBCO, the pressure was raised to 160mtorr. In that way the temperature could be kept at 700°C during the whole growth. In fact, Fuchs et al. had already applied this process [63].

The overall sample quality was significantly improved. The superconducting transition occurs reproducibly between 87 and 91K and the surface roughness measures between 70 and 150Å. XRD revealed that the PBCO layer is mainly a-axis oriented with traces of c-axis orientation (Fig 40). Due to the lattice mismatch between the c-axis lattice parameter of LSGO and the b and c lattice of PBCO, c-axis oriented growth direction is indeed favoured over a- or b-axis growth close to the interface [63]. The YBCO layer itself is fully a-axis oriented as can be seen from the absence of the (002) and (004) reflexes. The a-axis lattice parameter of YBCO, with 3.80-3.81Å was close to the bulk value. Mosaic spreads were

measured between 0.3° and 0.6° . A small peak could be identified as the (200) reflex of the secondary phase PrBaO_4 .

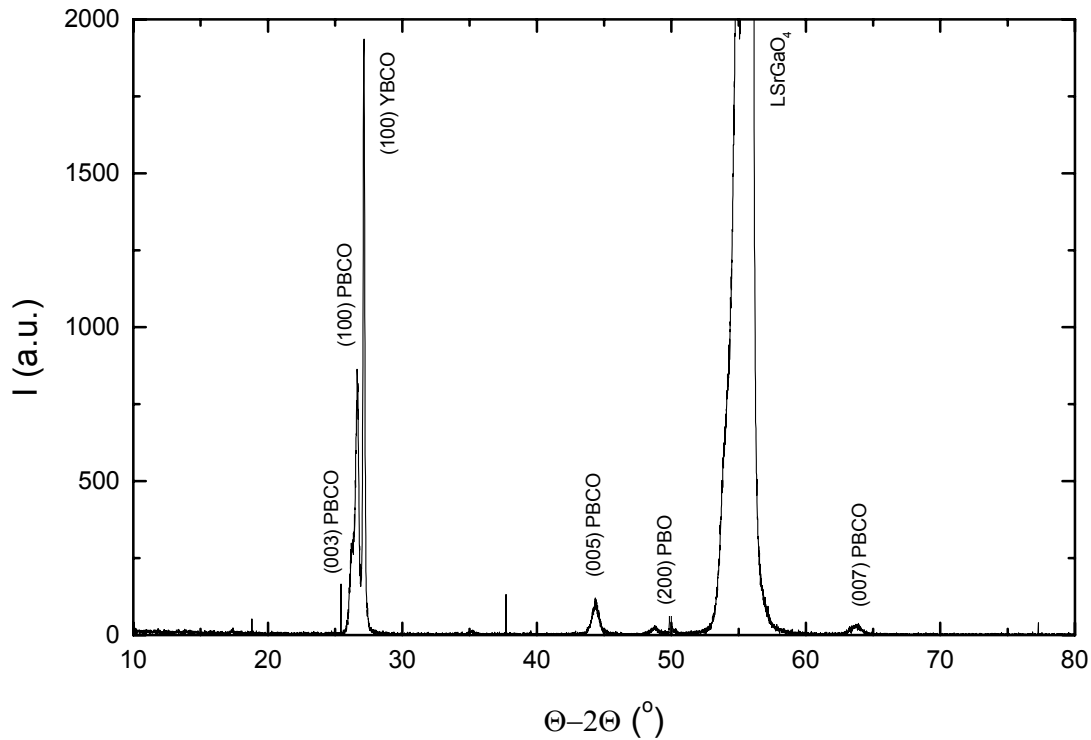


Fig 40: XRD pattern of an optimally doped a-axis oriented YBCO thin film grown on (100)- LaSrGaO_4

5.2.2 In-plane Orientation

In this work all $\text{Y}_{1-x}\text{Ca}_x\text{Ba}_2\text{Cu}_3\text{O}_{7-y}$ films with a-axis orientation were grown on LaSrGaO_4 . Due to the tetragonal structure of this substrate [63], in-plane orientation of the b-axis [010] and the c-axis [001] was achieved in most samples. As a result, a large electrical anisotropy of the resistivities, ρ_b and ρ_c , is observed (Fig 41). In the optimally doped samples the resistivities at 100K were of the order of $\rho_b \approx 100\mu\Omega\text{cm}$ and $\rho_c \approx 10\text{m}\Omega\text{cm}$. ρ_b decreases linearly with temperature, while ρ_c shows a crossover between a semiconducting-like and a metallic-like behaviour at a temperature T^* , which varies from sample to sample between 125K-175K. Currently there is no consensus about the important mechanisms contributing to c-axis transport, however a semiconducting-like behaviour seems to be intrinsic [64]. The linearity in ρ_b is typical for optimally doped samples and shows the presence of strong electron-electron scattering. A typical surface of a film with a large electrical anisotropy, as seen in the optical microscope and the AFM, is shown in Fig 43 and Fig 42, respectively. In the AFM pictures the in-plane alignment is visible due to the alignment of YBCO grains. The longer side of the grains is parallel to the (010)-axis and the shorter one parallel to (001) [63].

Although it is likely that the films are continuous and that the intrinsic anisotropy is

measured, one has to keep in mind that grain boundaries may alter the measurement.

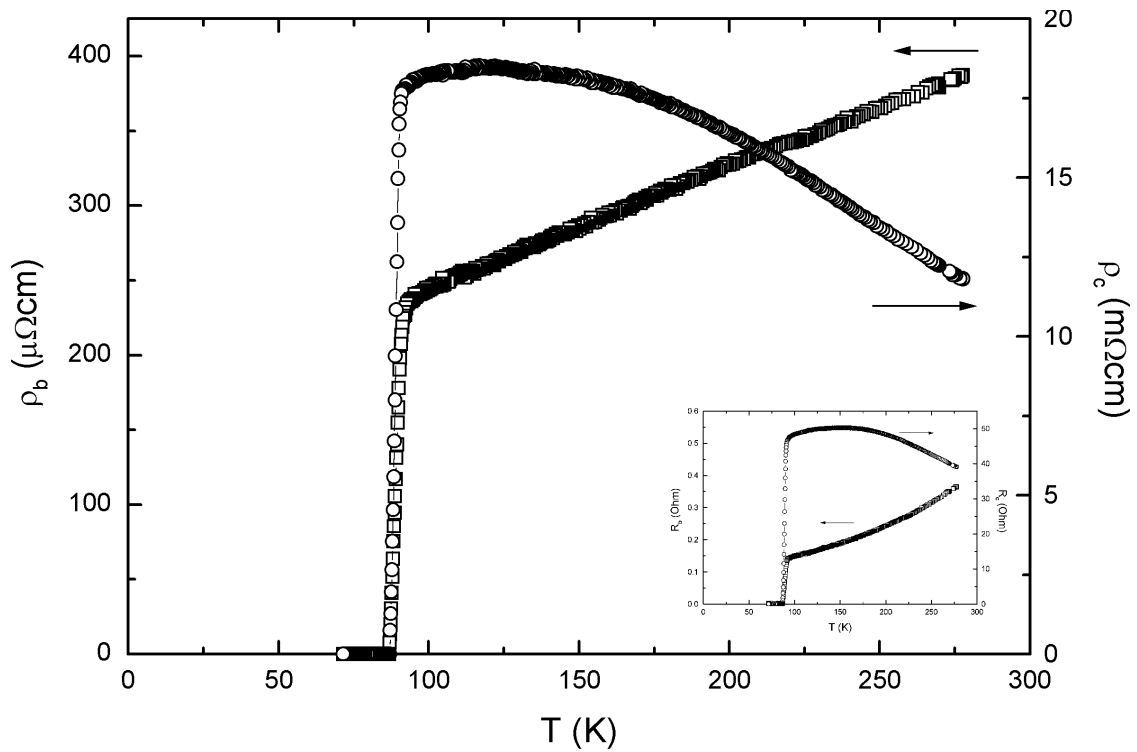


Fig 41: Resistivity ρ_b (■) and ρ_c (○) vs. temperature T of an optimally doped, in-plane oriented a -axis YBCO thin film. $T_C = 87-91K$. The inset shows the raw data. R_b and R_c . Note the difference in the temperature dependence between the measured resistance and calculated resistivity due to the square geometry (chapter 4.1).

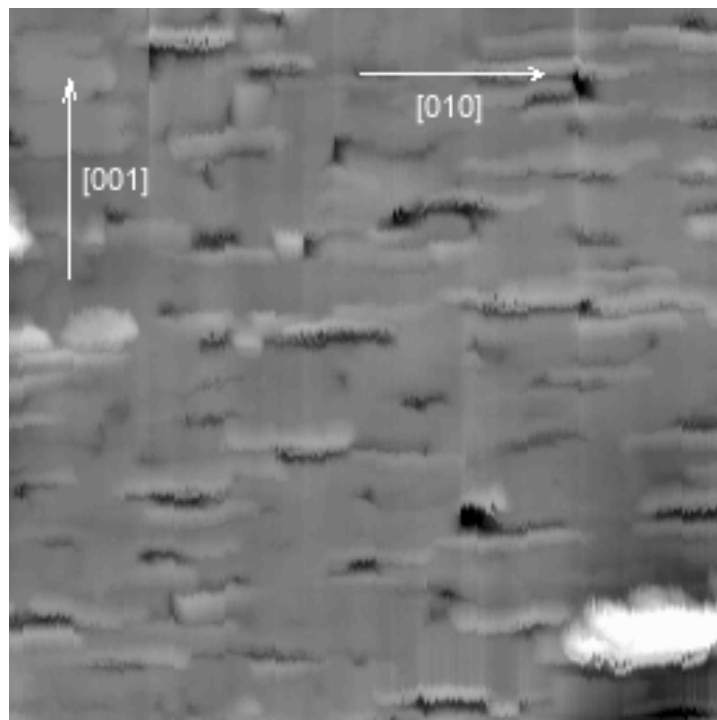


Fig 42: AFM micrograph of an in-plane oriented, a -axis YBCO thin film (picture width equals $5\mu m$).

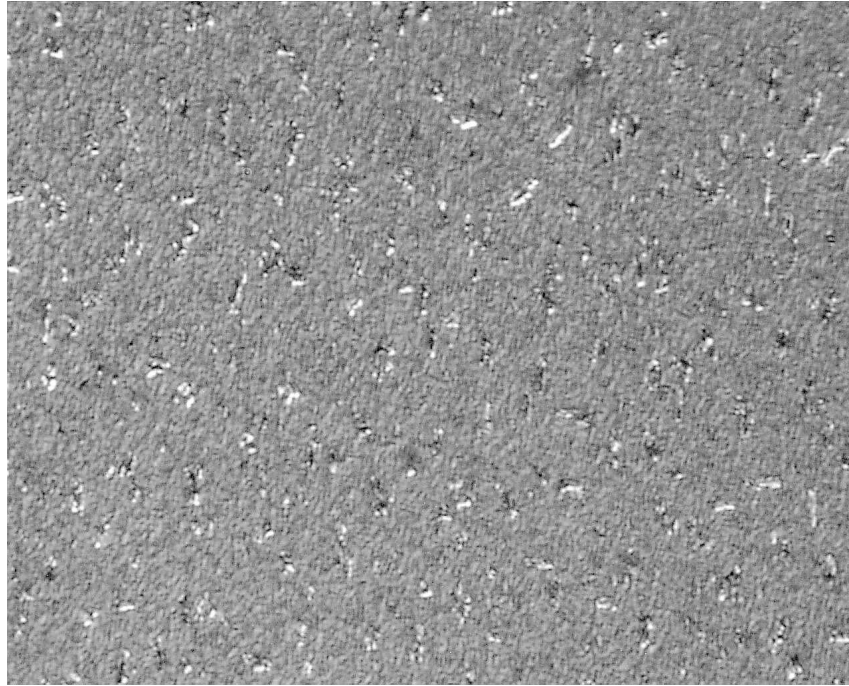


Fig 43: Optical Micrograph of an in-plane oriented a-axis YBCO thin film (picture width equals 200 μ m)

From the crystallographic point of view, in-plane oriented YBCO films are similar to untwinned single crystals, since all crystallographic axes are macroscopically aligned. This is very important for the interpretation of the tunneling data. The dimensions of the samples were typically 7x7mm² with a thickness of the YBCO layer being estimated as 3000Å.

5.2.3 Oxygen Underdoped Samples

Underdoped YBCO samples were grown under identical conditions as optimally doped samples. However, instead of cooling down in 1atm oxygen the samples were annealed at 350°C and 10mtorr oxygen. In such samples, T_C is reduced below 60K as expected for underdoped samples. As can be seen in Fig 44, also in under doped samples an anisotropy of the resistivities is observed, with $\rho_b \approx 1\text{m}\Omega\text{cm}$ and $\rho_c \approx 10\text{m}\Omega\text{cm}$. However a significant difference can be observed in the temperature dependence between the optimally doped and underdoped samples. The b-axis resistance shows down to T_C an upward curvature, whereas the c-axis resistance becomes metallic like below 120K. The superconducting transition of these samples is also significantly wider with the transition onset at 58K and zero resistance at 47K. The crystallographic structure of the underdoped samples is identical with the overdoped samples, except that the a-axis lattice parameter is with 3.82Å slightly larger than for the optimally doped samples (Fig 45). The surface morphology is similar to Fig 42 and Fig 43 with no significant difference in the surface roughness.

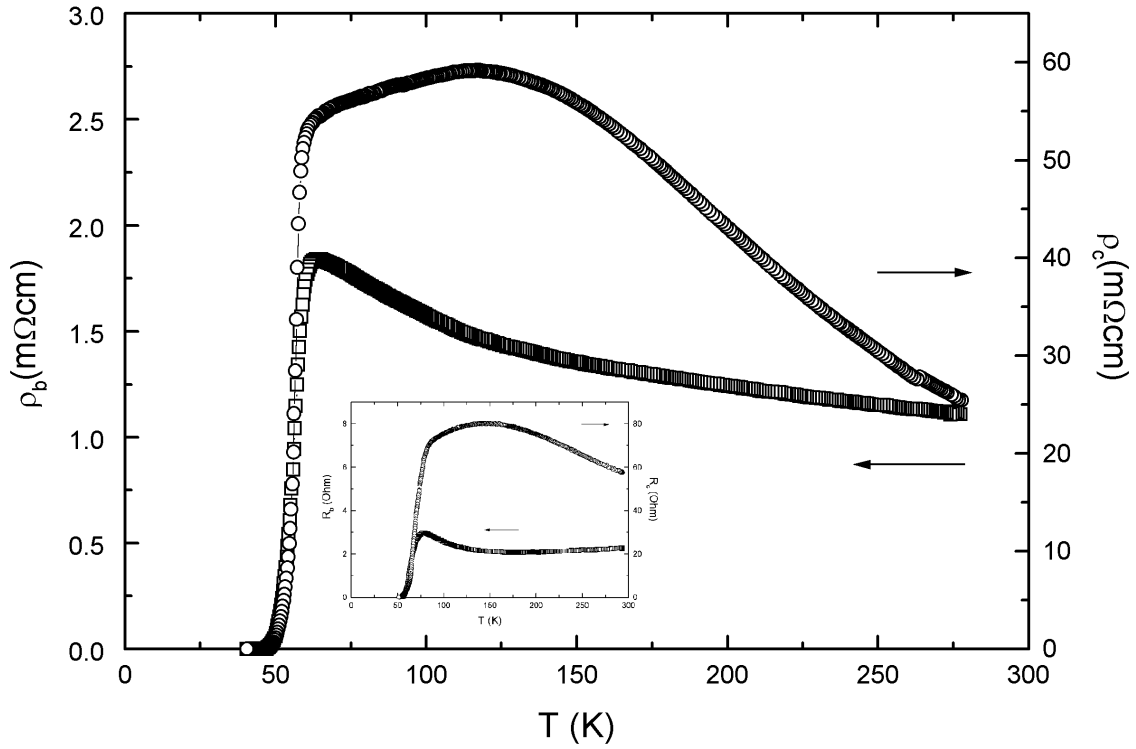


Fig 44: Resistivity ρ_b () and ρ_c (O) vs. temperature T of an oxygen-underdoped, in-plane oriented a -axis YBCO thin film. $T_c = 47$ - 58 K. The inset shows the raw data (see chapter 4.1).

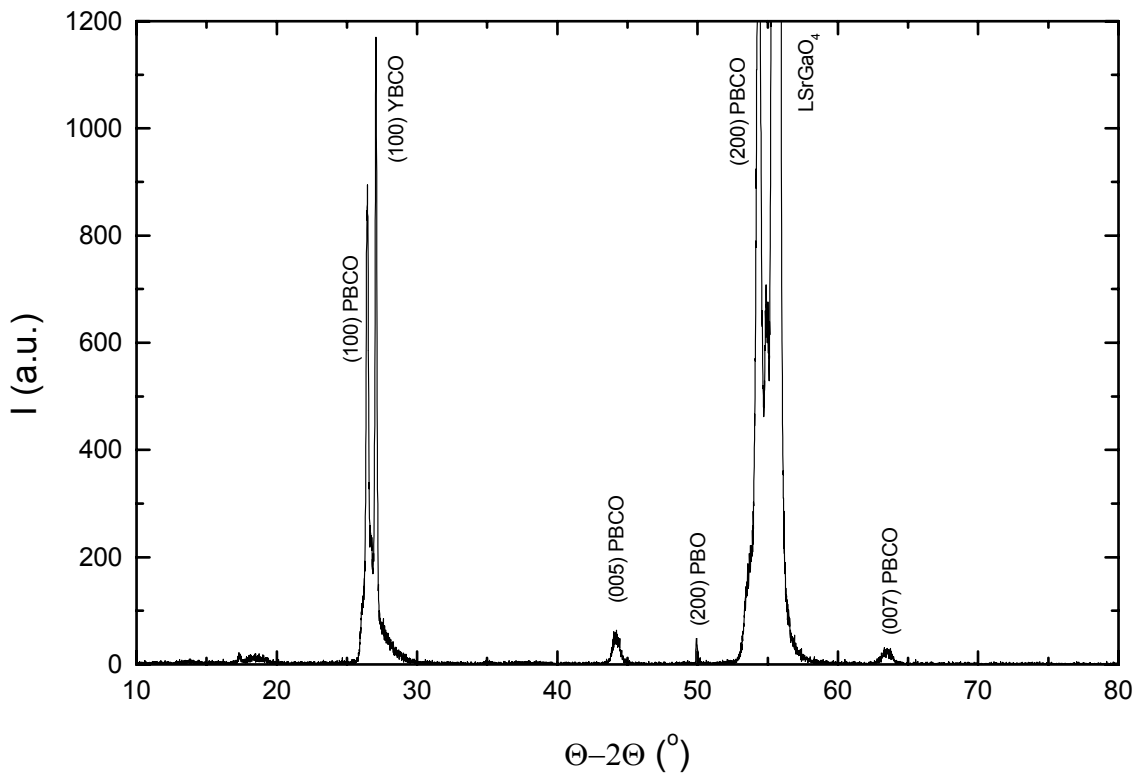


Fig 45: XRD pattern of an oxygen-underdoped a -axis oriented YBCO thin film grown on (100)-LaSrGaO₄.

5.2.4 Calcium Overdoped Samples

Calcium overdoped samples were grown by sputtering from a $Y_{0.8}Ca_{0.2}Ba_2Cu_3O_{7-x}$ target.

The growth process was identical to the growth of optimally doped YBCO samples. The XRD pattern is similar to optimally and underdoped YBCO (Fig 46). The a-axis lattice parameter and the mosaic spread are typically 3.81Å and 0.3-0.7°, respectively.

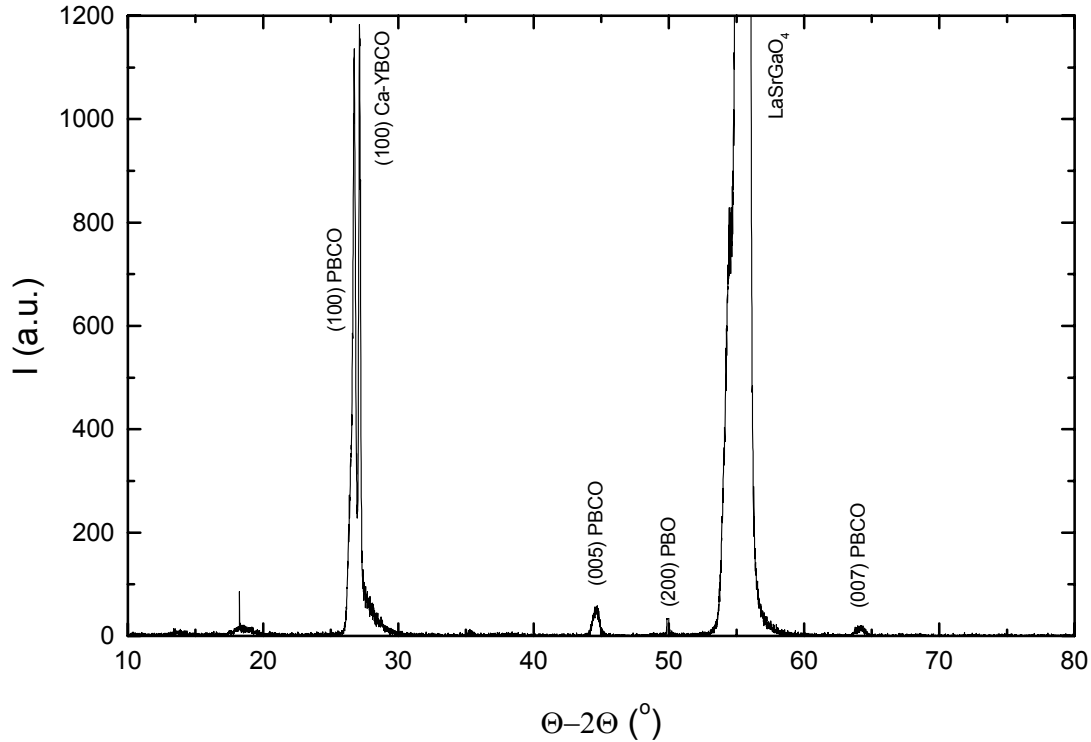


Fig 46: XRD pattern of an overdoped a-axis oriented Ca-YBCO thin film grown on (100)-LaSrGaO₄.

Due to calcium doping T_C is reduced below 75K. A large anisotropy of the resistivity is observed with $\rho_b \approx 10\mu\Omega\text{cm}$ and $\rho_c \approx 100\text{m}\Omega\text{cm}$ (Fig 47). The resistivity in b-direction has a quadratic temperature dependence, which is a signature of conventional electron-electron scattering in a Fermi liquid metal. The c-axis resistivity is metallic-like below $T^* \approx 220\text{K}$, which occurs at significantly higher temperature than in the optimally and under-doped samples. The superconducting transition is wide, as in the case of underdoped samples, with a transition onset around 75K and zero resistance at 53K. This can be due to variation of the doping level, resulting in a much wider transition for samples off the optimal doping (Fig 20 and Fig 21).

The surface morphology is similar to under- and optimally doped samples with a surface roughness between 113Å and 160Å. Also here the AFM picture shows clearly the in-plane alignment of the sample (Fig 48).

This completes the characterisation of the samples, which were subject to tunneling spectroscopy as presented in chapter 7.

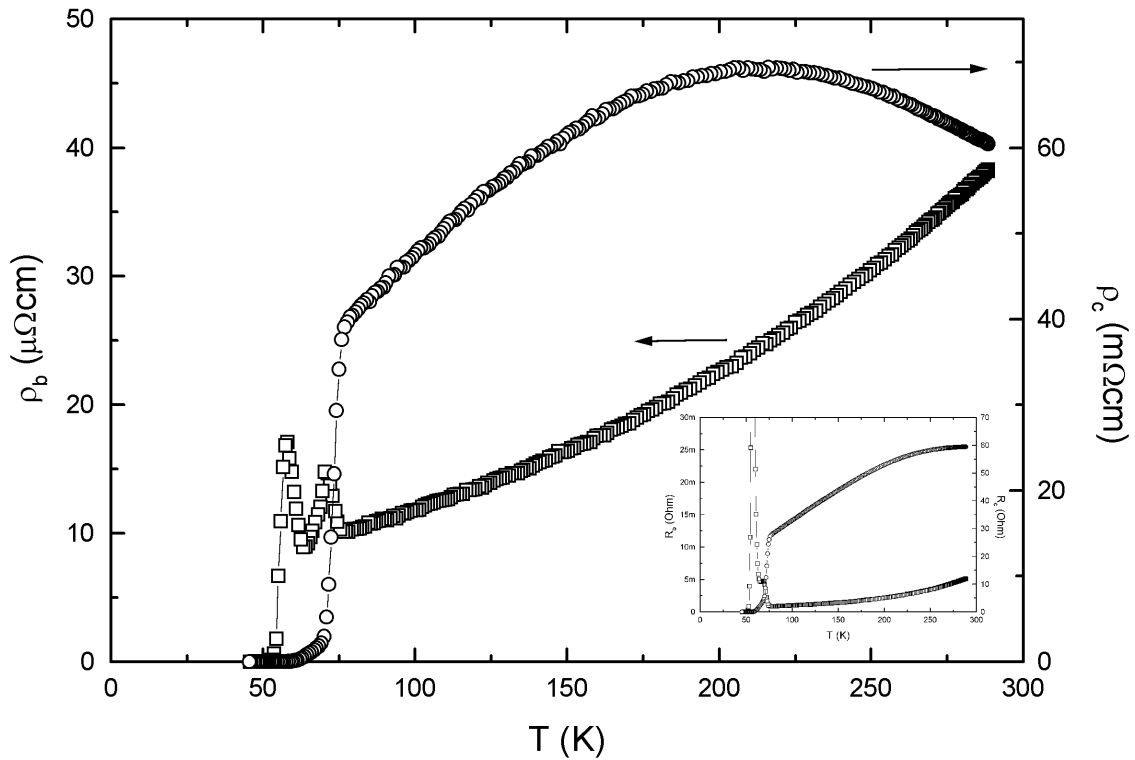


Fig 47: Resistivity ρ_b ($\mu\Omega\text{cm}$) and ρ_c ($\text{m}\Omega\text{cm}$) vs. temperature T of an overdoped, in-plane oriented a -axis $\text{Y}_{0.8}\text{Ca}_{0.2}\text{Ba}_2\text{Cu}_3\text{O}_7$ thin film. $T_C = 53\text{-}75\text{K}$. The inset shows the raw data (see chapter 4.1). Below 75K , local superconducting regions change the current pattern and obstruct the square geometry measurement.

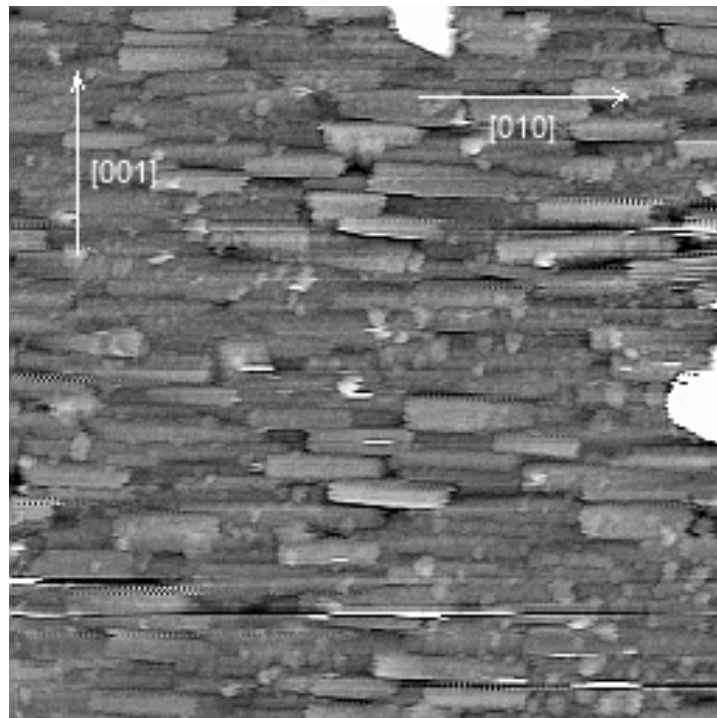


Fig 48: AFM micrograph of an in-plane oriented, a -axis $\text{Y}_{0.8}\text{Ca}_{0.2}\text{Ba}_2\text{Cu}_3\text{O}_7$ thin film (picture width equals $5\mu\text{m}$)

5.3 YBCO on CeO Buffered Ni Tapes

This chapter reports on the results of a collaboration with A. Goyal from Oak Ridge

National Laboratory. The subject is the deposition of YBCO on flexible Nickel substrates by sputter deposition. The so-called rolling-assisted biaxially-textured substrates (RABiTS) were produced at Oak Ridge National Laboratory [65]. These substrates are biaxially oriented and enable the growth of YBCO films with high critical currents due to the absence of high angle grain boundaries [66].

Flexible Nickel substrates of dimensions $3 \times 6 \times 0.1 \text{ mm}^3$ were attached to a resistive heater with silver paint or clamping. Prior to deposition, a vacuum of $6 \cdot 10^{-6}$ mbar was established. After heating the samples, a CeO buffer layer was grown by rf sputtering for 10min under 80mtorr of pure Argon followed by 25min with additional 80mtorr of oxygen. This is to prevent substrate oxidation in the beginning. Without interruption, YBCO was grown by dc sputtering for 3h onto the buffer layer. Cooling down the sample in 1atm oxygen completed the process.

The samples were characterized by means of inductive and resistive T_C measurement, X-ray diffraction and optical microscope.

5.3.1 X-Ray Diffraction

Samples were grown at different temperatures ranging from 650°C to 750°C . At 700°C pure c-axis orientation of the YBCO layer was achieved as can be seen in Fig 49. The lattice parameter is with $c=11.69\text{\AA}$ close to the bulk value for optimally doped samples. The CeO_2 buffer layer did mainly grow in the desired (200) orientation however traces of (111) oriented grains can be seen. Oxidation of the substrate was not prevented as can be seen by the presence of the (111) and (200) reflexes. This obstacle may eventually reduce the critical current density, however it can be avoided by a high temperature annealing prior to growth and by the use of a reductive sputter atmosphere [67].

5.3.2 Optical Microscopy

Optical micrographs of the Nickel substrate and of the YBCO/CeO/Ni multilayer show deep grain boundaries which separate grains of average size $50\mu\text{m}$ (Fig 50 and Fig 51). The visual impression is that YBCO did grow properly on grains but did not in between.

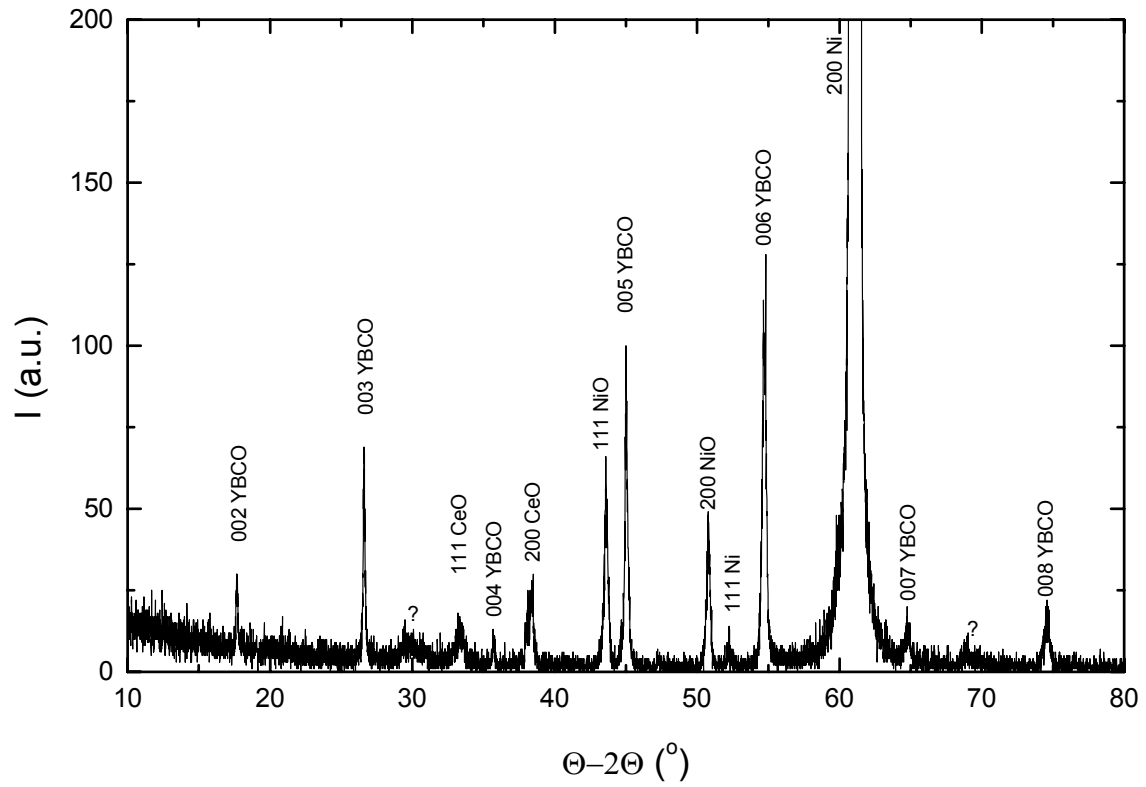


Fig 49: $\Theta-2\Theta$ X-Ray diffraction pattern of the multilayer $Y_1Ba_2Cu_3O_{7-x}/CeO_2/Ni$.

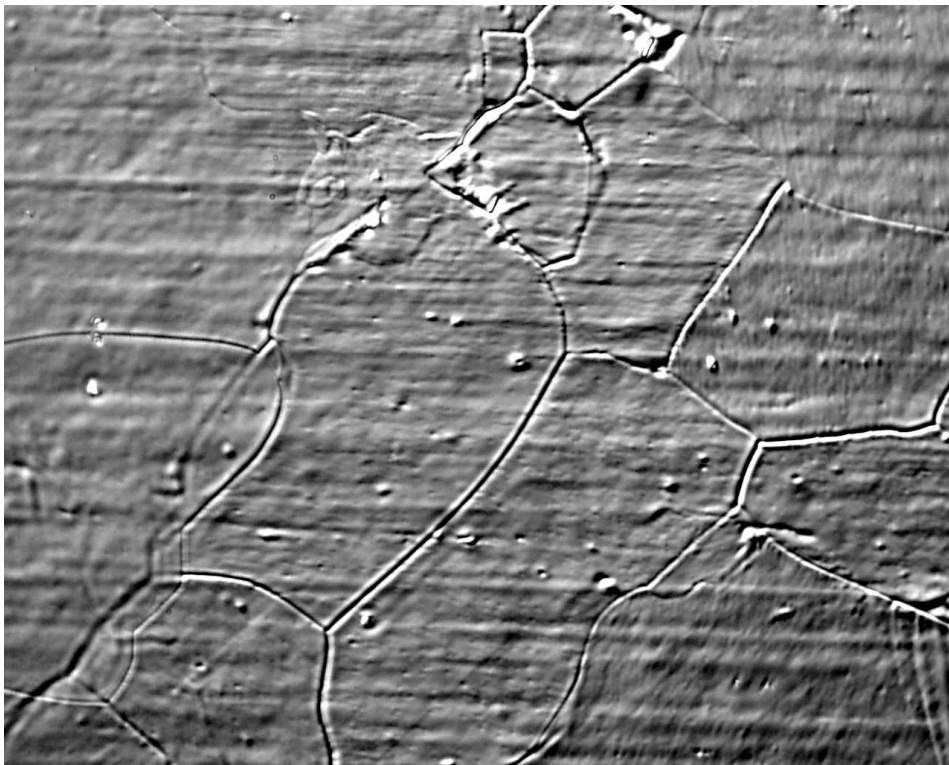


Fig 50: Optical micrograph of the Nickel substrate. Width equals $200\mu m$.

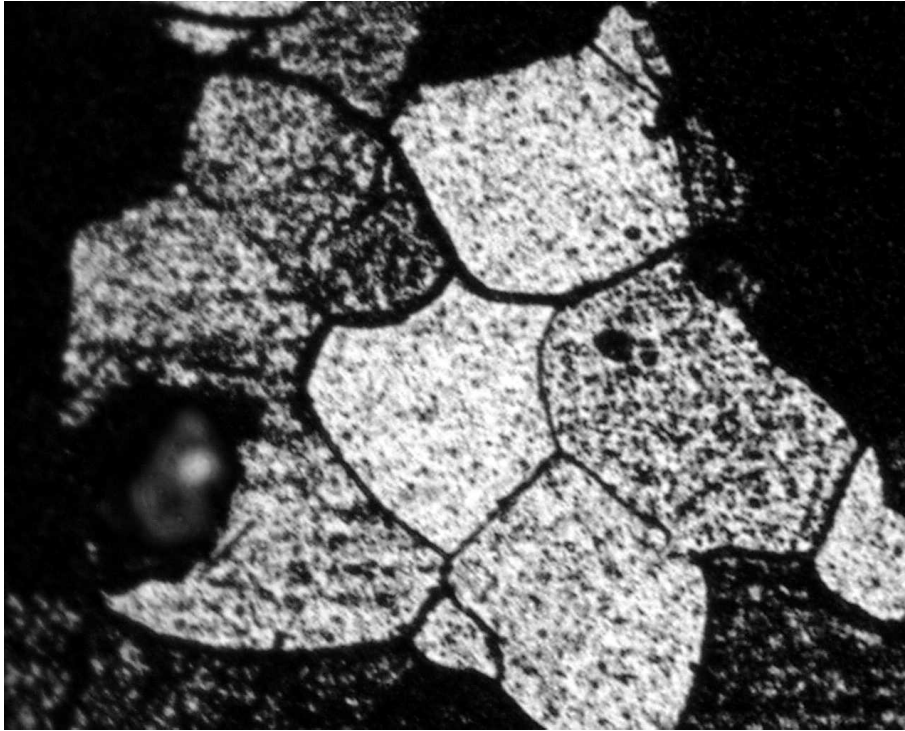


Fig 51: Optical micrograph of the multi-layer YBCO/CeO/Ni. Width equals 200 μ m.

5.3.3 Inductive Measurement

The diamagnetic response of all samples was weak and only significant at low temperature (Fig 52). It shows that the field shielding provided by the sample is not continuous. This is probably due to non-superconducting grain boundaries, which is confirmed by the resistive measurements, as discussed next.

5.3.4 Resistive Measurement

On the sample, which showed the largest diamagnetic response a resistive measurement was performed (Fig 53). The voltage leads were 1mm apart, which is much larger than the average grain size. The temperature dependence is very similar to nonmonotonic resistivity transitions in granular superconducting ceramics [68]. Under temperature reduction the resistance first rises linearly, then drops sharply at T_C and finally decreases linearly with an asymptotic approach of zero resistance.

5.3.5 Conclusion

YBCO films with a high onset temperature were grown on the Ni substrates provided by Oak Ridge National Laboratories. It is concluded that the main obstacle in producing continuously superconducting YBCO films is grain boundaries. In that sense the substrate quality has to be improved.

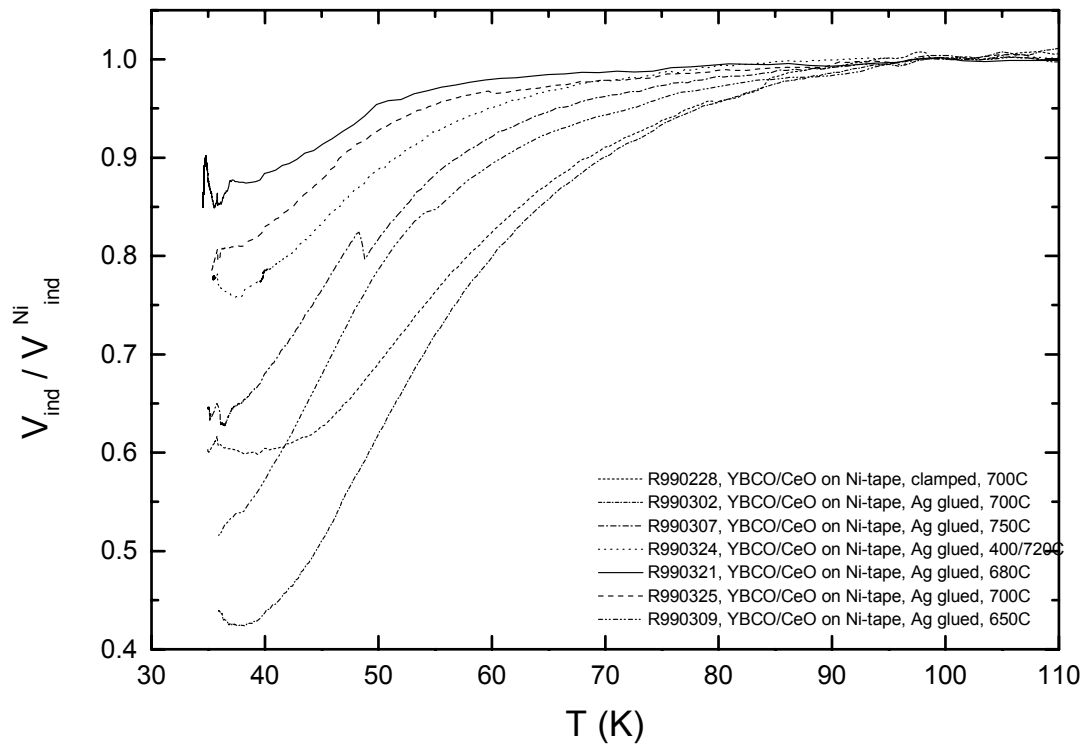


Fig 52: Inductive T_C measurement of several multilayers normalized to the Nickel background.

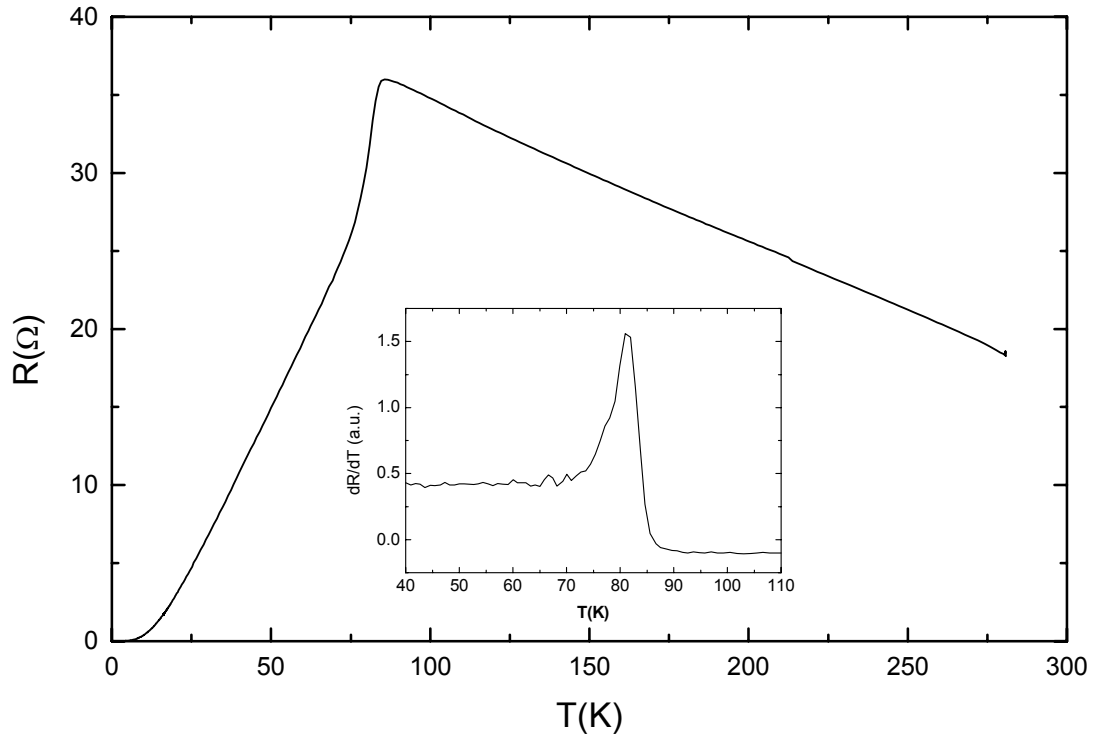


Fig 53: Four terminal measurement of resistance vs. temperature of YBCO/CeO/Ni. The inset shows dR/dT vs. T .

6 YBCO Tunnel Junctions

6.1 CeO Barrier

The conventional way of producing planar tunneling contacts on YBCO is to evaporate a metallic counter electrode onto the ceramic material. The tunneling barrier can be either a so called natural barrier, which is a decomposed surface layer [69] created by exposure of YBCO to air, or an insulating layer created at the interface of YBCO and the metal [70]. The first method lacks control on the barrier properties, while in the second method the oxidation of the metal is due to deoxygenation of the YBCO layer. The growth of an artificial barrier in the form of an oxide layer onto a YBCO layer seems to be a more promising route, especially if done in-situ at temperatures close to the deposition temperature of YBCO. This would prohibit YBaCuO degradation during the in-situ cooling down process, due to part per million impurities of CO₂ and H₂O in the process gas [71]. However the deposition of an oxide at high temperature onto YBCO would prevent oxygen loading at lower temperature. The oxygen loading is believed to be important since the YBCO does not become superconducting otherwise.

Recently we proved that in fact YBCO films grow fully oxidised and remain oxidised if quenched at room temperature. This allows in principal to deposit an oxide layer instantaneously onto the YBCO and avoid decomposition. Since the YBCO film is already oxidised, an oxygen loading, which would be impossible through an oxide layer, is not necessary.

Several materials may be used for artificial barriers such as CeO₂, SrTiO₃, MgO and Al₂O₃. The experiment has been performed with CeO₂ for several reasons: a) growth conditions for CeO₂ are compatible with those of YBCO, b) interface of YBCO grown on CeO₂ is known to be atomically sharp [72] and c) no chemical reaction occurs at the interface.

CeO₂ layers with thicknesses between 2Å and 35Å were grown on (100) oriented YBCO by sputtering at T=700C. The YBCO layer below CeO₂ was fully oxidised and became superconducting at T_C=89K, even in the case of a thick CeO₂ layer. Tunneling experiments however showed that CeO₂ does not grow continuously up to a thickness of 30Å, since the conductivity spectrum was not significantly altered by the CeO₂ layer. Above 30Å the conductivity was reduced by 5 orders of magnitude accompanied by a dramatic change in the shape of the spectrum, unknown for in-plane tunneling. This method was therefore not further exploited. It may be possible to obtain better results on either smoother YBCO films or by the use of a different barrier material. In the following we report on the properties of YBCO/Ag

and YBCO/In contacts which have been used mostly in this work.

6.2 YBCO/Ag Contact

YBCO/Ag contacts are made by placing a drop of liquid silver paint onto the YBCO film surface. The silver paint is a colloid, which contains silver grains in an organic solvent (Iso-Butyl Methyl Ketone). The contact becomes solid once the organic solvent has evaporated. In this work contact areas were of the order of 3mm^2 . Ag paint contacts are generally used in four terminal measurements of the resistivity or critical currents density due to its good electrical and thermal contact. However the conductance spectra of Ag/YBCO contacts are not purely ohmic and show general features of the density of states of YBCO at low temperatures (Fig 76). This leads to the conclusion that part of the conductance is due to tunneling. Whether the tunneling barrier is the above mentioned degradation layer caused by exposure to air, or a layer degraded by the organic solvent is not clear. In any case, the barrier appears to be rather weak or inhomogeneous since the tunneling features are rather soft. Although this cannot be checked (Ag is not a superconductor), a large amount of leakage current is very likely to be present.

6.3 YBCO/In Contact

The conductance spectrum does reflect the density of states in the superconducting state only if most of the conductance is due to elastic tunneling. This requires a strong tunneling barrier with $Z > 1$ and only a small amount of leakage current. For low T_c superconducting materials, tunnel junctions are acceptable if the zero bias conductance (ZBC) in the superconducting state is less than 0.1% of the normal state conductivity [73]. Otherwise it is evidence for gaplessness or for the presence of a metallic short. In general the leakage current can be determined by using a superconducting counter electrode of the BCS type. In the limit $T=0\text{K}$ the ratio between the ZBC with the counter electrode being in the superconducting state and in the normal state determines the percentage of leakage current. At elevated temperature the increase of the ZBC due to thermal smearing of the gap has to be taken into account.

Several BCS superconductors may be used as counter electrodes such as Al, Pb and In. While Al and Pb have to be evaporated, In can be applied also as a pad due to its ductility. Applying the In counter electrode as a pad can be done immediately after the YBCO film growth. It avoids time consuming lithography and therefore minimizes surface degradation.

Most of the junctions in this work have been done by placing fresh cut In pad onto the YBCO surface immediately after the YBCO film growth. The contact area is approximately 3mm^2 . The conductance of these contacts is about three orders of magnitude smaller and the

conductance spectra show sharper features and finer structure compared to Ag/YBCO contacts (Fig 60). This means, that the barrier between In and YBCO is stronger than the barrier between Ag and YBCO. The stronger barrier is possibly Indium oxide created due to contact with YBCO or the prior exposure of In to air.

From the conductance at zero-bias the leakage current in In/YBCO contacts has been estimated to be around 35% (see chapter 8.1). A fit to the low bias conductance spectrum shows that the voltage dependent conductance is due to elastic tunneling, as discussed later.

Evaporation of Al led to unmeasurable high junction resistance, while evaporation of Pb gave gap-like features in the conductance spectrum, which however were completely insensitive to magnetic field and therefore could not reflect the superconducting density of states. Furthermore the superconducting gap of Pb could not be observed below $T = 8K$.

Therefore the best planar tunnel junctions on (100)- oriented YBCO prepared in this work were those with In pads as counter electrode.

In the following table we show the typical order of magnitude of the zero-bias junction contact resistance at $T=4.2K$ obtained on YBCO and Ca-YBCO, for different doping levels and counter electrodes.

| | Ag | In | Pb | Al |
|----------------------|-------------------------|-------------------------|------------------------|-----------------------|
| underdoped YBCO | - | $10\Omega\text{cm}^2$ | - | - |
| optimally doped YBCO | $0.01\Omega\text{cm}^2$ | $1\Omega\text{cm}^2$ | - | $>M\Omega\text{cm}^2$ |
| overdoped Ca-YBCO | - | $0.05\Omega\text{cm}^2$ | $0.1\Omega\text{cm}^2$ | $>M\Omega\text{cm}^2$ |

7 Tunneling into a-Axis Oriented YBCO Films

In-plane oriented (100)-YBCO films, which have been characterized in chapter 5.2, were studied by tunneling spectroscopy. The spectra of optimally doped, underdoped and overdoped samples were measured as a function of temperature and magnetic field: Chapter 7.1 shows the temperature dependence measured in zero magnetic field and chapter 7.2 displays the magnetic field dependence at low temperature. In all tunneling experiments the junctions were wired in such a way, that at positive voltage electrons are tunneling into YBCO.

7.1 Temperature Dependence at $\mu_0 H=0T$

7.1.1 Optimally doped YBCO

The conductance spectra of optimally doped YBCO are shown in Fig 54. The tunnel junction is the interface between YBCO and In. The higher bias background shows a typical parabolic shape, which enables to determine the barrier height $\phi=0.4V$, the barrier width $S=34\text{\AA}$ and the offset voltage $V'=21\text{mV}$ [73].

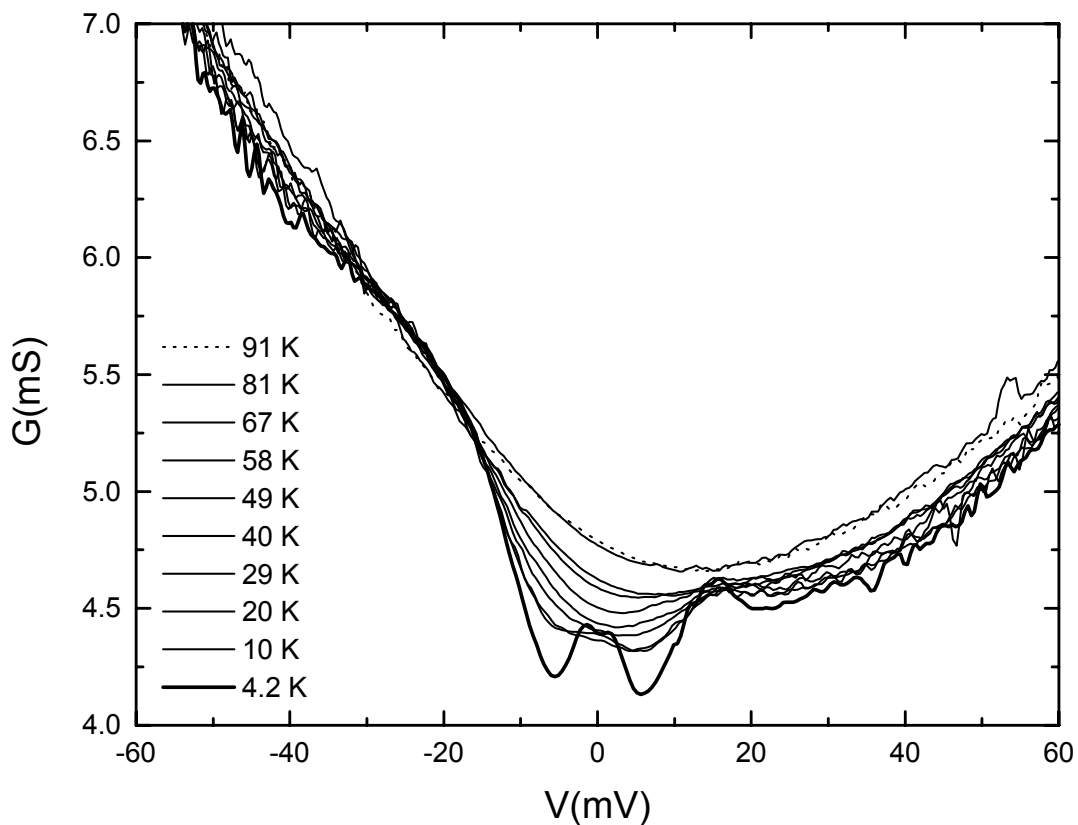


Fig 54: Temperature dependence of the conductance spectrum of an optimally doped (100)-YBCO/In junction in zero magnetic field.

The offset voltage and the observed asymmetry of the spectrum indicate that the tunneling barrier is asymmetric and higher at the barrier side facing the YBCO. At lower temperature a reduction of the low bias conductance is observed as a result of the opening of the superconducting gap. At 4.2K a large gap-like structure is observed at +17mV. At negative bias the structure is less pronounced probably due to the barrier asymmetry.

Below 30K a zero-bias conductance peak (ZBCP) is observed within the larger gap. Below 6K the ZBCP splits into two peaks as can be seen in Fig 55. The splitting between the two peaks at 4.2K is $2\delta=2-3\text{mV}$ and depends on the specific sample. The zero bias conductance at 10K is larger than the conductance of each of the two peaks at 4.2K, and therefore the single peak can not be explained by simple thermal smearing of the two peaks.

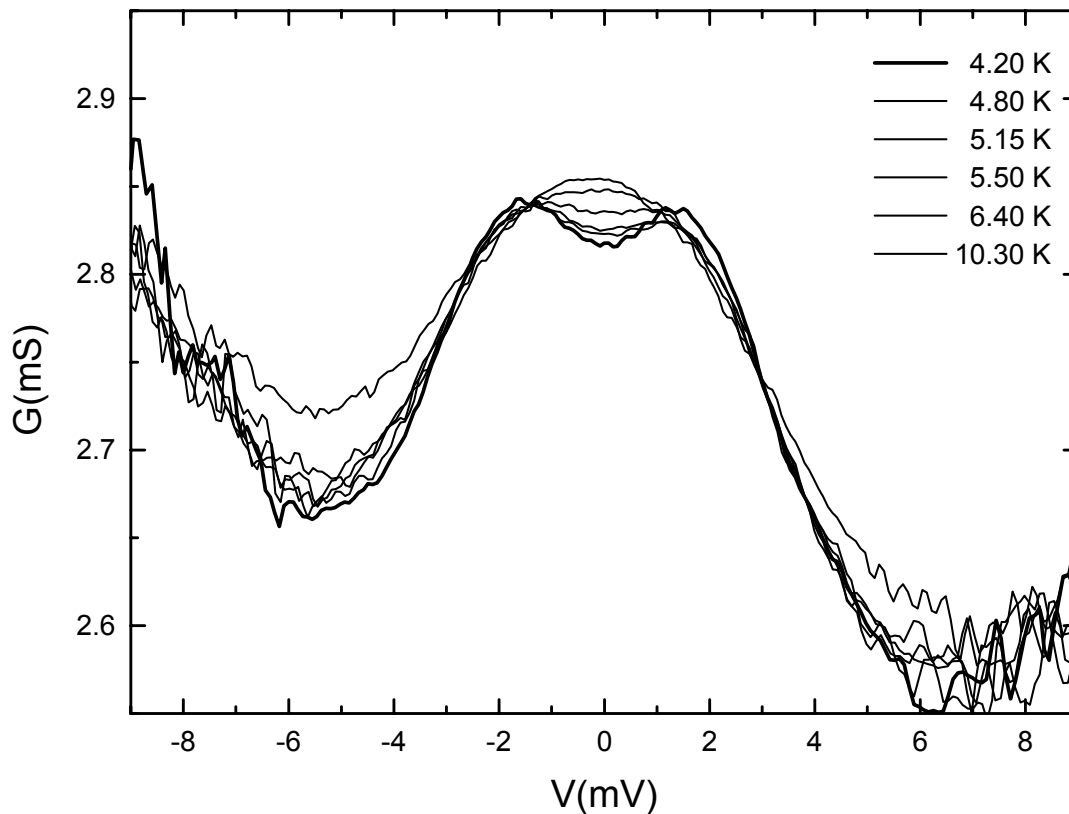


Fig 55: Temperature dependence of the ZBCP. Zero-field splitting is observed below 6K.

7.1.2 Underdoped YBCO

In Fig 56 are shown the conductance spectra of oxygen underdoped YBCO. Also here the higher bias shows a parabolic background, however the asymmetry is smaller as is the calculated offset voltage $V'=8.4\text{mV}$. The extracted barrier height $\phi=0.2\text{V}$ and barrier width $S=51\text{\AA}$ indicate that the insulating barrier is lower and thicker compared to the junction on optimally doped YBCO.

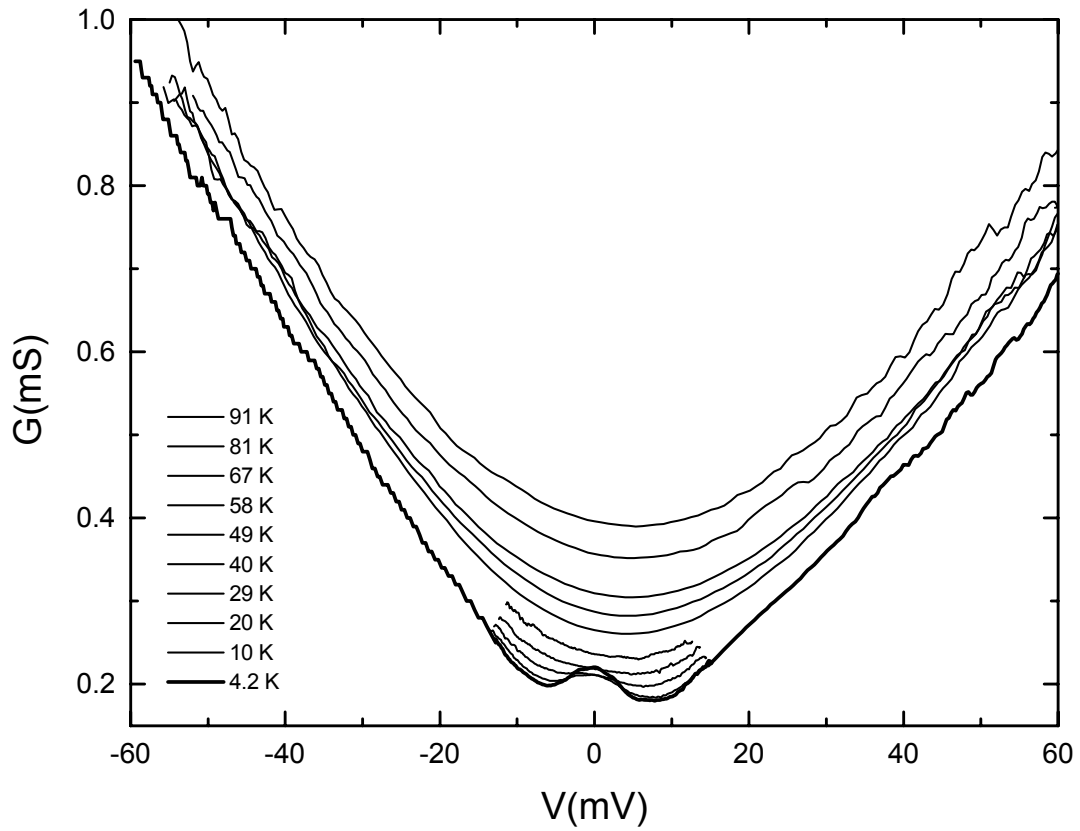


Fig 56: Temperature dependence of the conductance spectrum of an underdoped (100)-YBCO/In junction in zero magnetic field.

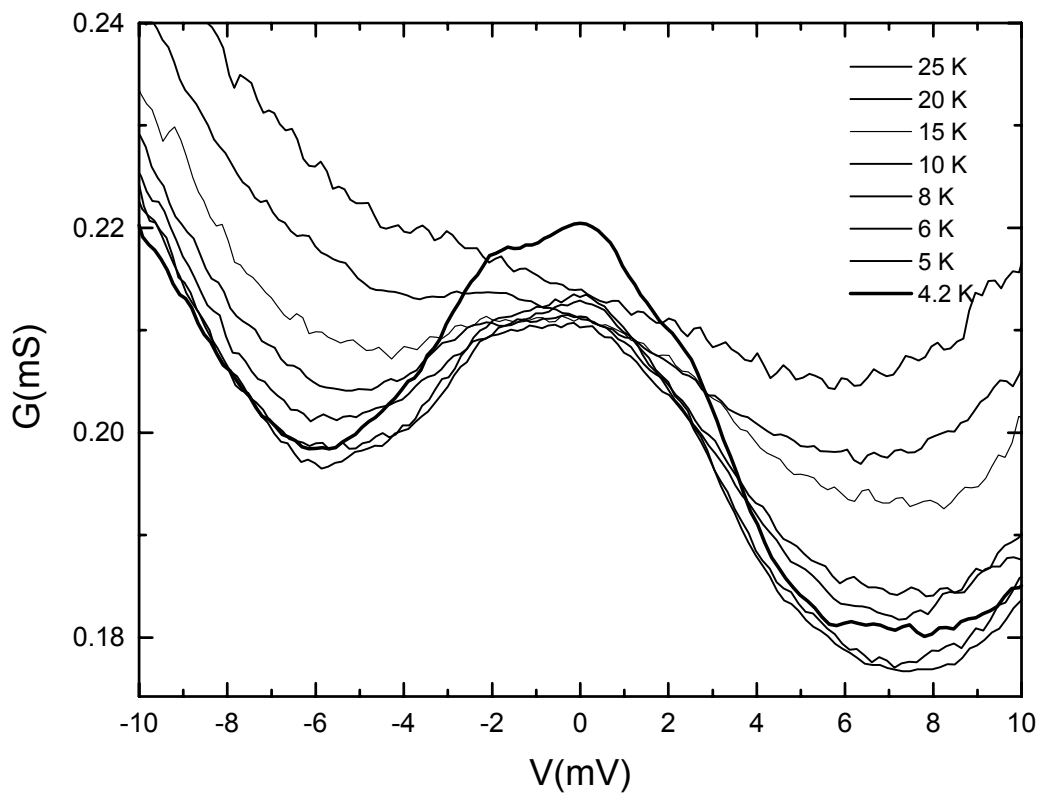


Fig 57: Temperature dependence of the ZBCP.

At lower temperature the low bias conductance is reduced however no gap-like feature is observed except for a weak bump at around 35mV. Between 15mV and 30mV the conductance increases linearly.

Below 25K a ZBCP appears which increases with lower temperature. This ZBCP does not split at any temperature down to 4.2K. However occasionally a deformation of the ZBCP can be observed as in (Fig 57).

7.1.3 Overdoped Ca-YBCO

The temperature dependence of the conductance spectra of calcium overdoped Ca-YBCO is shown in Fig 58. The background at high bias is of parabolic shape and exhibits a large asymmetry and offset voltage $V^0=21\text{mV}$. The barrier height and barrier thickness are $\phi=0.27\text{V}$ and $S=32\text{\AA}$, respectively. Therefore the barrier is similar to those obtained on optimally doped YBCO yet the barrier height is somewhat smaller.

At lower temperature the conductance at low bias is reduced due to the opening of a large gap. No sharp gap is observed, yet the conduction is strongly reduced below 15mV.

Below 12K an additional sub-gap opens (Fig 59). At 4.2K the sub-gap equals 2.5mV. It is important to note that at no temperature a ZBCP is observed.

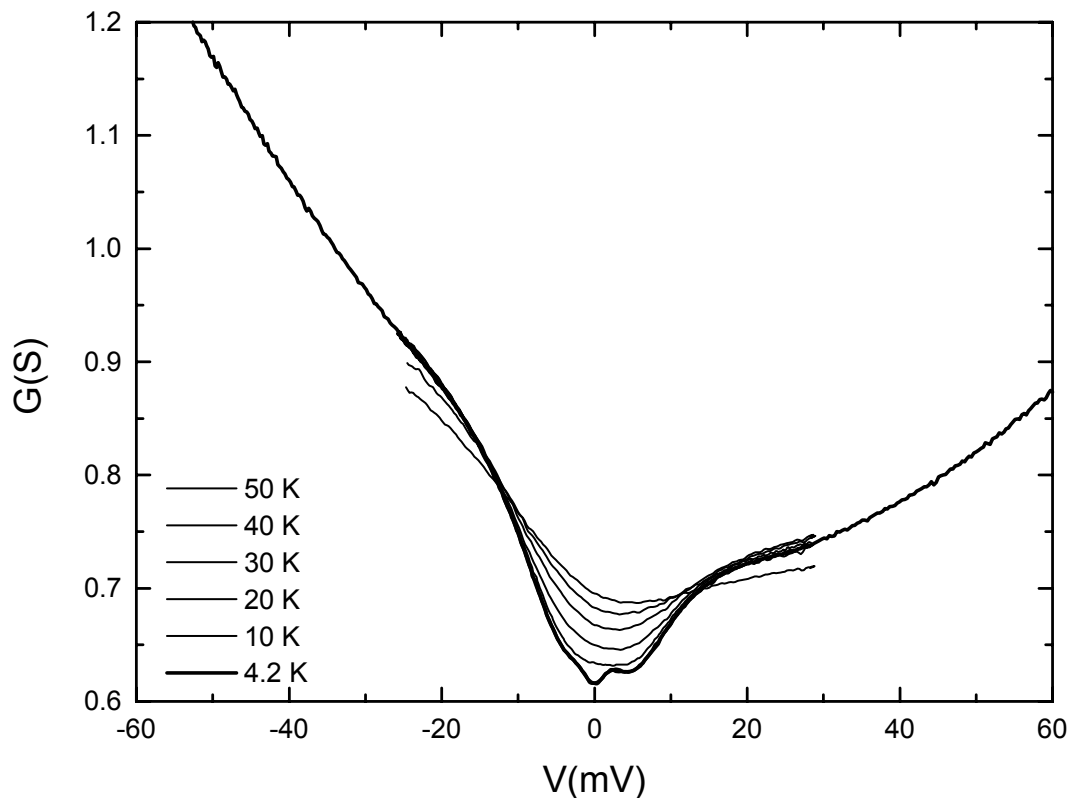


Fig 58: Temperature dependence of the conductance spectrum of an overdoped, (100)-Ca-YBCO/In junction in zero magnetic field.

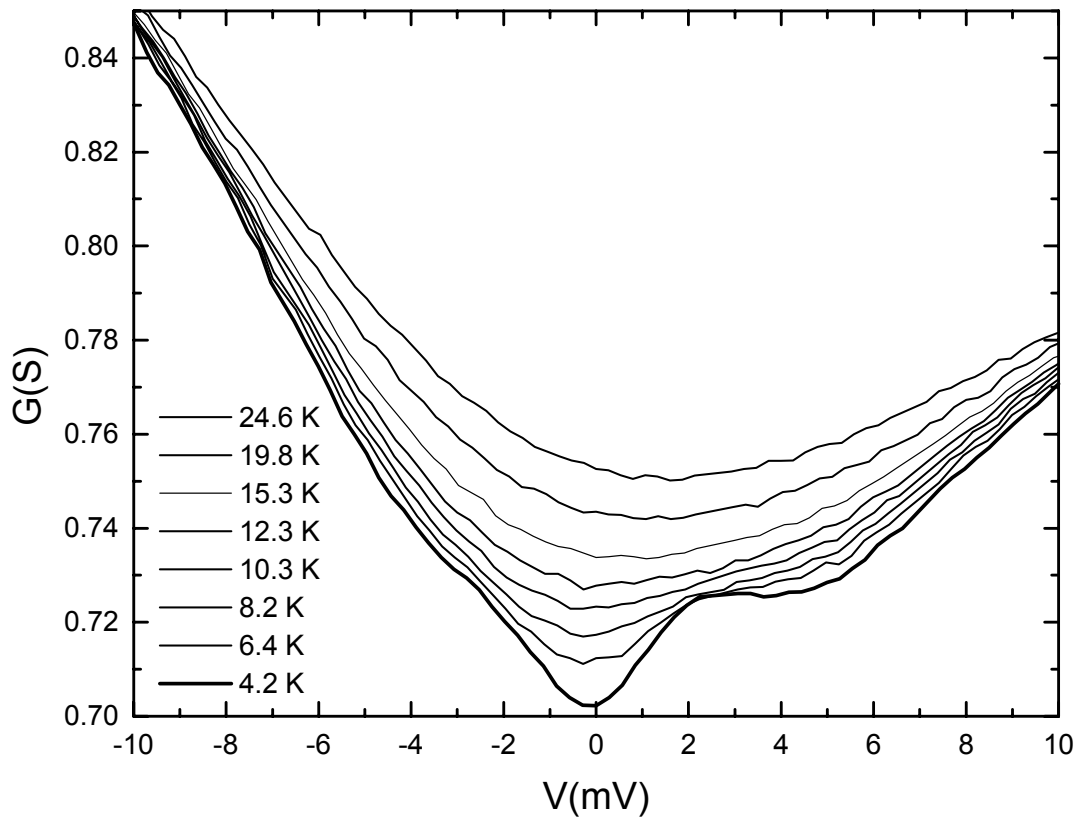


Fig 59: Temperature dependence of the sub-gap.

7.2 Magnetic Field Dependence at T=4.2K

7.2.1 Optimally doped YBCO

The overall magnetic field dependence of the conductance spectra of optimally doped YBCO taken at T=4.2K is shown in Fig 60. The magnetic field is aligned perpendicular to the (100) direction. The following features are observed:

The high bias region, $V > \pm 25\text{mV}$, is within the experimental resolution field insensitive up to $H=6\text{T}$. The broad conductance peak around -20mV is weakly suppressed by the magnetic field. In contrast, the $+17\text{mV}$ peak is strongly suppressed with magnetic field. No significant shift in energy is observed.

The focus is now on the low energy part of the spectrum ($\pm 8\text{mV}$) around the splitted ZBCP. With increasing applied field an increase of the splitting is observed. The splitting is strongly anisotropic and depends on the specific alignment of the magnetic field with respect to the crystallographic orientation of the film. In Fig 61a the magnetic field H is aligned parallel to the c -axis ($H||c$). As H increases the zero-bias conductance (ZBC) diminishes, and the peak position, δ , moves to higher energies.

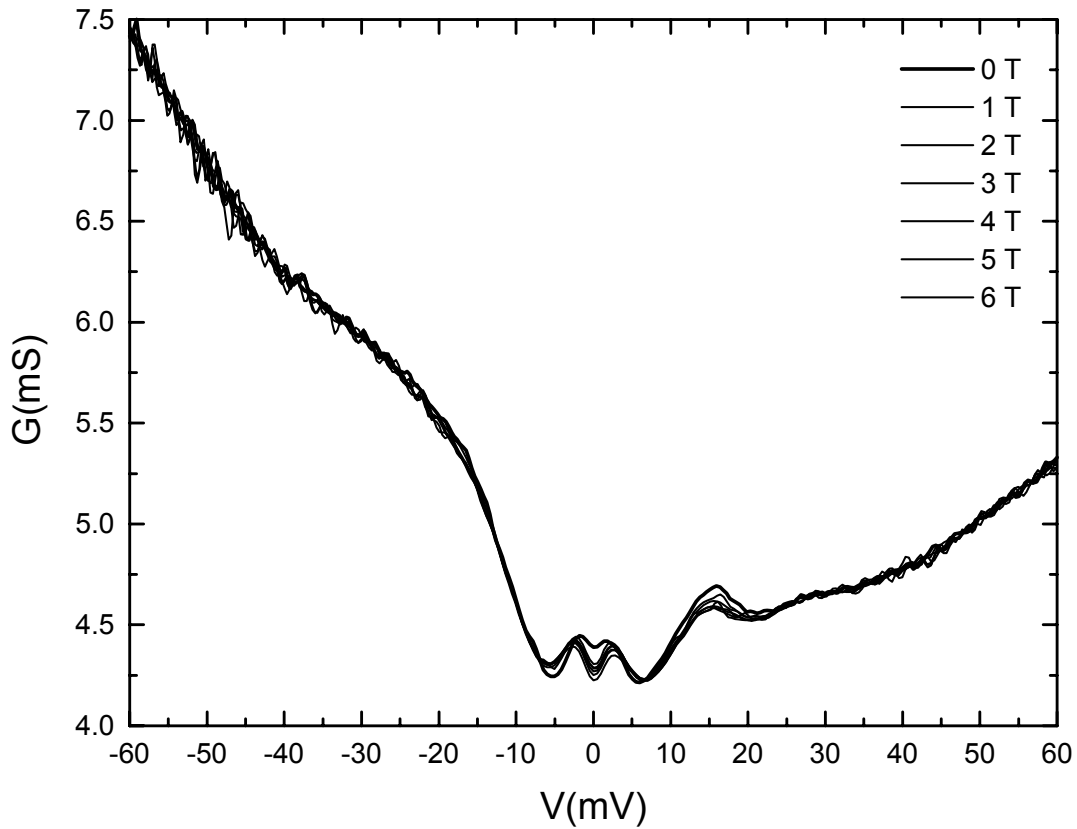


Fig 60: Magnetic field dependence of the conductance spectra of an optimally doped (100)-YBCO/In junction taken at $T=4.2K$. $H \perp a$ and increasing.

In Fig 61b the field evolution is shown for H parallel to the b -axis ($H \parallel b$). In that configuration the ZBC decreases and δ increases with increasing H , but with weaker field dependence.

The field dependence for H parallel to the a -axis ($H \parallel a$) is qualitatively the same as for $H \parallel b$. When reducing H , the ZBC increases and δ is reduced, however hysteretically if $H \parallel c$. No hysteresis is observed for $H \parallel b$ and $H \parallel a$.

The detailed field dependence of δ can be followed in Fig 62. It will be described first the case $H \parallel c$, symbolized by full circles.

For H increasing from 0 to 6T, one can distinguish three regions:

- a) for $\mu_0 H \leq 0.1T$, the peak position is field independent within the experimental error and $\delta = \delta_s$.
- b) for $0.1T < \mu_0 H < 0.8T$, δ is strongly field dependent and increases with a slope of $1.3mV/T$.
- c) for $\mu_0 H \geq 0.8T$, δ is weakly field dependent and increases at a rate of $0.1mV/T$.

For $\mu_0 H$ decreasing from 6T to 0T, roughly two regions can be distinguished:

- d) for $5.5T < \mu_0 H \leq 6$, δ is strongly field dependent and decreases with an initial slope of $1.1mV/T$.

e) for $\mu_0 H \leq 5.5\text{T}$, δ is weakly field dependent and changes with a slope of 0.14mV/T .

In the case $H||b$, symbolized by open squares, the hysteresis is absent and δ is weakly field dependent with a slope of 0.09mV/T over the entire field range. The slope for the case $H||a$ is 0.11mV/T .

In order to get more information about the hysteretic behavior in the case $H||c$, the magnetic field was cycled between different starting and end-points. First a field of 6T was applied, which was then reduced to 3T . Then the field dependence was measured between 3T and 5T as depicted in Fig 62 by open circles. Again strong field dependence shows up with an initial slope of 1.4mV/T , which flattens above 3.5T to 0.12mV/T . Finally the field was swept between 5T and 4.8T . The field dependence in that range is strong, with a slope of 1.9mV/T and not hysteretic.

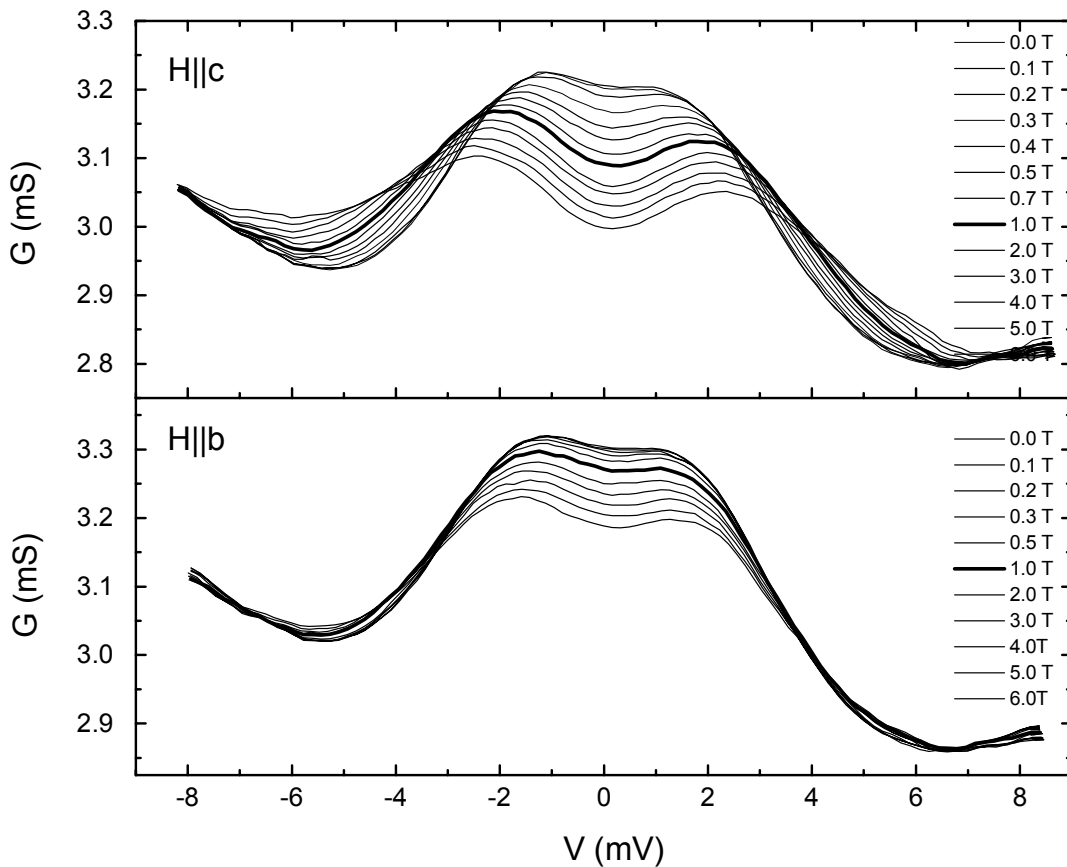


Fig 61: Anisotropic magnetic field dependence of the conductance spectra of an optimally doped (100)-in-plane oriented YBCO/In junction taken at $T=4.2\text{K}$. a) $H||c$. b) $H||b$. H increasing.

The field dependence can be summarized as follows. In the case $H||c$, there exist two distinct regimes of field sensitivity, which are characterized by a strong and a weak field dependence of the ZBCP splitting, with slopes of $\sim 1.3\text{mV/T}$ and $\sim 0.1\text{mV/T}$ respectively. If the magnetic field variation is small, $\Delta H < \Delta H^*$, the field dependence is strong and the ZBCP

splitting is reversible and non-hysteretic. If $\Delta H > \Delta H^*$, the splitting follows successively two slopes, and is hysteretic. In the case $H \parallel c$ and $H \parallel a$, the field dependence is non-hysteretic and weak with slopes of $\sim 0.09 \text{ mV/T}$ and $\sim 0.11 \text{ mV/T}$ respectively.

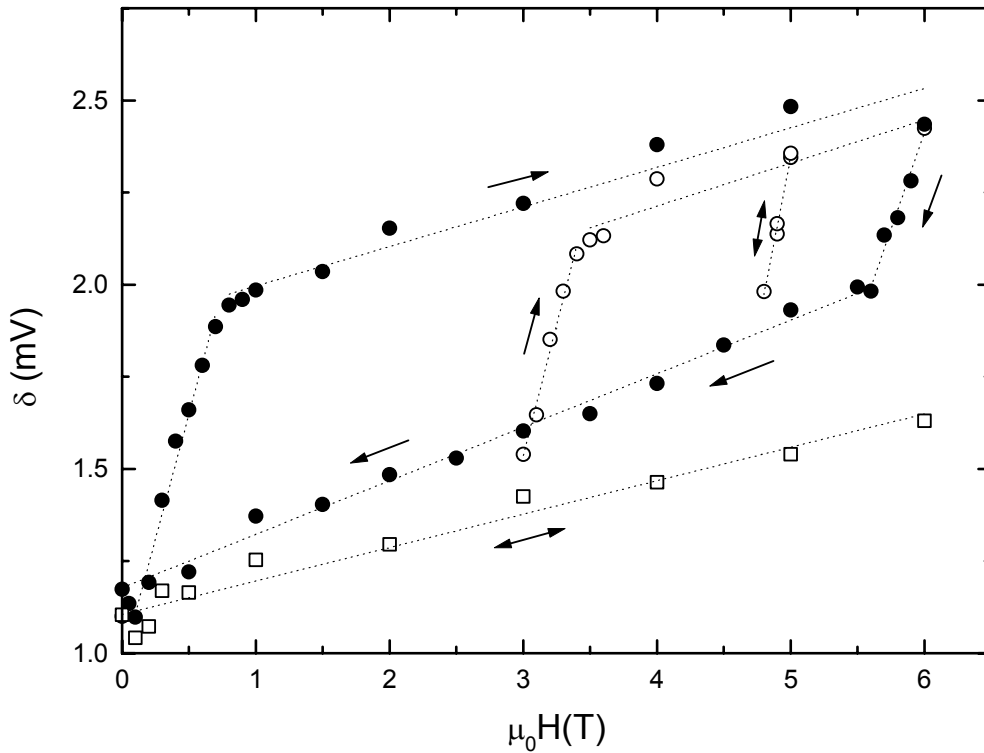


Fig 62: Peak position δ vs. magnetic field. $H \parallel c$ (●,○) and $H \parallel b$ (□). The arrows indicate the sweep direction of the magnetic field as explained in the text. Dotted lines are guides to the eye.

Now the focus is on the high bias peak at 17mV (Fig 60 and Fig 72). The peak intensity is strongly reduced by a magnetic field of 1T. At higher fields the intensity diminishes further but weaker. Within the experimental uncertainty no shift in energy of the peak is observed.

It has to be added that only one junction showed no zero-field splitting at $T=4.2\text{K}$. Nevertheless a large field splitting was observed (Fig 63)

The anisotropic magnetic field dependence of the ZBCP on in-plane oriented [100] $\text{Y}_1\text{Ba}_2\text{Cu}_3\text{O}_{7-x}/\text{In}$ tunnel junctions presented in this chapter has been published in [74].

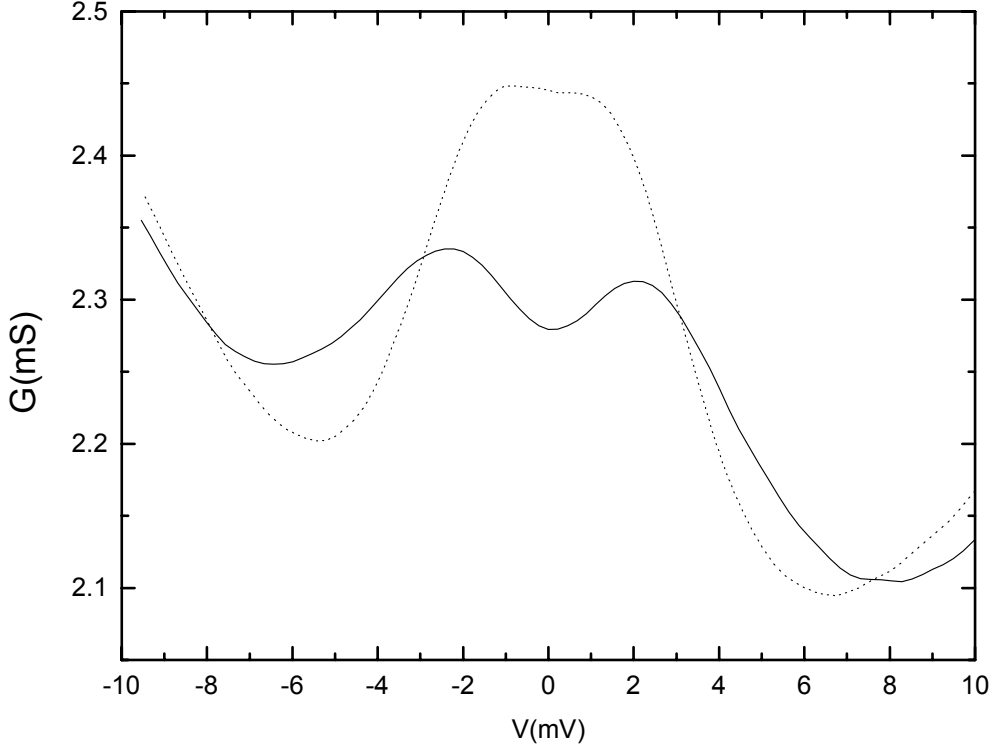


Fig 63: Large field splitting of the ZBCP on a sample without zero-field splitting. Note that the peak is broadened in zero-field. $\{H\|c, T=4.2K, (\cdots) \mu_0H=0T, (—) \mu_0H=6T\}$.

7.2.2 Underdoped YBCO

The magnetic field dependence of the conductance spectra for oxygen underdoped YBCO taken at $T = 4.2K$ are shown in Fig 64 and Fig 65 for the two field orientation $H\|c$ and $H\|b$ respectively.

The sensitivity of the conductance spectra to the magnetic field is limited to a small bias range $V \leq 4mV$. No significant anisotropy of the field effect is observed, yet the suppression of the ZBCP is somewhat larger at $H\|c$. In both orientations, the ZBCP is completely suppressed at $\mu_0H = 6T$. At low fields $\mu_0H \leq 3T$ the ZBCP can be well fitted to a lorentzian distribution with a field independent width $\Gamma \approx 4mV$ in both field orientations (Fig 66), where

$$G(V) = G(0) + \frac{A}{\pi} \cdot \frac{\Gamma/2}{(\Gamma/2)^2 + (V - V_0)^2}, \quad G(0), A, V_0 \text{ are constants.}$$

For higher fields $\mu_0H > 2T$ fitting to a simple lorentzian distribution is not possible due to splitting of the ZBCP. At $\mu_0H = 6T$ a field splitting of $\delta \approx 1.2mV$ is observed in both field orientations $H\|c$ and $H\|b$.

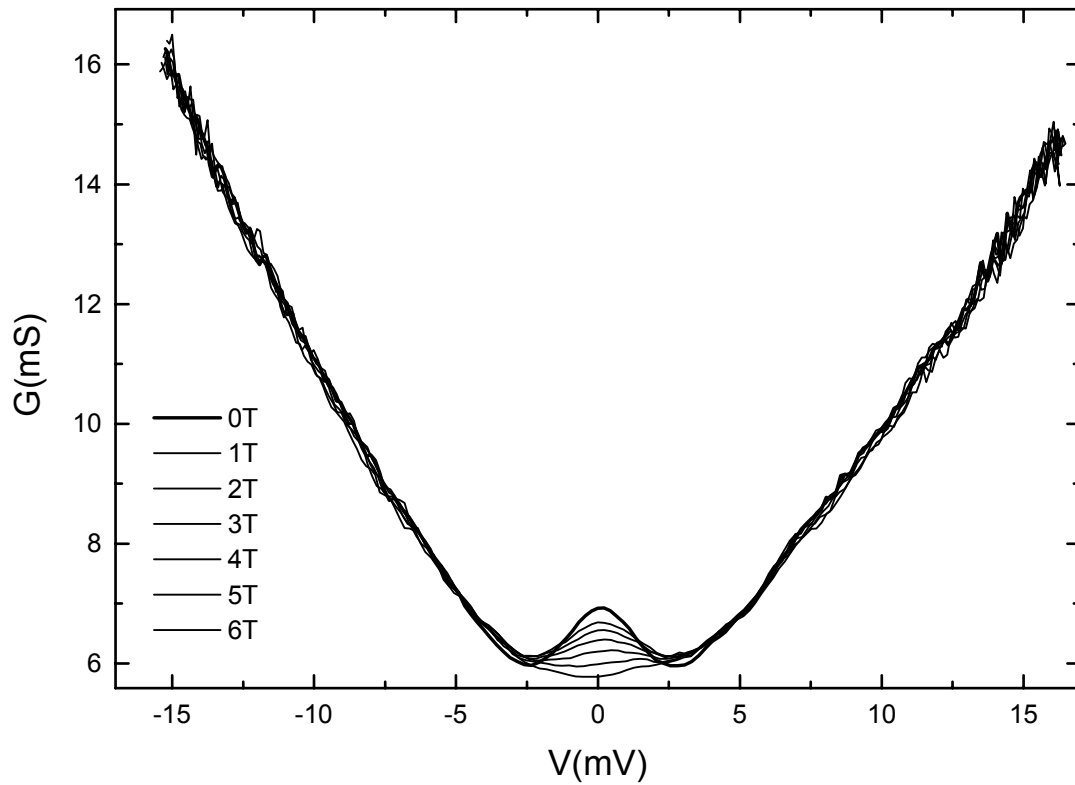


Fig 64: Magnetic field dependence of the conductance spectra of oxygen an underdoped (100)-in-plane oriented YBCO/In junction taken at $T=4.2K$. $H||c$ and increasing.

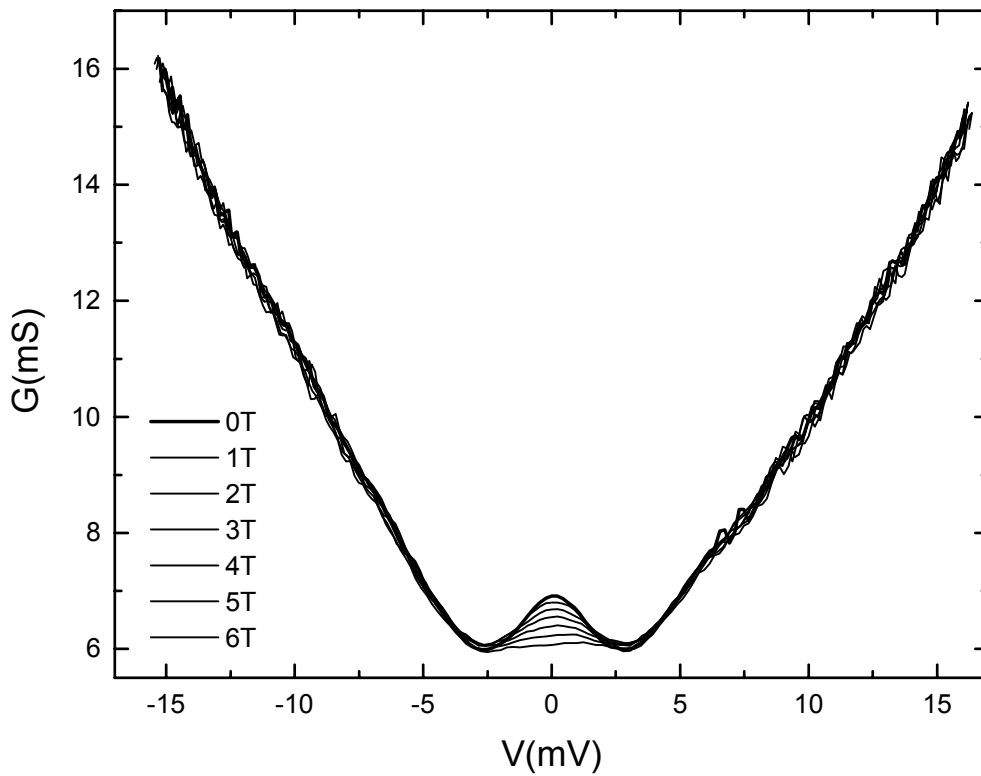


Fig 65: Magnetic field dependence of the conductance spectra of an oxygen underdoped (100)-in-plane oriented YBCO/In junction taken at $T=4.2K$. $H||b$ and increasing.

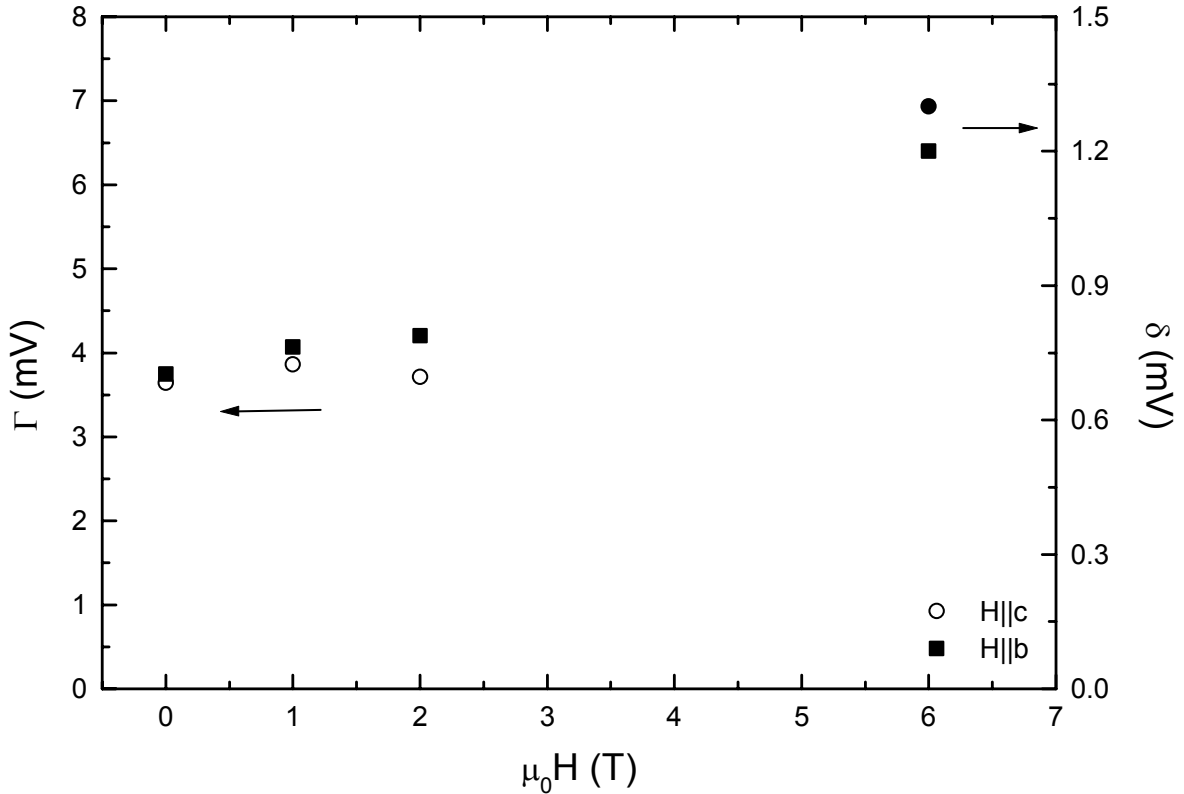


Fig 66: Width Γ of the Lorentzian distribution fit on the ZBCP as a function of magnetic field for $\mu_0 H \leq 2T$, and splitting δ of the ZBCP at $\mu_0 H = 6T$, for $H||c$ (O) and $H||b$ (■). The arrow indicates the relevant axis.

7.2.3 Overdoped Ca-YBCO

The magnetic field dependence of the conductance spectrum for overdoped Ca-YBCO has been measured for both field orientations $H||c$ and $H||b$ at $T = 4.2K$. The sensitivity of the spectrum to magnetic field extends over the entire measured bias range up to $V = 25mV$ for the field orientation $H||c$ (Fig 67). Two regions can be identified where the change due to the magnetic field is large. In the high bias region between $8mV$ and $22mV$ the conductivity is suppressed at large magnetic fields. In the low bias region, $V < 8mV$, a large shift in spectral weight from the zero-bias region towards higher energies is observed (Fig 68).

In the field orientation $H||b$ the field sensitivity is different. At high bias a similar reduction of the conductivity is observed as in the case of $H||c$, however the sensitive bias range is now between $6mV$ and $16mV$ (Fig 69). The low bias region $V < 6mV$ is only weakly field dependent and shows a small shift in spectral weight from the zero-bias region towards higher energies (Fig 70).

Therefore the field dependence is anisotropic also for overdoped Ca-YBCO.

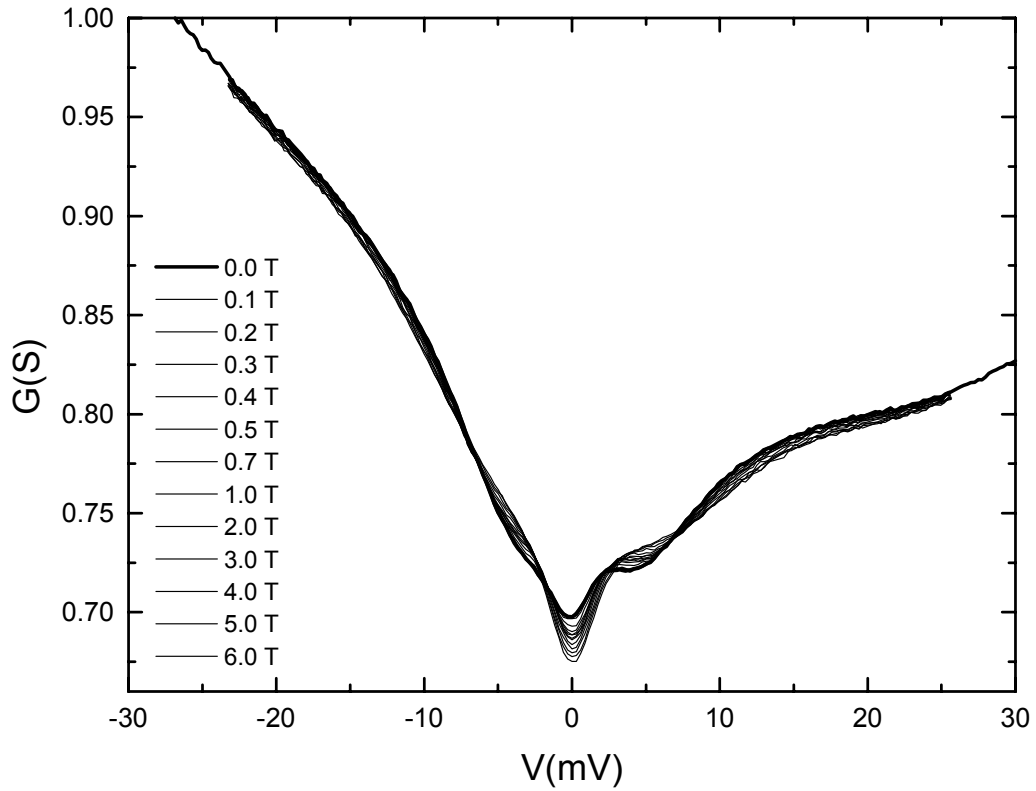


Fig 67: Magnetic field dependence of the conductance spectra of an overdoped (100)-in-plane oriented CaYBCO/In junction taken $T=4.2K$, $H||c$ and increasing.

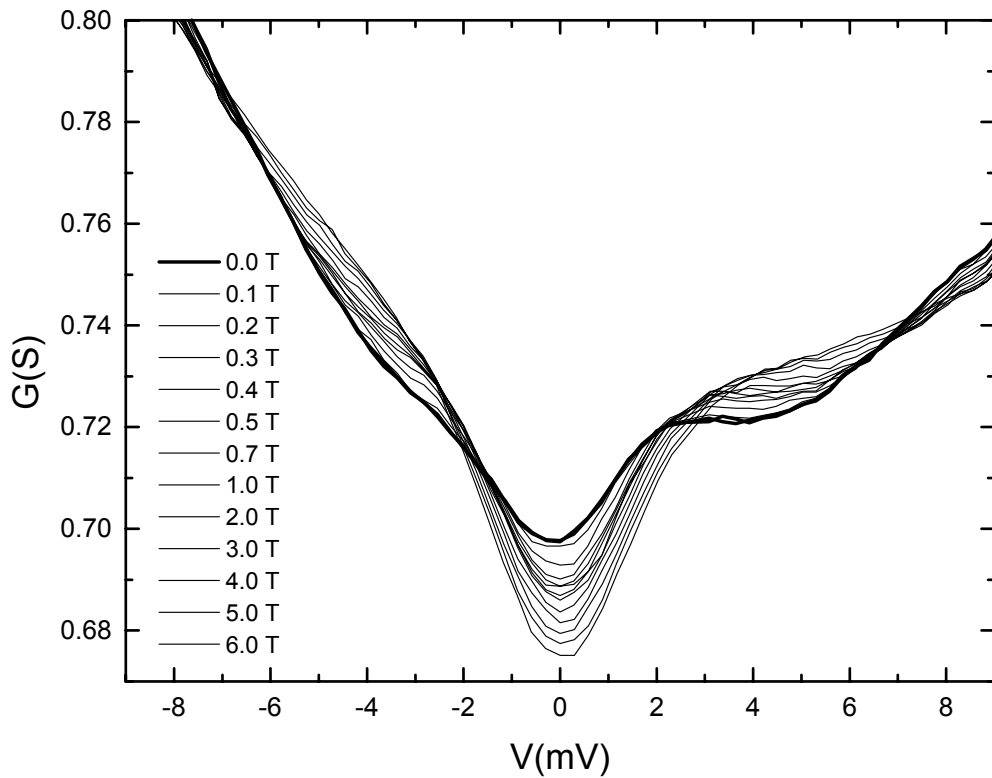


Fig 68: Magnetic field dependence of the sub-gap of an overdoped (100)-in-plane oriented CaYBCO/In junction taken at $T=4.2K$. $H||c$ and increasing.

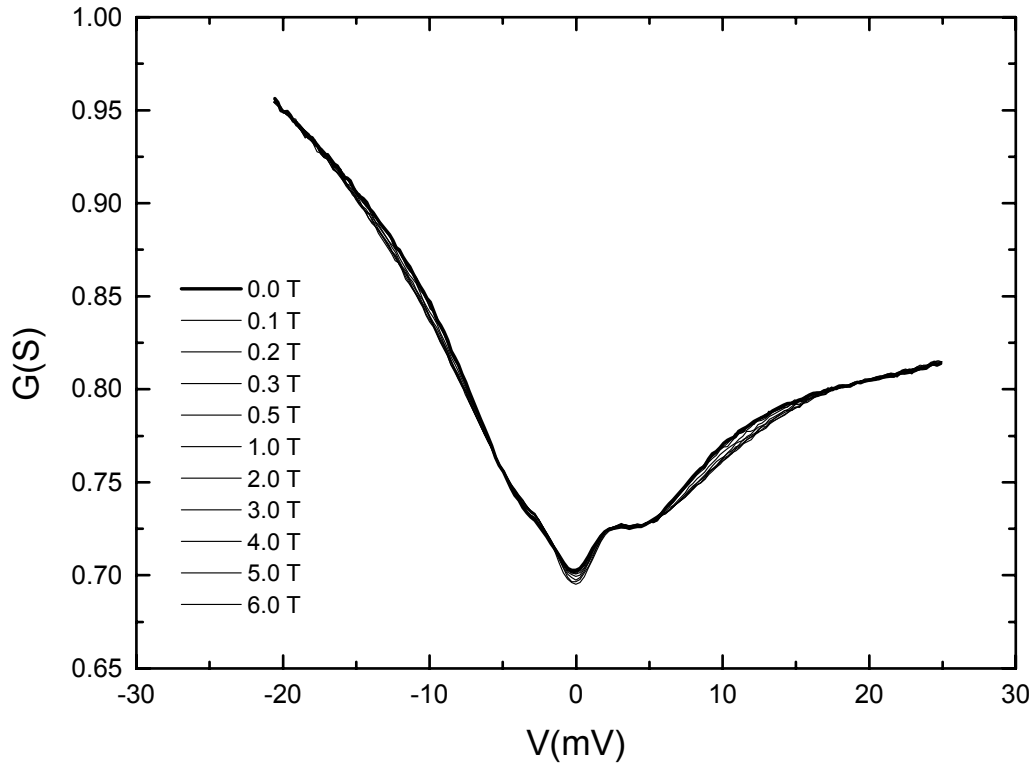


Fig 69: Magnetic field dependence of the conductance spectra of an overdoped (100)-in-plane oriented CaYBCO/In junction taken $T=4.2K$, $H||b$ and increasing.

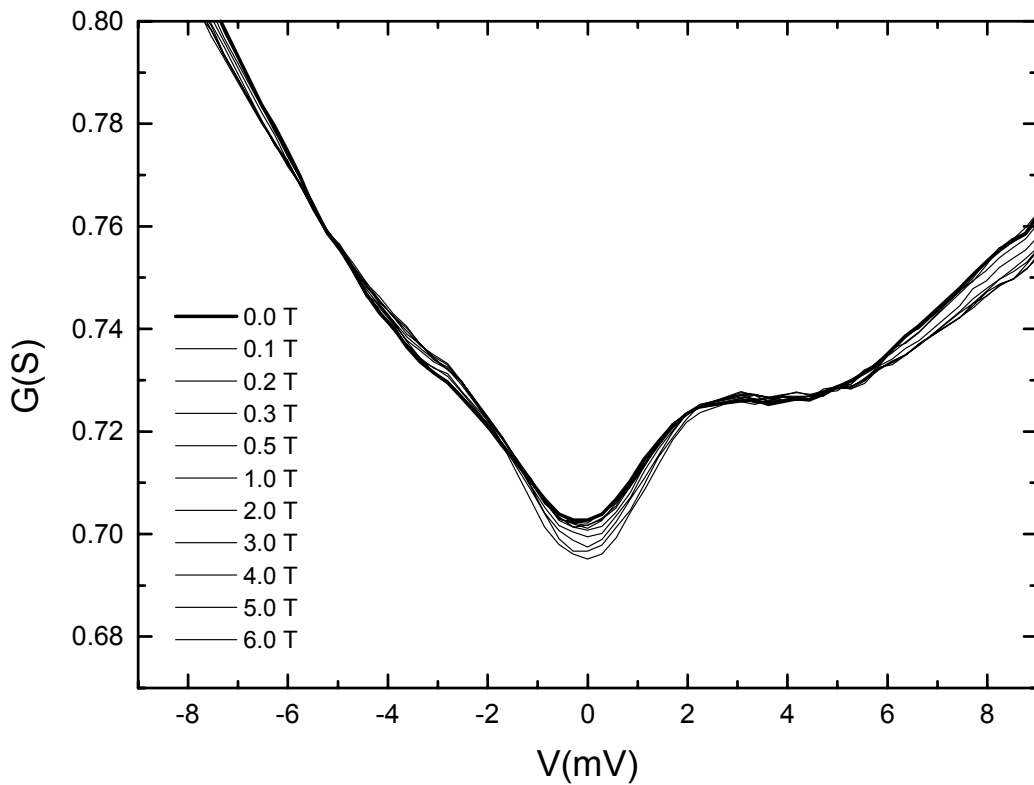


Fig 70: Magnetic field dependence of the sub-gap of an overdoped (100)-in-plane oriented CaYBCO/In junction taken at $T=4.2K$. $H||b$ and increasing.

In the case of optimally doped samples, the shift of spectral weight as a function of

magnetic field could be easily followed, by measuring the peak position of the splitted ZBCP. In the overdoped samples this is not possible due to the absence of a ZBCP. Instead the subgap δ has been identified as the onset of the conductance reduction in the low bias region.

The widening of the subgap δ with magnetic field is shown in Fig 71. A striking similarity to the field splitting of the ZBCP in optimally doped samples is present.

For $H||c$ a large field induced widening of the subgap is observed for $\mu_0 H < 0.8T$ with a slope of $1.2mV/T$. At larger fields the field induced widening is weaker with a slope of $\approx 0.2mV/T$.

The field dependence is hysteretic. Upon field reduction the subgap narrows strongly between $6T$ and $5.5T$ with a slope of $\approx 1mV/T$. Between $5.5T$ and $0T$ the subgap narrows weakly with a slope of $\approx 0.3mV/T$.

For $H||b$ the field induced widening of the subgap is not hysteretic and weak with an estimated slope of $\approx 0.2mV/T$.

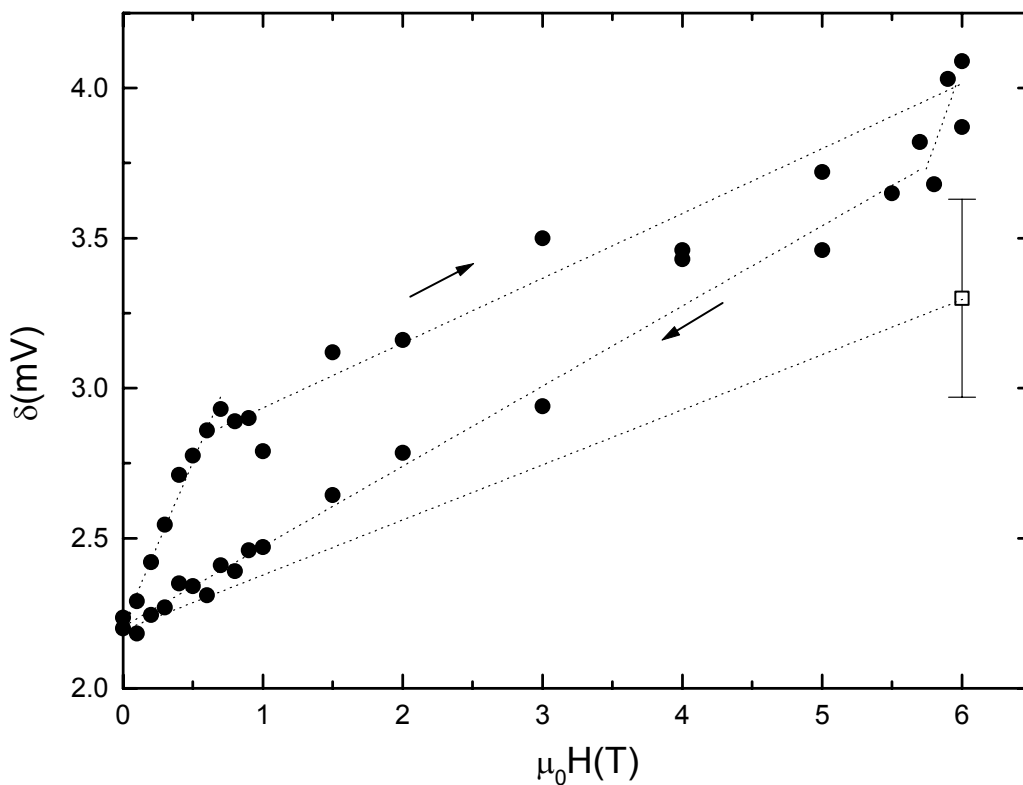


Fig 71: Sub-gap δ vs. magnetic field. $H||c$ (\bullet) and $H||b$ (\circ). The arrows indicate the sweep direction of the magnetic field. Dotted lines are guides to the eye.

7.3 Temperature Dependence of the Crossover Field H^*

An important question for the discussion of the field splitting is whether the crossover field H^* is temperature dependent. In order to guaranty long term stability of the temperature the lengthy measurements had to be restricted to two temperatures, $4.2K$ and $1.47K$.

The measurements were performed with an Indium contact on an optimally doped (100) oriented YBCO sample with considerably smaller degree of in-plane orientation. Smaller degrees of in-plane orientation are sometimes observed in these samples, however the origin remains unclear. In this sample also the junction conductance is significantly larger and very similar to junctions obtained with Ag contacts. The zero-field splitting at $T = 4.2\text{K}$ is weaker than usually observed, with $\delta \approx 0.9\text{-}1.0\text{mV}$ (Fig 72). Nevertheless a clear non-linear field splitting is observed at both field orientations $H\parallel[010]\text{LSGO}$ and $H\parallel[001]\text{LSGO}$ (Fig 73).

At $T = 4.2\text{ K}$, with $H\parallel[001]\text{LSGO}$, at least two crossover fields are observed at $\mu_0H = 0.5\text{T}$ and $\mu_0H = 1\text{T}$ respectively. At $H\parallel[010]\text{LSGO}$ one crossover field is observed at $\mu_0H = 0.5\text{T}$. The low field slope ($\mu_0H \leq 0.5\text{T}$) is 0.78mV/T and 0.43mV/T for the two field orientations $H\parallel[001]\text{LSGO}$ and $H\parallel[010]$ respectively.

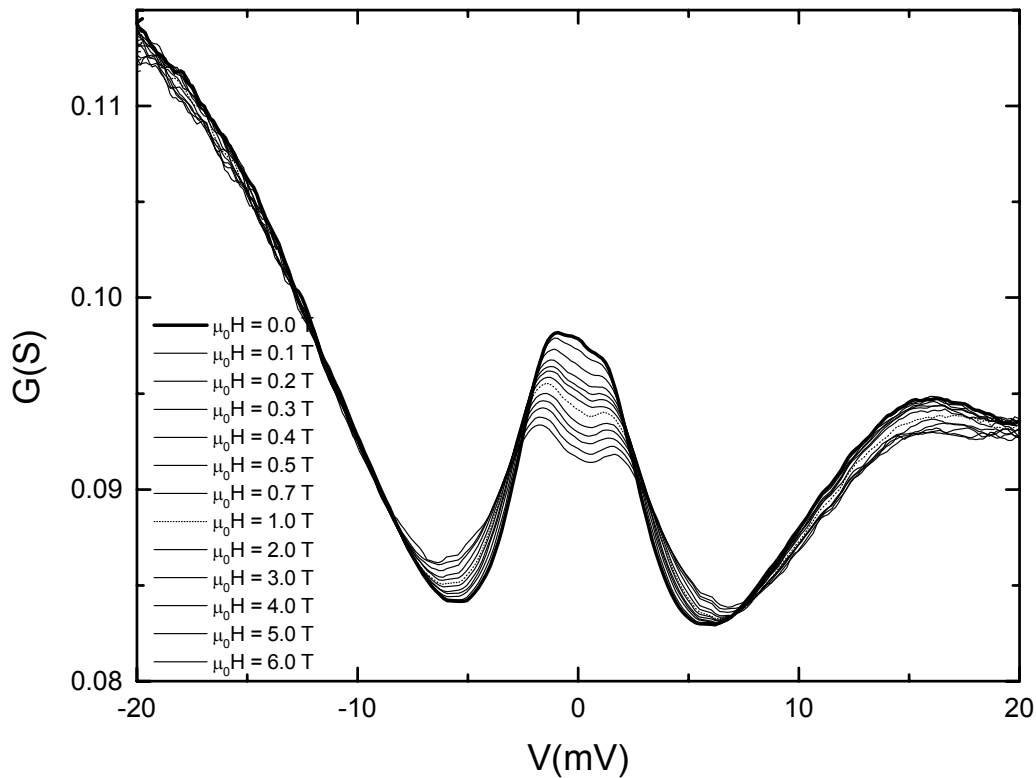


Fig 72: Magnetic field dependence of the conductance spectra of an optimally doped (100)-YBCO/In junction taken $T=4.2\text{K}$. $H\parallel[001]\text{LSGO}$ and increasing

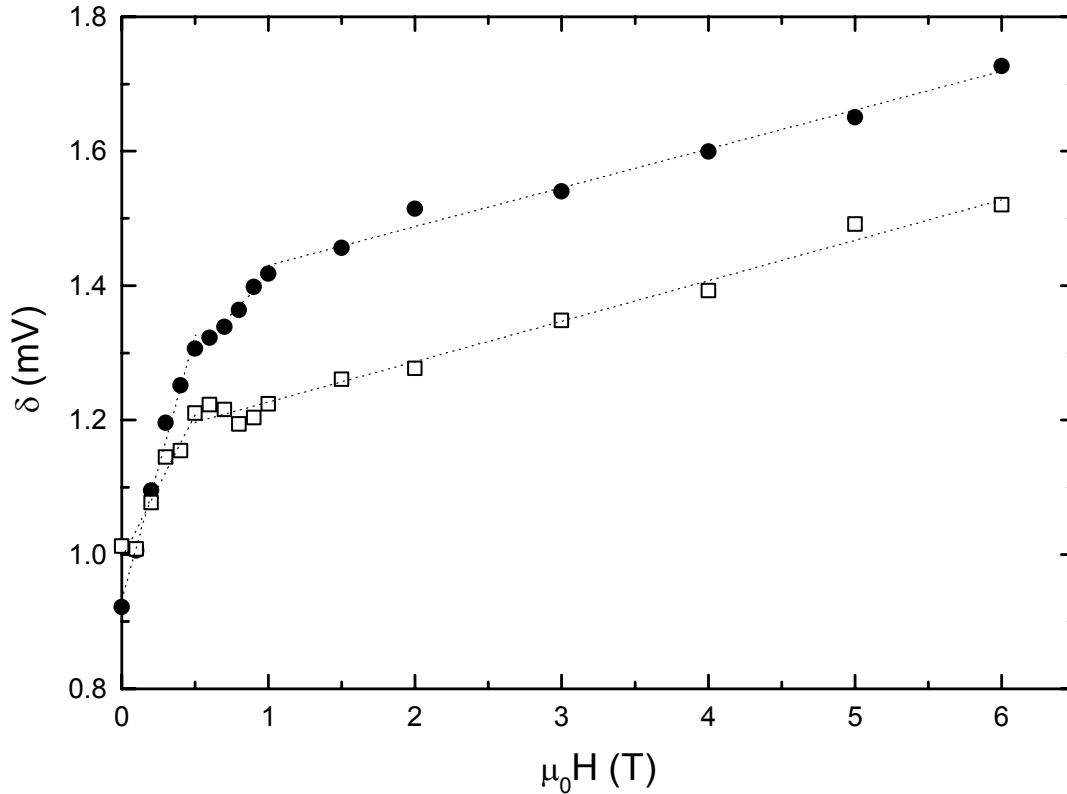


Fig 73: Peak position δ vs. magnetic field. $H||[001]LSGO$ (●) and $H||[010]LSGO$ (□). Dotted lines are guides to the eye.

At high fields ($\mu_0 H \geq 1T$) the slope is for both orientations $0.06mV/T$. In the intermediate field range $0.5T \leq \mu_0 H \leq 1T$ the slope is $0.23mV/T$ for $H||[001]LSGO$.

At $T = 1.47K$, the measurement was for technical reasons restricted to a maximum field of $\mu_0 H = 1T$. The zero-field spectrum is considerably altered due to the superconducting Indium electrode (Fig 74). The specific shape of the zero-field spectrum is analysed later. Above $\mu_0 H \geq 0.03T$ Indium is normal conducting.

The extrapolated zero-field splitting (Fig 75) at $T = 1.47K$ is $\delta = 1.2mV$ and therefore larger than at $T = 4.2K$. The crossover field is for both orientations reduced to $\mu_0 H = 0.3T$. The low field slopes ($\mu_0 H \leq 0.3T$) are reduced to $0.6mV/T$ and $0.36mV/T$ for the two orientations $H||[001]LSGO$ and $H||[010]LSGO$ respectively, as well as the intermediate range slope of $0.14mV/T$ in the case $H||[001]LSGO$ for $0.5T \leq \mu_0 H \leq 1T$.

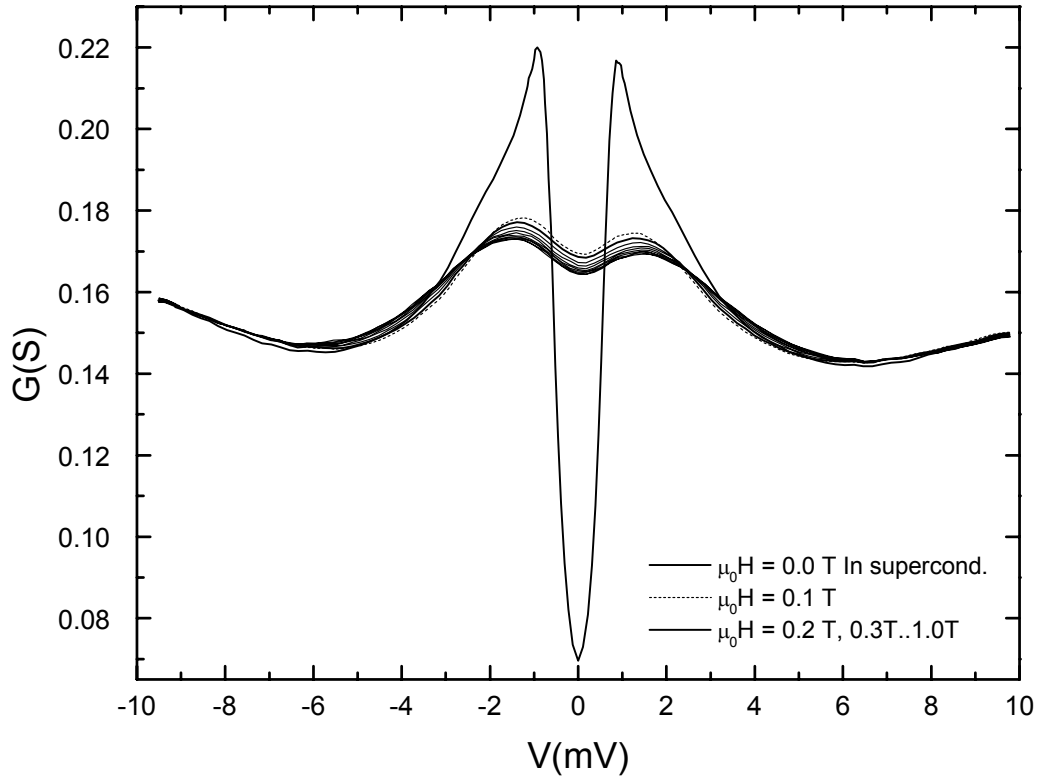


Fig 74: Magnetic field dependence of the conductance spectra of an optimally doped (100)-oriented YBCO/In junction taken at $T = 1.47\text{K}$. $H \parallel [001]\text{LSGO}$ and increasing.

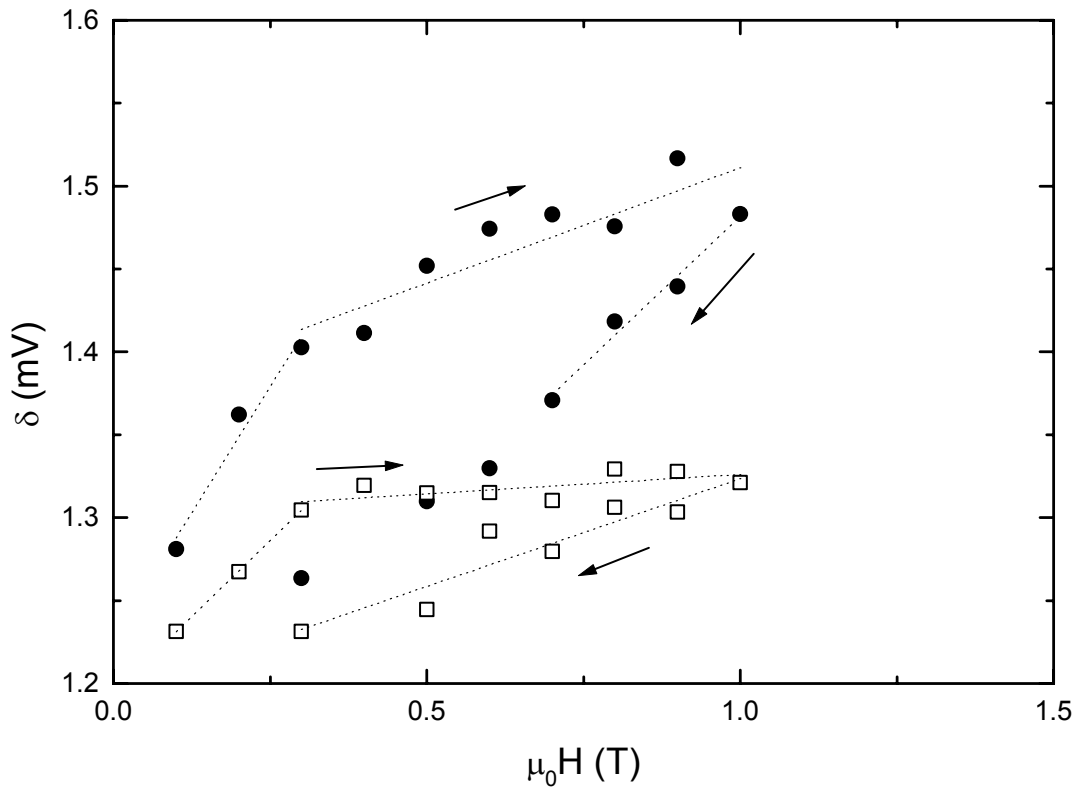


Fig 75: Peak position δ vs. magnetic field. $H \parallel [001]\text{LSGO}$ (●) and $H \parallel [010]\text{LSGO}$ (□). Dotted lines are guides to the eye. Arrow indicate the sweep direction of the magnetic field.

7.4 Conductance Spectra with Ag Contacts on Optimally Doped YBCO

Conductance spectra of Ag contacts on optimally doped (100) in-plane oriented YBCO films were measured as a function of temperature at zero magnetic field (Fig 76) and of magnetic field at $T=4.2\text{K}$ (Fig 77). The spectra are significantly different from those obtained with Indium contact. The conductance is about three orders of magnitude larger and only a weak asymmetric background is observed. The high-energy part of the spectrum at low temperature as well as the whole spectrum at temperatures close to T_c can not be fitted to a parabolic background, which gives doubt about elastic tunneling being the dominant process. Furthermore all features seem to be broadened even at $T = 4.2\text{K}$. No splitting of the ZBCP is observed down to $T = 4.2\text{K}$. Generally no sharp peak in the conductance is observed at $V=17\text{mV}$. Instead a broad peak at $V=20..40\text{mV}$ is present with the energy range varying from sample to sample. This feature is also weakly observed in some junctions with Indium contacts (Fig 60). The broad peak seems not to move in energy at higher temperature and can be detected up to T_c . The ZBCP does vanish at about $T = 40\text{K}$. A magnetic field modifies the spectra up to $30..40\text{mV}$ similar to spectra with Indium contacts (Fig 77).

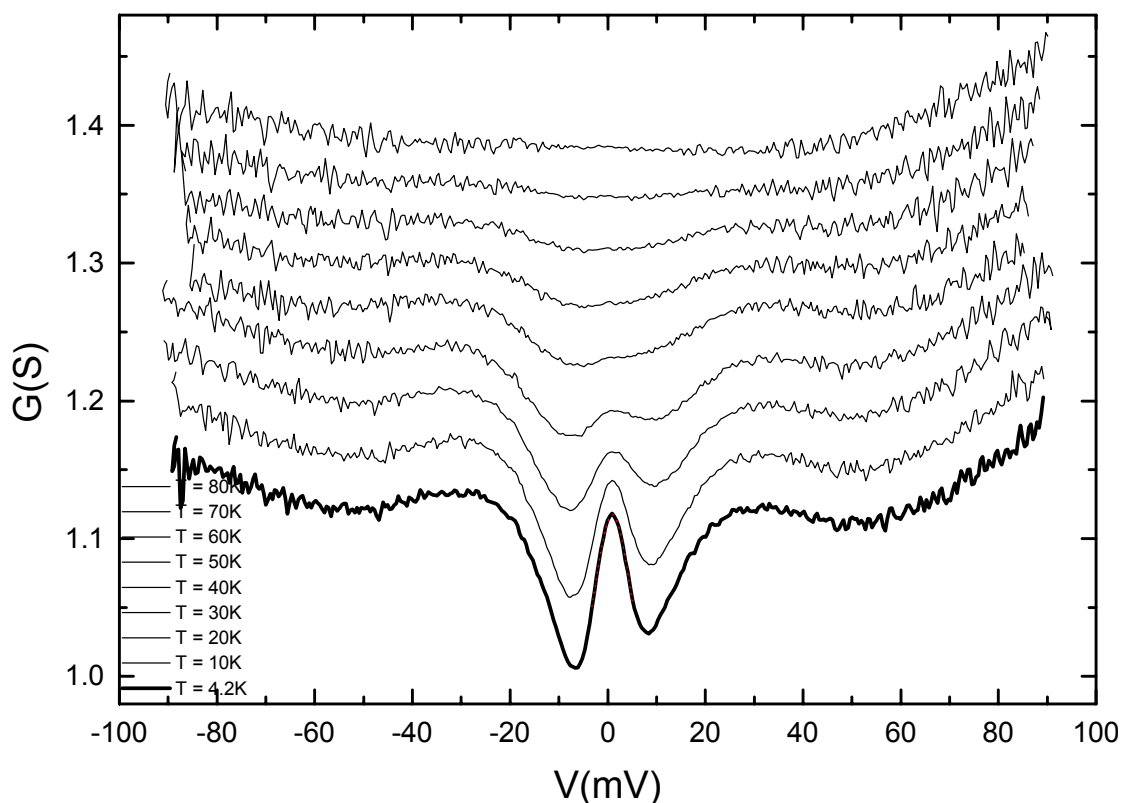


Fig 76: Temperature dependence of conductance spectra of a YBCO/Ag contact at zero magnetic field.

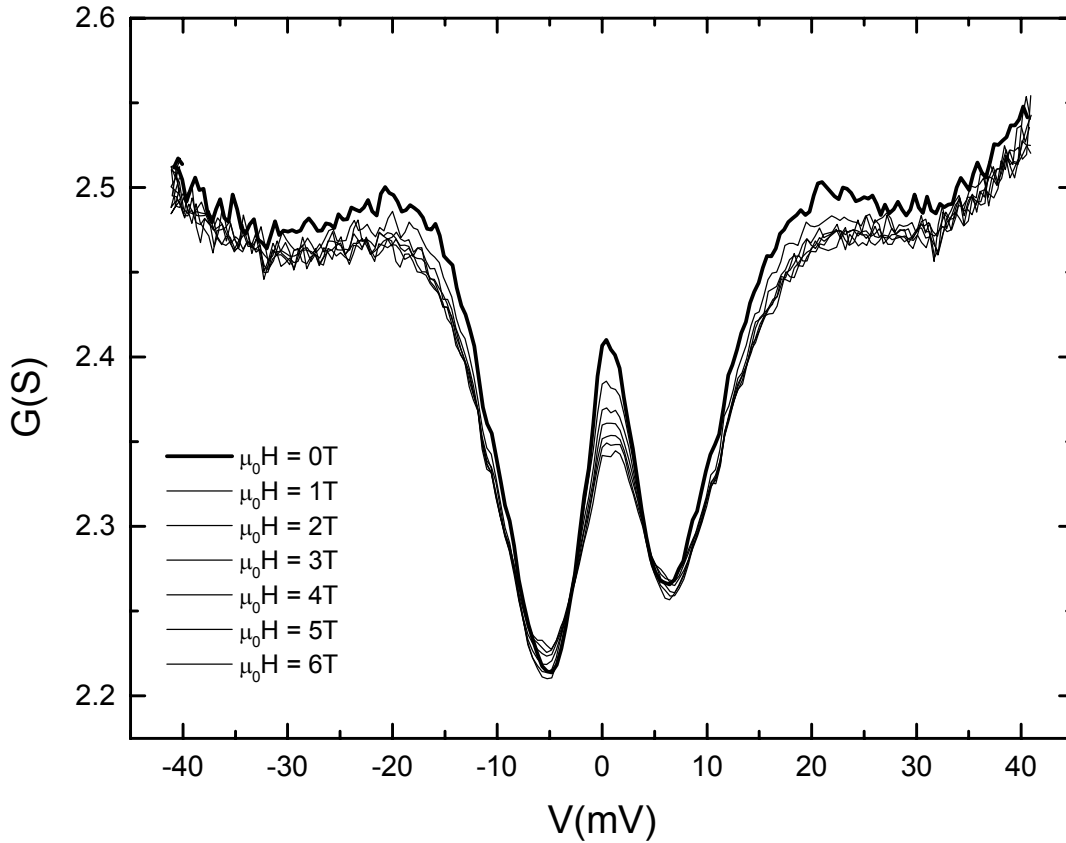


Fig 77: Magnetic field dependence of conductance spectra of a YBCO/Ag contact at $T=4.2K$.

As seen in Fig 77 the high energy peak between $V=15..30mV$ is significantly reduced by a magnetic field of 1T and less sensitive to higher fields. The intensity of the ZBCP is also reduced, which is depicted in detail for the two field orientations $H||c$ and $H||b$ in Fig 78 and Fig 79, respectively.

Although no splitting is observed the ZBC shows a field dependence similar to the splitting. The relative reduction of the ZBC and the broadening of the ZBCP are the strongest for the field orientation $H||c$ and for low fields $\mu_0H \leq 2T$. At larger fields the sensitivity is weaker. A hysteresis is observed upon field reduction. The magnetic field dependence is similar for the orientation $H||b$, however the low field reduction of the ZBC is weaker (Fig 81). It has to be mentioned that the field alignment in this measurement was not very accurate.

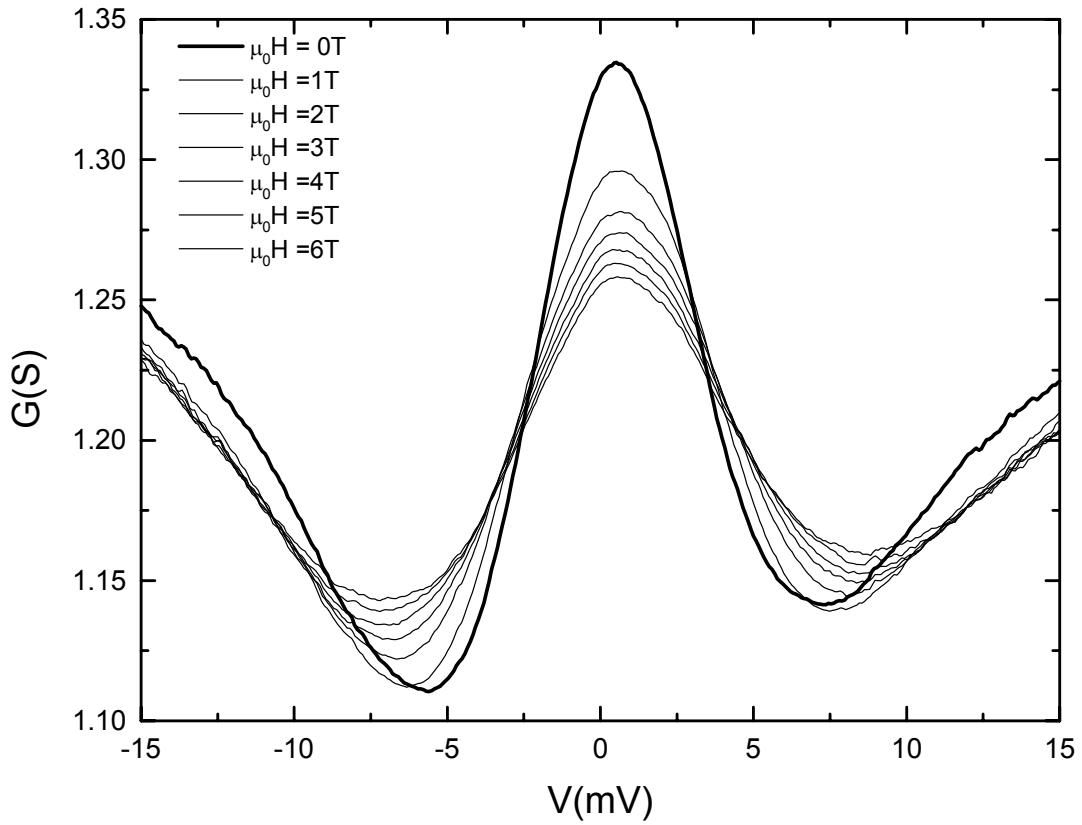


Fig 78: Magnetic field dependence of the ZBCP of a YBCO/Ag contact at $T=4.2K$. $H||c$ and increasing.

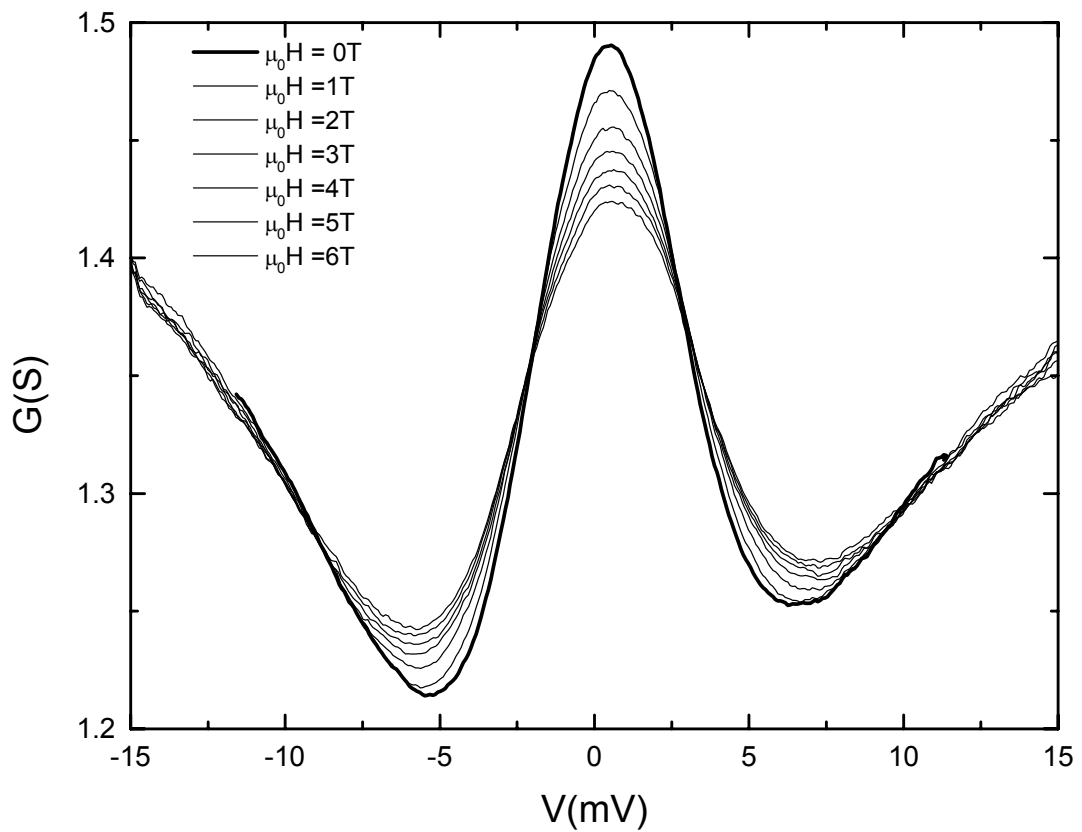


Fig 79: Magnetic field dependence of the ZBCP of a YBCO/Ag contact at $T=4.2K$. $H||b$ and increasing.

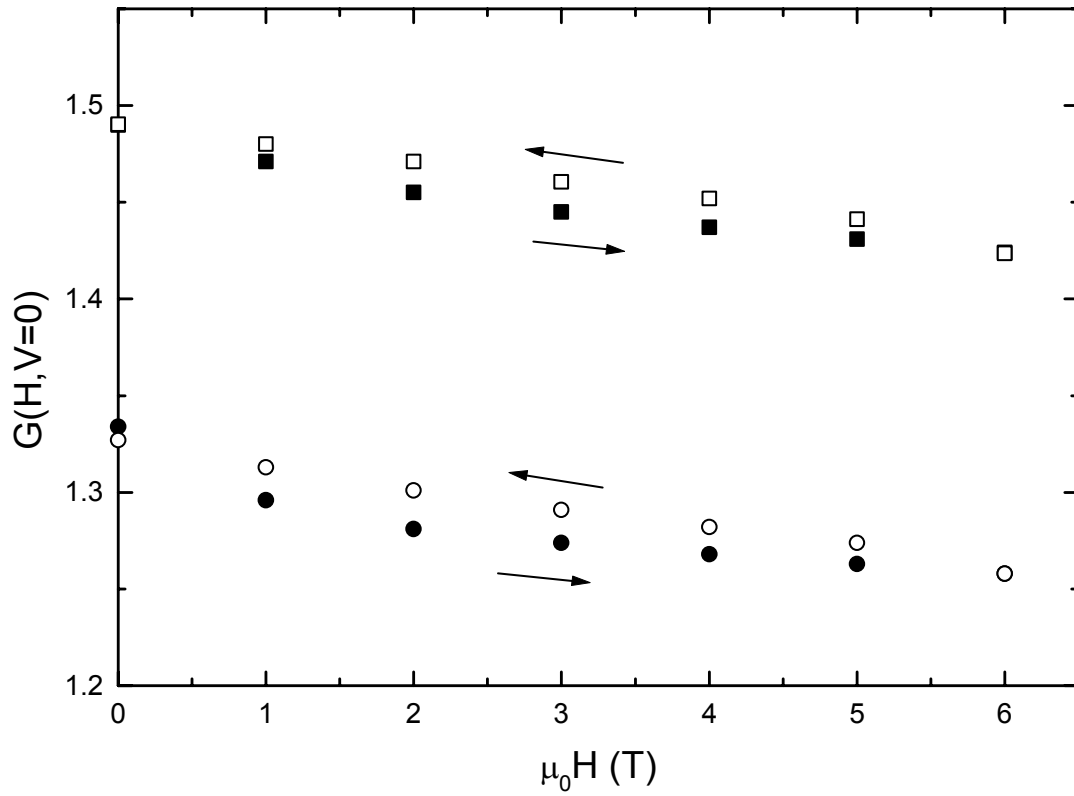


Fig 80: Field dependence of the zero-bias conductance of a YBCO/Ag contact at $T=4.2K$. $H||c$ (\bullet, \circ) and $H||b$ (\blacksquare, \square). Arrows indicate the sweep direction of the magnetic field.

8 Discussion

In this chapter the conductance spectra will be discussed. The main focus will be on the temperature and the magnetic field dependence of the zero-bias anomaly measured on optimally doped YBCO. The data will be used to test existing theories. The discussion will then be expanded by the doping dependence of the conductance spectra.

8.1 Evidence for Elastic Tunneling in In/YBCO Junctions

For the following discussion it is important to show, that elastic tunneling contributes the most to the voltage dependent part of the conductance spectrum of an In/YBCO contact. In that case the conductance spectrum can be calculated with:

$$G(V) = \frac{dI}{dV}, \quad I(V, T) \propto \int_{-\infty}^{\infty} N_{\text{In}}(E, T) \cdot N_{\text{YBCO}}(E - eV, T) \frac{d[f(E - eV, T) - f(E)]}{dE} dE,$$

where N_{In} is the density of states of Indium at finite temperature, N_{YBCO} is the density of states of YBCO at finite temperature and f is the Fermi function. N_{In} at finite temperature can be calculated, since the material is a conventional BCS-superconductor. N_{YBCO} can not be calculated, since its temperature dependence is not known. However, when superconductivity in Indium is suppressed by a small magnetic field (Fig 81, $\mu_0 H = 0.05\text{T}$) and therefore $N_{\text{In}} = \text{const.}$, the measured conductance at low temperature is approximately N_{YBCO} , yet thermally smeared.

The equation above is therefore approximated by the zero temperature integral using the thermally smeared density of states of In (calculated) and YBCO (measured), \bar{N}_{In} and \bar{N}_{YBCO} , respectively:

$$I(V) \propto \int_0^{eV} \bar{N}_{\text{In}}(E) \cdot \bar{N}_{\text{YBCO}}(E - eV) dE$$

Since the temperature of the measurement is known, here $T = 1.47\text{K}$, there are no fitting parameters except for a voltage independent part of the conductance due to pin holes in the tunneling barrier, G_{Ohmic} . With an assumed leakage current of 36%, the SIS spectrum could be well fitted (Fig 81). Especially the ‘bump’ at 2mV is very well reproduced, which is

convincing evidence, that most of the conductance features are due to elastic tunneling. The remaining discrepancy is probably due to the inequivalence of the two integrals. It should be stressed that the BCS density of states of Indium could not be recovered by simply subtracting or dividing the spectrum taken at $\mu_0 H = 0 T$ by the one taken at $\mu_0 H = 0.05 T$, which is consistent with the absence of inelastic scattering.

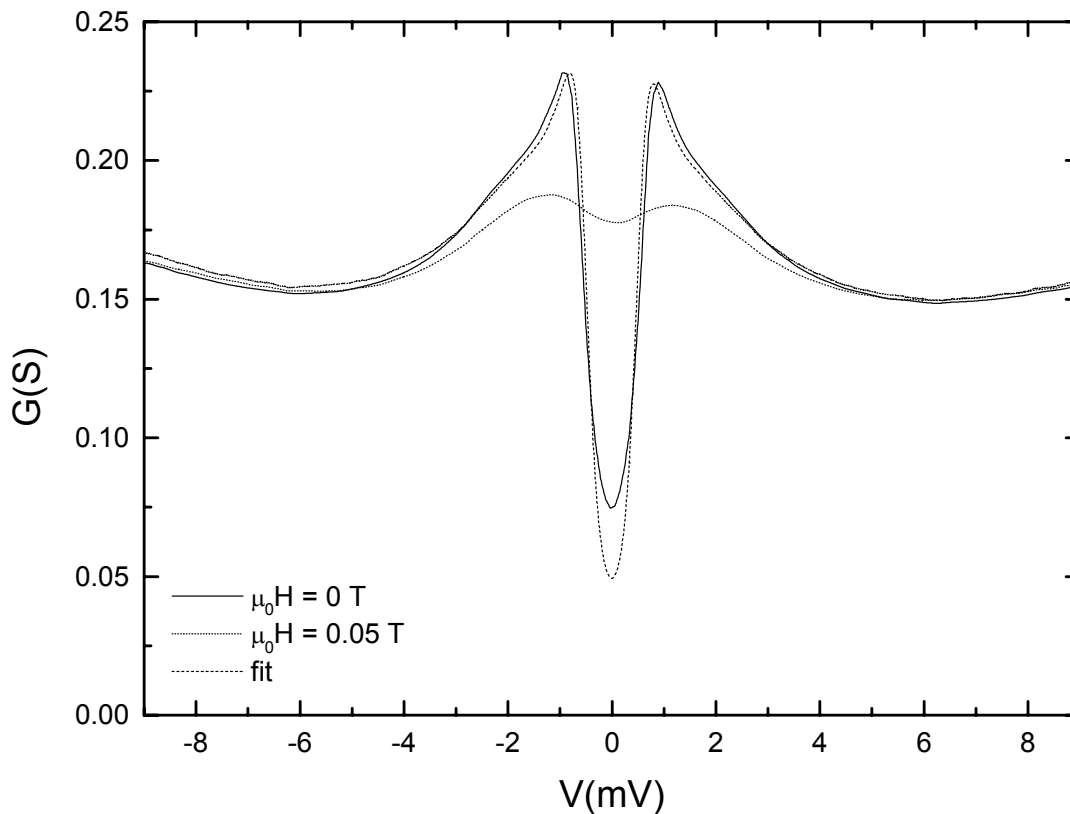


Fig 81: Fitting of the conductance spectra of an optimally doped (100)-oriented YBCO/In junction in the low bias range, $T = 1.47 K$. The fitting uses the calculated BCS density of states of Indium and the YBCO density of states measured at $\mu_0 H = 0.05 T$ (see text). $G_{ohmic} = 0.0648 S \rightarrow 36\%$ leakage current.

8.2 The ZBCP in Optimally Doped YBCO: Evidence Against Presence of Magnetic Impurities in the Tunneling Barrier

The zero-bias conductance peak (ZBCP) is a robust feature observed on tunneling into [100], [110] or [103] surfaces [75,76,77,78,79,80,81,82]. Two possible origins of the ZBCP are the presence of magnetic impurities [83] in the vicinity of the barrier, and d-wave pairing [18] (see chapter 2.2.1). In the last case, for low transparency contacts, it is due to the formation of Andreev surface bound states at pair-breaking surfaces [84] (see chapter 1.2). The experimental fact, that ZBCPs are generally observed for any in-plane tunneling is not in favor of the Andreev surface bound state scenario, since it should be absent on [100] surfaces. However already a small misorientation of the [100] surface is sufficient to pick up spectral

weight at zero bias (Fig 17). In addition it has been shown that microscopic interface roughness can give rise to ZBCPs with similar spectral weight for both [110] and [100] planar tunnel junctions [85].

There are several possibilities to discriminate whether the ZBCP has its origin in magnetic impurity scattering scenario and/or in Andreev surface bound states:

| | Magnetic scattering | Surface bound states |
|---------------------------|------------------------------|----------------------------------|
| Magnetic field effect | isotropic linear splitting | anisotropic non-linear splitting |
| Density of states | suppressed in magnetic field | conserved in magnetic field |
| Tunneling | inelastic | elastic |
| Shape of ZBCP $\mu_0H=0T$ | logarithmic divergence | lorentzian distribution |

a) The strongest argument against magnetic scattering comes from the magnetic field effect:

For the first time an anisotropic magnetic field dependence of the ZBCP was measured (Fig 61), with a large field splitting, only if the magnetic field was aligned with the c-axis. This definitely rules out that the major contribution to the ZBCP has its origin in magnetic impurity scattering. Details of the field splitting and their implications for other theoretical models will be discussed later.

b) Concerning the density of states:

The magnetic field dependence of the total number of states was studied by integration of the conductance spectra between $\pm 8mV$ and normalization with the zero-field value. This was done for the two field orientations $H||c$ and $H||b$, measured in Fig 61. For both field orientations the number of states is decreasing linearly at a rate of $\sim 1\%/T$ (Fig 82). The origin of the loss of states is not clear, but it has been ruled out, that magnetic impurity scattering is at its origin, since states are lost equally over a large energy range.

However note, that there is little change in the number of states over the field range where most of the splitting occurs ($H||c$ and $\mu_0H < 0.8T$). More exactly, there is no significant anisotropy in the loss of states between $H||c$ and $H||b$. This means that the process, which induces a large field splitting, does conserve the number of states and only shifts spectral weight to higher energies.

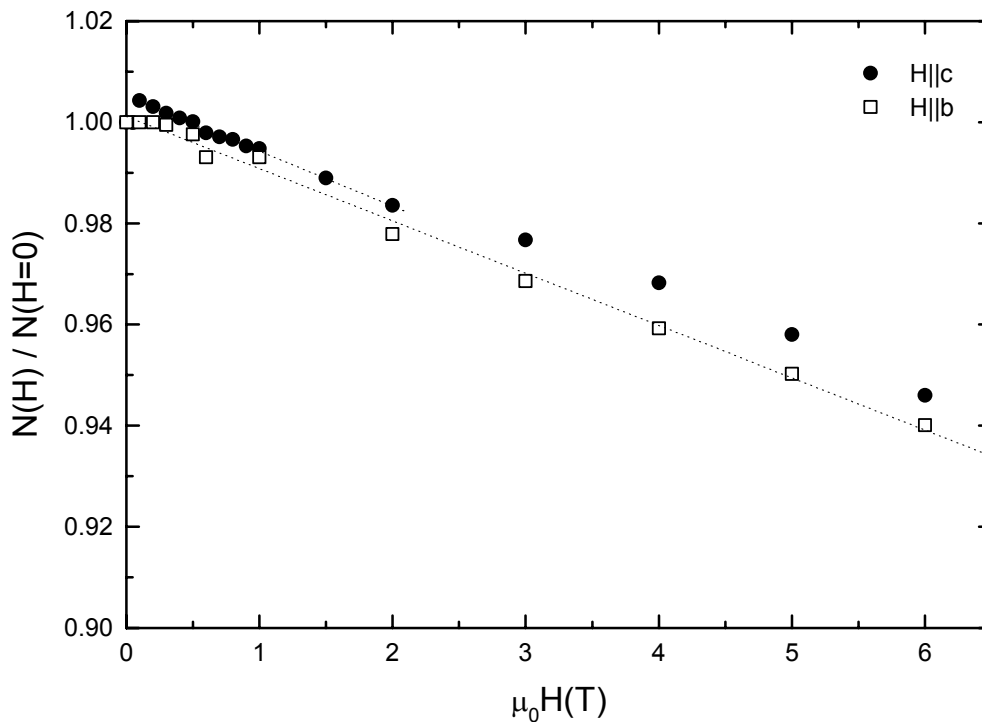


Fig 82: Magnetic field dependence of the total number of states normalized by the zero-field value from the conductance data of Fig 61.

c) Tunneling:

In chapter 8.1 it has been shown, that elastic tunneling is the major transport mechanism in the present junctions. **Since magnetic impurity scattering contributes only to inelastic tunneling the absence of inelastic tunneling is further evidence against the presence of magnetic scatterers.**

d) Shape of the ZBCP:

At low temperature, the shape of the ZBCP on In/YBCO junctions was obstructed by a zero-field splitting. Therefore the analysis of the ZBCP shape was done on Ag/YBCO junctions where no zero-field splitting is observed. Fig 83 shows, that the data could be fitted reasonably well with a Lorentzian distribution function and $\Gamma=8.2\text{mV}$. A fit to a logarithmic voltage dependence is not possible (see inset Fig 83), consistent with the absence of magnetic scattering. A Lorentzian distribution is very likely for the bound state scenario, since a bound state has a finite lifetime τ , which leads to a lifetime broadening with $\Gamma \propto \hbar / \tau$.

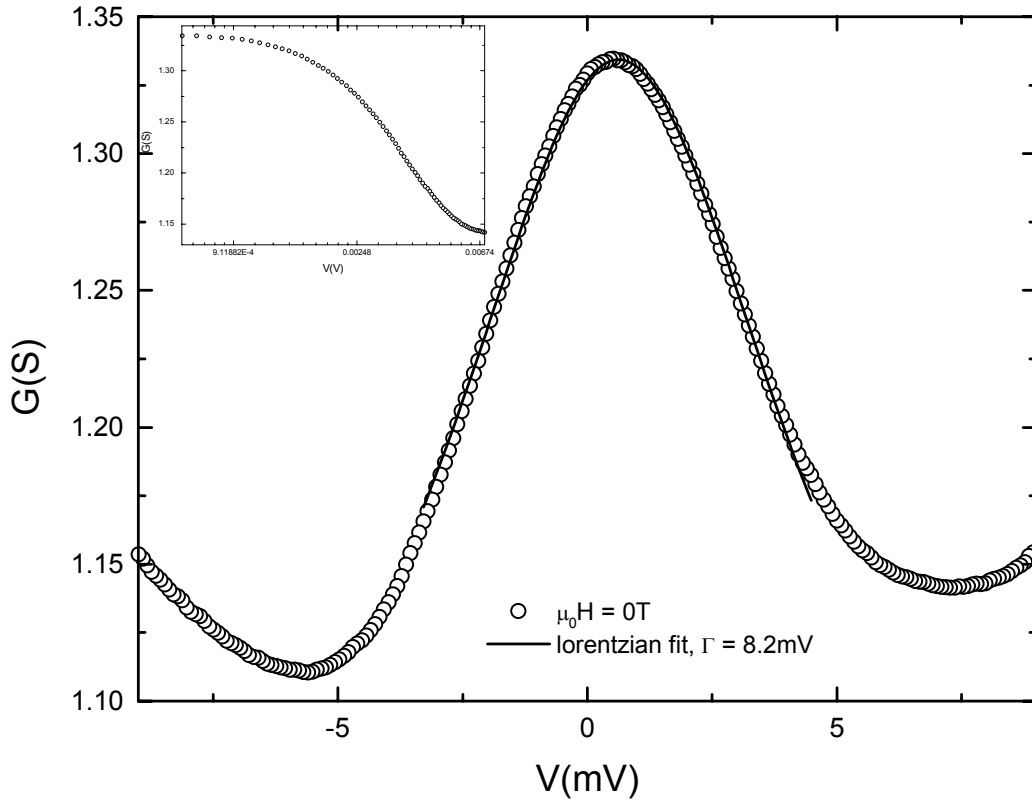


Fig 83: ZBCP of a Ag/YBCO contact in zero magnetic field . The full line is a fit to a lorentzian distribution with $\Gamma=19.2\text{mV}$. The inset shows the data at positive voltage on a ln scale.

8.3 The Field Splitting: Doppler Shifted Bound States or Induced Finite Gap ?

The field dependence $\delta(H)$, that is observed for $H||c$, is similar to that reported by Covington et al.[78] and Lesueur et al. [76]. However note some difference. First, in both studies, unlike in this work, the films were not in-plane oriented, and no anisotropy of $\delta(H)$ was observed. Second, the more detailed data of this work shows a sharp change in slope at 0.8T, from a strong field splitting regime to a weak field splitting regime. Thirdly, a finite slope ($d\delta/dH$) at large field is definitely observed. This is in contradiction with the interpretation of Covington et al. on their own data, which was fitted with a theory predicting a saturation of δ at strong fields [85]. Furthermore a large hysteresis is shown for the first time for $H||c$.

We present now a possible interpretation of the field dependence observed in this work. First, the ZBCP splitting theory of Fogelström et al.[85] is used to explain the large initial slope in the case $H||c$. Then, the hysteretic behavior will be explained in the framework of the Bean-Livingston (BL) barrier of type-II superconductors [86]. Furthermore, it will be argued that the high field small slope comes from the Pauli-field contribution. In the end, the

possibility of a magnetically induced $d_{x^2-y^2} + id_{xy}$ state is considered.

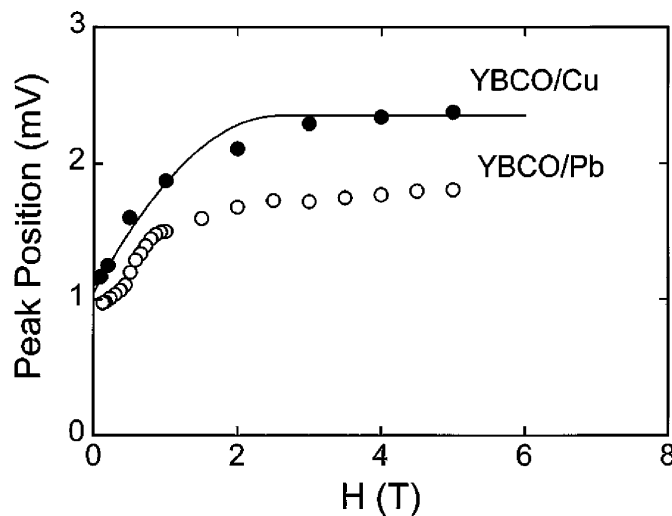


Fig 84: Magnetic field induced splitting of ZBCP's measured by Covington et al. [78] for YBCO/Cu and by Lesueur et al. [76] for YBCO/Pb junctions. The full line shows a theoretical prediction of Fogelström et al. [85].

As mentioned in chapter 1.2, d-wave symmetry of the order parameter leads intrinsically to pair-breaking at surfaces misoriented from the [100] orientation and gives rise to surface bound states, or zero-energy excitations, which are measured by tunneling as ZBCP. Fogelström et al.[85] have shown that the ZBCP should split in the presence of a magnetic field perpendicular to the CuO_2 planes ($H||c$). This splitting is due to the field induced in-plane screening currents, that shift the energy of the surface bound states by an amount of the order $\bar{v}_f \cdot \bar{p}_s$, where \bar{p}_s is the superfluid momentum and \bar{v}_f is the velocity of the bound state excitation. No such shift should occur when the field is applied parallel to the CuO_2 planes ($H||a$ or $H||b$). Precisely this anisotropy of the field splitting is shown by this experiment for the first time. It has to be stressed that the anisotropy can only be measured if the samples are in-plane oriented, as is the case in this work. In ref.76 and ref.78 samples could not be in-plane oriented due to the use of cubic substrates (see chapter 3.2). This must be the reason why anisotropic field splitting was not observed.

The electromagnetic coupling that enters the transport equation is $[-(e/c)\bar{v}_f \cdot \vec{A}(\vec{R})]$, where $\vec{A}(\vec{R})$ is the self-consistently determined vector potential. For a uniform (or slowly varying) supercurrent this coupling leads to a Doppler shift in the excitations given by $\bar{v}_f \cdot \bar{p}_s$, where $\bar{p}_s = p_s[(\hbar/2)\nabla\vartheta - (e/c)\vec{A}(\vec{R})]$. Excitations, which have a momentum component parallel or coparallel to the superflow, are shifted to higher or lower energies respectively. Therefore the current shifts the Andreev bound states spectrum. Those excitations, which are reflected at glancing angle, experience the largest energy shift. The

maximum energy shift, ε^{\max} , should be of the order of the gap $\Delta \approx 17 \text{ meV}$. It is limited by the surface currents, reaching the pair breaking current at the thermodynamical critical field $H_C = \phi_0 / \sqrt{8\pi\lambda_0\xi_0}$. Excitations, which are reflected at a larger angle, are shifted by $\varepsilon_p = \Delta \cdot (H/H_C) \cdot \sin\theta$, with θ the angle between the trajectory of the excitation and the surface normal.

This is in principle valid for all pair-breaking surfaces. However, as shown in chapter 1.2, it is only for quasiparticle trajectories with $\theta > 45^\circ - \alpha$ that zero-energy bound states are formed. E.g. for a weakly misoriented (110) surface, all trajectories form zero-energy bound states except for those at nearly perpendicular incidence, while on a weakly misoriented 100 surface, only qp reflected at glancing angle form zero-energy bound states. Assuming for the moment that tunneling is not directional it becomes immediately clear, that a field induced splitting should be easier to observe on a weakly misoriented (100) surface, since only those quasiparticles, which experience the largest shift also form the bound state. On a 110 surface however, a large fraction of the quasiparticles forming the bound state are shifted only weakly due to their small θ . This leads to a broadening of the split ZBCP.

Tunneling should be in principle directional, since finite barrier thickness favors tunneling along the interface normal. Which excitations eventually can be detected depends therefore on the barrier thickness. If the barrier is thin, the tunneling cone is large and all excitations can be measured. However, if the barrier is thick, the tunneling cone is small and only excitations with a small energy shift can be detected. Therefore the maximum shift observable in tunneling is $\delta(H) = \Delta \cdot (H/H_C) \cdot \sin\phi_C$, where ϕ_C is the angle of the acceptance cone measured from the surface normal.

From that argumentation the field splitting due to surface currents has an initial slope $(\Delta/H_C) \cdot \sin\phi_C$, which reproduces the expression of Fogelström et al. (pg.284 in ref.85) in the low field limit. With $H_C \approx 0.8 \text{ T}$ and $\Delta \approx 17 \text{ meV}$, ϕ_C has to be equal to 3.5° in order to fit the value of the large slope of the field splitting. These values are consistent with those used by Covington et al.[78] to fit their low field data. It should be recalled, that an important condition to observe the splitting is that the tunnel junction has a low-transmission. Only then the surface barrier is strong and Andreev bound states are well defined. A small value for ϕ_C is therefore expected. However a small value for ϕ_C also excludes the possibility that the observed field splitting originates from weakly misoriented (100) surfaces.

If the low field splitting has indeed its origin in Doppler shifted bound states it must come from excitations reflected on (110) facets, which are probably present due to

surface roughness. It is important to note, that on in-plane oriented samples all (110) facets are parallel to the (001) direction. The observed anisotropic field splitting would therefore still be consistent with the Doppler shift scenario.

The observed field splitting crosses over from a strong field dependence to a weak field dependence, if the field variation is larger than $\Delta H^* \sim 0.8T$. This value is of the order of the BL barrier field, observed in $Y_1Ba_2Cu_3O_7$ [87]. **Therefore a reasonable explanation for the crossover and the hysteresis would be, that once vortices can enter the superconductor, a further field increase does not modify the surface current and a further splitting of the ZPCP does not occur. In decreasing fields, vortices do not exit if the field is reduced by less than ΔH^* .** In that range the surface current decreases, and so does the splitting. This observation was not predicted by Fogelström et al. Another observation that does not fit the predictions of Fogelström et al., is that the field splitting does not saturates at high field, but rather shows a weak field dependence with a slope of approximately $0.1\text{meV}/T$. According to Fogelström et al., a saturation should occur at $H \sim 3 \cdot H_C$. Instead, the slope is close to $\delta(H)/H = g\mu_B = 0.1158\text{mV}/T$, predicted for the Zeeman splitting of electrons with $g = g_{\text{electron}} = 2$. **It has to be concluded, that the weak field dependence seen at strong applied fields is caused solely by Zeeman splitting.** This statement is reinforced by the fact, that similar slopes are measured with $H \parallel a$ and $H \parallel b$, where no strong field dependence is observed and field splitting due to supercurrents does not occur, and is not expected. It has to be pointed out, that the high field data of ref.[76] and [78] can be linearly fitted with a similar slope, which is consistent with our interpretation of a universal Zeeman splitting.

In conclusion it can be said, that the anisotropy of the field splitting at low fields is consistent with the idea of Doppler shifted zero-energy bound states. However the observed hysteresis and the sharp crossover at $\mu_0 H = 0.8T$ are only plausible if a large BL-barrier is present. At high field, the strongly increasing splitting is presumably a Zeeman splitting, not predicted by the Fogelström theory.

Concerning the abrupt crossover at $\mu_0 H = 0.8T$, it important to consider, that there is a striking similarity to an experiment on the thermal conductivity of $Bi_2Sr_2CaCu_2O_8$ in a magnetic field by Krishana et al. [13]. At $T = 6K$, the thermal conductivity decreases linearly as the field is increased and at $\mu_0 H = 0.6T$, the conductivity shows a sudden cross-over to a constant value regime (Fig 85). If there is a connection between Krishana's experiment and

this tunneling experiment, it has to be due to a bulk effect, since the thermal conductivity is a bulk property.

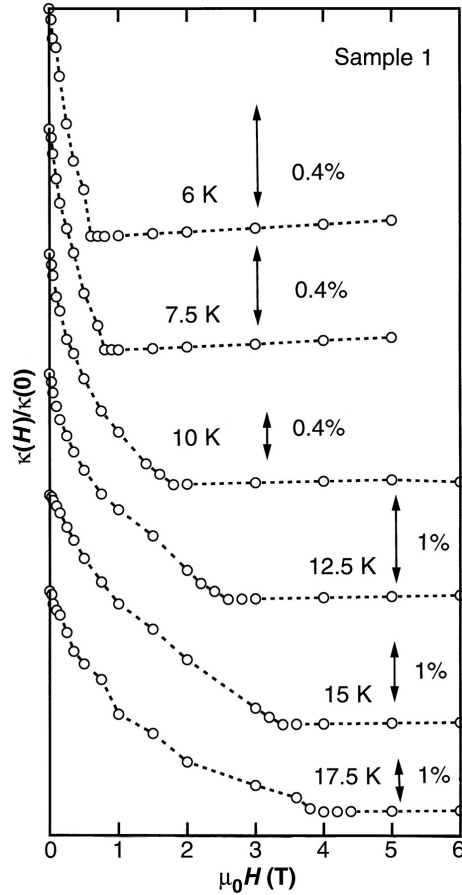


Fig 85: The H dependence of the thermal conductivity below $T=20K$ ($H||c$) measured by Krishana et al. [13]. The slight positive slope reflects the weak magnetoresistance of the thin-film heaters.

The experiment of Krishana et al. was given a theoretical explanation by Laughlin [14]. Laughlin claims, that the transition observed in the thermal conductivity experiment is consistent with a field induced complex order parameter of the form $d_X^2 - Y^2 + id_{XY}$, with the following field dependence in the zero-temperature limit:

$$|i\Delta_{XY}| \approx 1.64 \frac{\text{mV}}{\text{Tesla}^{1/2}} \cdot \sqrt{B}$$

The effect should be anisotropic, with the id_{XY} component induced only if $H||c$. This is consistent with the work of Krishana et al., who have reported a qualitatively different and much weaker field dependence when H is in-plane aligned. Krishana has also observed a magnetic hysteresis [88].

If Krishana's data and the tunneling in this work have to be interpreted within the

framework of an induced id_{XY} component, one may come to the following conclusion: As the magnetic field is increased a id_{XY} component is induced which causes the opening of a finite gap. As the finite gap opens, the thermal conductivity decreases and the bound states are shifted to higher energies (see Fig 6, Fig 7 and Fig 18). At H^* , a maximum gap is induced and the induced gap does not further increase at higher fields. As a consequence the thermal conductivity is constant and the field splitting of the ZBCP is constant as well, except for the generally observed Zeeman splitting. This effect should be present only if $H||c$ in agreement with the experiments. The hysteresis however is difficult to understand. Also, Laughlin does not predict a maximum induced gap.

It is important to note that for directional planar tunneling (thick barrier) the id_{XY} component can be measured only on (110) facets, whereas for non-directional tunneling (thin barrier) the full gap is detectable also on weakly misoriented (100)-surfaces (Fig 18).

The low field splitting has been fitted to both the theory of Doppler shifted zero-energy bound states bound states and to the theory of a field induced id_{XY} gap [89]. Both theories can fit the data well, however the Laughlin prediction has no free parameter, except for an additional constant which accounts for the zero-field splitting, where as the Fogelström theory needs two parameters plus a zero-field splitting constant:

a) the Doppler shift according to Fogelström et al. [85]:

$$\delta(H) = \delta_s + \frac{17\text{mV} \cdot \mu_0 H}{H_0} \cdot \left[1 - \frac{1}{2} \left(\frac{H}{H_c^*} \right) \right],$$

$$\text{with } \delta_s = 1.02\text{mV} \quad \mu_0 H_0 = 13.5\text{T} \quad \text{and} \quad \mu_0 H_c^* = 6.3\text{T}$$

b) the Laughlin prediction [14] with the ad-hoc assumption of an additional constant δ_s :

$$\delta(H) = \delta_s + \frac{1.64\text{mV}}{\text{Tesla}^{1/2}} \sqrt{\mu_0 H}, \quad \text{with } \delta_s = 0.46\text{mV}$$

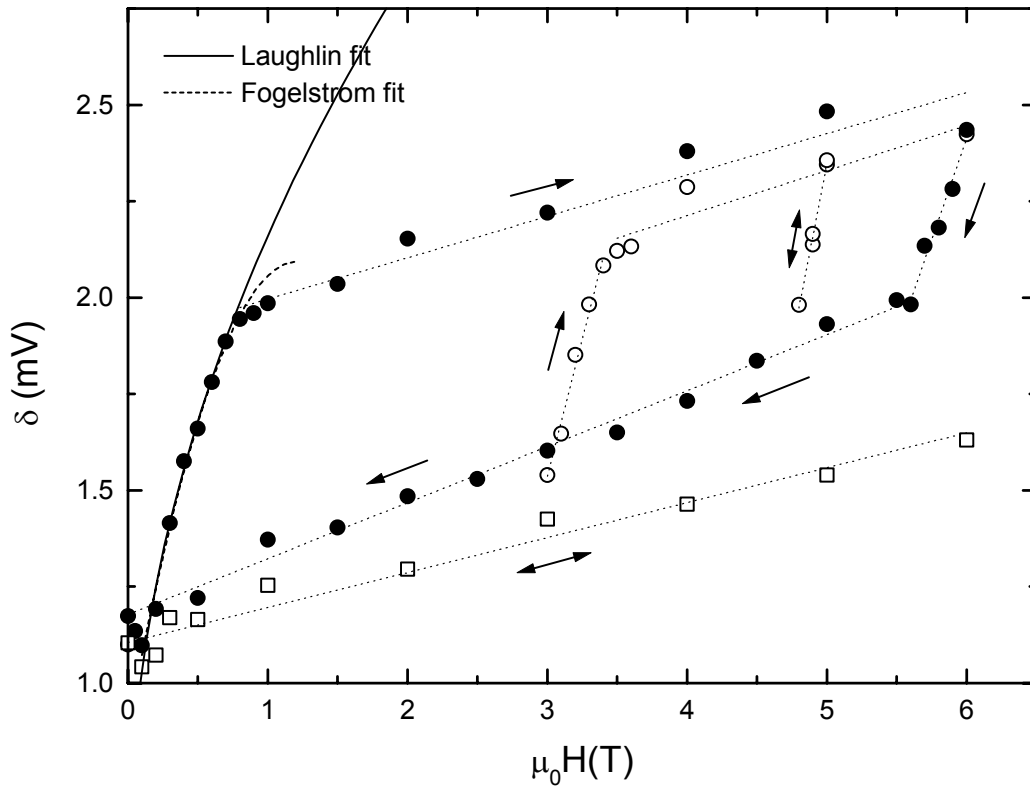


Fig 86: Fit of the low field data, for $H||c$ (●), to the theory of Laughlin (—) [14] and Fogelström et al. (---) [85].

There is further evidence for a close correlation between the Krishana's experiment and this work from the temperature dependence of the crossover field H^* , which has been studied in chap. 7.3. As the temperature is reduced from $T=4.2\text{K}$ to $T=1.5\text{K}$, H^* is reduced from $\mu_0 H^*=0.5\text{T}$ to $\mu_0 H^*=0.3\text{T}$. Such a strong reduction is difficult to reconcile with the temperature dependence of the BL barrier, which should *increase* or at least stay constant with decreasing temperature. It is however similar to the temperature dependence of the transition field observed by Krishana et al. (Fig 85).

Finally, an experimental and a theoretical study of bound states in vortices have to be mentioned, which are in favour of a field induced id_{XY} component in YBCO. Franz and Tešanović have calculated the quasiparticle spectrum of an isolated vortex in a d-wave superconductor [90]. For a pure $d_{x^2-y^2}$ superconductor, they found that there exist no bound states in the vortex core, since all states are extended due to nodes in the energy gap. This is inconsistent with existing data of Maggio-Aprile et al. [91] on YBCO, where a bound state was found within the vortex core at $\sim 5.5\text{mV}$ (Fig 88). Franz et al proposed therefore, that the existence of that bound state is due to the magnetic field induced $d_{x^2-y^2} + id_{XY}$ state in YBCO.

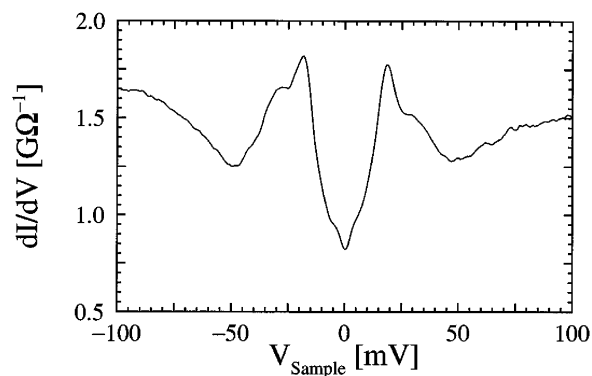


Fig 87: Conductance spectrum of the [001]-surface of a YBCO single crystal at $T=4.2K$, $\mu_0H=0T$

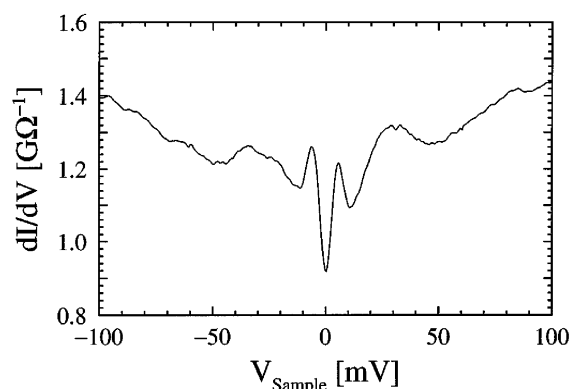


Fig 88: Conductance spectrum of the vortex core at $\mu_0H=6T$ and $H||c$ ($T=4.2K$, [001]-surface of YBCO crystal)

It is interesting to note, that the bound state within the vortex core appears at an energy not much larger than the energy, at which a ‘sub-gap’ feature appears in the zero-field conductance. This sub-gap feature is inconsistent with non-directional c-axis tunneling into a pure $d_{x^2-y^2}$ superconductor (Fig 17a, curve C and D). It is however consistent with the existence of a $d_{x^2-y^2} + is$ or $d_{x^2-y^2} + id_{xy}$ already in zero magnetic field (Fig 18a and Fig 18e, respectively for $Z=5$). This is very important for the following discussion about the origin of the zero-field splitting.

8.4 The Zero-Field Splitting

Surface pair breaking frees up spectral weight at the Fermi surface. If a subdominant pairing channel, which is only weakly modified by the surface, exists, pairs can condensate into that channel. The relevance of a subdominant order parameter depends on the microscopic pairing interaction. For example the electron-phonon interaction may lead to a sub-dominant pairing interaction in the A_{1g} channel (anisotropic s-wave) on the 110 surface of a d-wave superconductor, causing a $d_{x^2-y^2} + is$ surface phase. Also possible would be a $d_{x^2-y^2} + id_{xy}$ surface phase, since the (110) surface is not pair-breaking for the id_{xy} component either.

For both complex order parameters a small finite gap $\Delta = |id_{xy}|$ or $\Delta = |is|$ appears in the angular dependence of the gap amplitude, and the $d_{x^2-y^2}$ nodes are removed (Fig 6 and Fig 10). The effect on the conductance spectra depends on the specific tunneling experiment:

For non-directional tunneling, on a perfect (001)- or (100)- surface, a dip in the conductance spectrum should appear at $\Delta = |id_{xy}|$ or $\Delta = |is|$ (Fig 18a+e). In fact, dips have been seen in the STM data of Maggio-Aprile et al. [91] shown in Fig 87 and by J.M. Valles et al. [92] as well.

For tunneling into pairbreaking surfaces, the finite gap should split the ZBCP, with a splitting $\delta = |is|$ and $\delta = |id_{XY}|$ for $d_X^2 - Y^2 + is$ and $d_X^2 - Y^2 + id_{XY}$, respectively, as observed in this experiment. **However it is important to note, that ZBCP splitting due to the $d_X^2 - Y^2 + id_{XY}$ symmetry can be observed only by directional tunneling into (110) surfaces, for non-directional tunneling the ZBCP is not split but broadened by $|id_{XY}|$ (Fig 18f-h).**

On the basis of this work it can not be distinguished whether the observed zero-field splitting is due to $d_X^2 - Y^2 + is$ or $d_X^2 - Y^2 + id_{XY}$ ordering. **However a split ZBCP in zero magnetic field always proves the presence of a complex order parameter. Only with a complex order parameter it is possible to realize a small finite gap under conservation of an angular dependent phase** (see Fig 6 - Fig 13 and chapter 1.2). The observed splitting is of the order of 6% of the large d-wave gap and can be regarded as a small perturbation.

In this work, zero-field splitting is usually observed below $T=6K$ on optimally doped In/YBCO junctions. This is similar to the work of Geerk et al.[75] and Kashiwaya et al.[80], where zero-field splitting is observed at $T=4.2K$ as well. Yet Covington et al.[78] reports zero-field splitting only below $T=4.2K$, and in the case of Ag/YBCO, no zero-field splitting is observed down to 1.5K.

It is possible that the temperature, at which the zero-field splitting appears, depends on the degree of nanofacetting. Rainer et al.[21]. has shown, that the measurable finite gap, especially of a $d_X^2 - Y^2 + id_{XY}$ order parameter, closes rapidly with surface roughness. Finally for very rough surfaces the limit of non-directional tunneling is reached (Fig 18f-h).

However another parameter that varies with the kind of contact is the level of oxygen doping [70]. If the zero field splitting is attributed to a sub-dominant s-wave or d_{XY} -wave order parameter, its strength may be doping dependent. This has not been predicted theoretically.

Finally it has to be noted, that a large field splitting has also been observed on a sample without zero-field splitting (Fig 63).

8.5 The Doping Dependence

On underdoped YBCO no zero-field splitting of the ZBCP is observed down to $T=4.2\text{K}$. Neither is a strong field splitting of the ZBCP observed. Only a weak, isotropic field splitting of the order of the Zeeman splitting is seen (Fig 64 - Fig 66).

These findings are difficult to reconcile with the theory of Fogelström et al, which predicts, that a ZBCP should generally split in a magnetic field. But it is also difficult to reconcile with the theory of Laughlin, where an id_{xy} component should generally evolve in a d-wave SC.

However possibly the field splitting, as well as the zero-field splitting, is doping dependent and not observable in the underdoped regime. For instance on grain boundary junctions, which are known to be underdoped [93], a direct splitting of the ZBCP has never been observed [82]. Also the half-flux quantum experiment of Tsuei and Kirtley performed on tricrystal grain boundary junctions suggest pure $d_{x^2-y^2}$ with an uncertainty of $\pm 10\%$ [94].

The absence of a zero-field splitting is consistent with the generally accepted pure $d_{x^2-y^2}$ order parameter in underdoped YBCO.

On overdoped Ca-YBCO no ZBCP is observed at any temperature (Fig 68). Instead an additional sub-gap, appears below $T=12\text{K}$. This implies that over a large temperature range nodes are absent and that the order parameter is different from pure $d_{x^2-y^2}$ symmetry.

The fact that the field dependence of the sub-gap on Ca-YBCO is similar to the field dependence of the ZBCP on optimally doped YBCO points to a common physical mechanism (Fig 71, Fig 62).

Finally we report a value for the larger gap in Ca-YBCO. As seen in Fig 65, the raw data is often difficult to analyse due to a voltage dependent background. In [95] we presented a procedure, which is useful to determine the energy of the superconducting gap more accurately. The idea is to subtract the spectrum measured in a magnetic field from the zero field spectrum. At the energy of the superconducting gap the conductance is reduced, where as normal state features, which are not affected by the field, simply cancel out. As this procedure is applied on Ca-YBCO, a dip appears at the energy of the superconducting gap $\Delta=11\text{mV}$ (Fig 89). Note that in the subtraction presentation, the field splitting of the ZBCP and the widening of the sub-gap show up as a shift of spectral weight from zero energy to higher energy. The spectral weight appears to be shifted to higher energies than the real splitting of the ZBCP. This is however an artefact due to the subtraction procedure, which

depends intrinsically on the specific shape of the ZBCP.

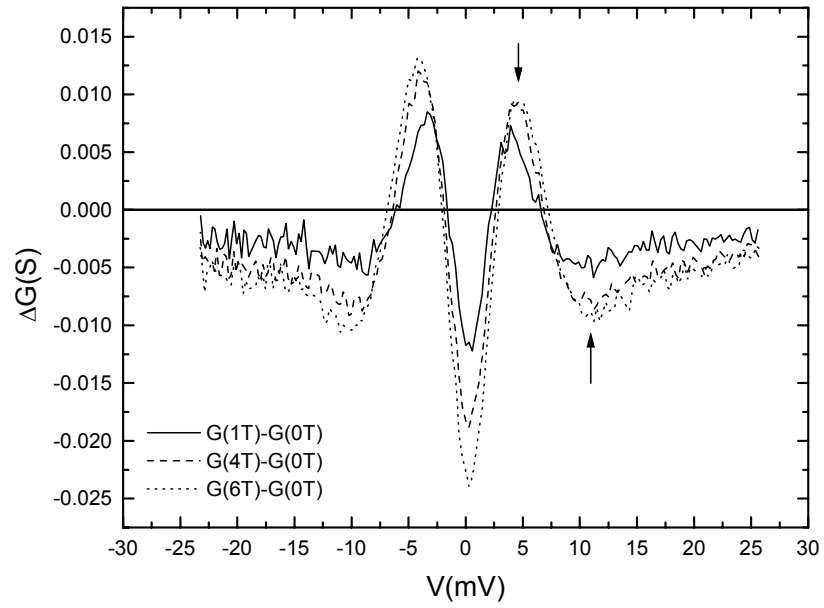


Fig 89: $G(H)-G(0T)$ for overdoped Ca-YBCO, $\Delta = 11mV$.

9 Conclusion

Tunneling spectroscopy was performed on in-plane oriented (100)-YBCO films. It was shown unambiguously that the zero-bias conductance peak, observed on these films, is due to the presence of Andreev surface bound states and not to magnetic scattering in the barrier. Since the energy of Andreev bound states depends on the phase of the order parameter, tunneling into Andreev bound states is a phase sensitive measurement.

On that basis, the data is evidence that the order parameter at least at the surface changes as a function of temperature and doping. For underdoped samples the symmetry is pure $d_{x^2-y^2}$ -wave at low temperatures down to $T=4.2\text{K}$. On optimally doped samples a transition is observed at $T'=6\text{K}$ from pure $d_{x^2-y^2}$ -wave to a complex order parameter below T' . On overdoped samples the order parameter is complex at least up to $T'=12\text{K}$. The specific symmetry of the complex order parameter is unknown but probably either $d_{x^2-y^2} + id_{xy}$ or $d_{x^2-y^2} + id_{xy}$.

The magnetic field dependence was studied for different field orientations. For the first time, an anisotropic field splitting of the ZBCP has been observed. The splitting is strong only when the field is applied perpendicular to the CuO_2 planes ($H||c$). This observation alone can be explained either by an increase of the Andreev bound state energy by a Doppler shift or by a magnetically induced finite gap.

However the absence of a strong field splitting on the underdoped samples and the anisotropic field enhancement of the sub-gap in overdoped samples are difficult to reconcile with theoretical predictions. A magnetically induced $d_{x^2+y^2} + id_{xy}$ order parameter may resolve this difficulty, if the ability to induce the id_{xy} component is doping dependent. This has not been predicted.

Above a field $\mu_0H \sim 0.8\text{T}$, a large hysteresis of the field splitting is observed for $H||c$ in optimally and overdoped samples, with a sharp transition into a weak splitting regime. Possibly this can be understood only within the framework of a Doppler shift scenario and the presence of a BL barrier for vortex penetration. It can not be reconciled with a magnetically induced $d_{x^2+y^2} + id_{xy}$ ordering. Where the field splitting is weak it has been identified as due to Zeeman splitting.

Acknowledgements

I am grateful to my supervisor, Prof. Guy Deutscher, for giving me the opportunity to research in this exciting field and for sharing his deep physical insight and experience. I also appreciate very much his kindness and many discussions beyond physics.

For the pleasant work environment and many discussions I would like to thank all colleagues and friends, especially Dr. Tamir Ben David, Eli Farber, Dr. Isabelle Okashi- Djournio, Yoram Dagan, Amir Kohen, Lee Nehoshtan and Jose Luis Azar. Mishael Azoulay I would like to thank in addition for his tireless technical assistance.

I am also grateful to Dr. Zahava Barkay for her professional work in the Wolfson Material Center, Haim Bachar and Olivier Kohen for the supply of liquid helium, and to many others from the University staff including Chava Belson.

Finally I want to thank my parents, my friend Dagmar, my brother Carsten, my grandparents and all friends for their support and patience.



10 References

- [1] G. Deutscher, *Nature* 397 (1999) 410
- [2] D.J. Scalapino, *Phys. Rep.* 250, 329 (1995)
- [3] C.C. Tsuei and J.R. Kirtley, *Physica C* 282-287, 4 (1997)
- [4] J. Bardeen, L.N. Cooper, J.R. Schrieffer, *Phys. Rev.* 108 (1957) 1175
- [5] L.J. Buchholtz et al., *J. Low Temp. Phys.* 101 (1995) 1079
- [6] S. Kashiwaya et al., *Jpn. J. Appl. Phys. Vol. 34* (1995) 4555
- [7] J. Ma et al., *Science* 267, 862 (1995)
- [8] M. Moessle and R. Kleiner, *Phys. Rev. B* 59, 4486 (1999)
- [9] C. Kendziora, R.J. Kelley, and M. Onellion, *Phys. Rev. Lett.* 77, 727 (1996)
- [10] M. Covington et al., *Phys. Rev. Lett.* 79, 277 (1997)
- [11] V.L. Ginsburg and L.D. Landau, *Zh. Eksp. Teor. Fiz.* 20, 1044 (1950)
- [12] M. Sigrist, D.B. Bailey, R.B. Laughlin, *Phys. Rev. Lett.* 74, 3249 (1995)
- [13] K. Krishana et al., *Science* 277, 83 (1997)
- [14] R.B. Laughlin, *Phys. Rev. Lett.* 80, 5188 (1998)
- [15] I. Maggio-Aprile et al., *Phys. Rev. Lett.* 75, 2754 (1995)
- [16] G. Blonder, M. Tinkham, T. Klapwijk, *Phys. Rev. B.* 25, 4515 (1982)
- [17] S. Kashiwaya, Y. Tanaka et al., *Phys. Rev. B* 51, 1350 (1995)
- [18] Y. Tanaka and S. Kashiwaya, *Phys. Rev. Lett.* 74 (1995) 3451
- [19] Chr. Bruder, *Phys. Rev. B* 41 (1990) 4017
- [20] Y. Dagan et al., submitted to *Phys. Rev. B* (April 1999)
- [21] D. Rainer et al., *J. Phys. Chem Solids* 59 (1998) 2040
- [22] J.D. Jorgensen et al., *Phys. Rev. B* 41 (1990) 1863, Batlogg et al., *Novel Superconductivity* ed. by Wolf & Kresin
- [23] Y. Tokura et al., *Phys. Rev. B* 38, 7156 (1988)
- [24] C. Bernhard and J.L. Tallon, *Phys. Rev. B* 54 (1996) 10201
- [25] *Handbook of thin film phenomena*, L.I. Maisel, R. Glang, McGraw-Hill (1969)
- [26] S. Poelders, Diplomarbeit 1994, Kernforschungszentrum Karlsruhe
- [27] G.M. Pound, H. Karge in *Grundprobleme der Physik duenner Schichten* ed. R. Niedermayer, H. Mayer, 19-28, Vandenhoeck u. Ruprecht, Goettingen (1966)
- [28] T. Burmann et al., *Solid State Communications*, Vol. 90, No. 9, p. 599-602 (1994)
- [29] U. Jeschke et al., Diplomarbeit 1994, Kernforschungszentrum Karlsruhe
- [30] S. Hontsu et al., *Appl. Phys. Lett.* 61 (9) 1134

References

- [31] B. Roas, L. Schultz, G. Endres, Appl. Phys. Lett. 53 (1987) 1557
- [32] A.D. Berry et al., Phys. Rev. B 35
- [33] R.B. Laibowitz et al., Phys.Rev.B35 (1987) 8821
- [34] J.Geerk, G. Linker, O. Meyer, Mat. Sci. Rep. 4 (1989) 193
- [35] R. Behrisch: Festkoerperzerstaeubung durch Ionenbeschuss aus Ergebnisse der exakten Naturwissenschaften, Band 35, Springer-Verlag
- [36] J.D. Wasscher, Philips Res. Repts 16, 301-306, 1961
- [37] Mathcad 5.0 Plus, Math Soft Inc.
- [38] Thin film technology handbook / Aicha Elshabini, Fred D. Barlow. McGraw-Hill (1998)
- [39] R. Krupke, Z. Barkay, G. Deutscher, Physica C 289 (1997) 146-150
- [40] J.R. Gavaler et al., J. Appl. Phys. 70 (1991) 8
- [41] E.J. Cukauskas et al., IEEE Trans. Appl. Supercond. 3 (1993) 1
- [42] K. Verbist, A.L. Vasiliev, G. Van Tendeloo, Appl. Phys. Lett. 66 (1995) 11
- [43] V. Matijasevic et al., J. Mater. Res. 6 (1991) 682
- [44] R. Krupke, Z. Barkay, G. Deutscher, Physica C 315 (1999) 99-106
- [45] R. Krupke, Z. Barkay, G. Deutscher, Physica C 317-318 (1999) 536-539
- [46] Ph. Lecœr, B. Mercey, H. Murray, J.Appl. Phys. 78 (1995) 1247
- [47] F. Kaufmann, J.R. Kelso, Chem. Phys. 32 (1960) 301
- [48] M.D. Costa, P.A. Zuliani, J.M. Deckers, Can. J. Chem. 57 (1979) 568
- [49] J.R. Gavaler et al., J. Appl. Phys. 70 (1991) 8
- [50] G.S. Anderson, Wm.N. Mayer, G.K. Wehner, J. Appl. Phys. 33 (1962) 2991
- [51] R.J. Cava et al., Phys. Rev. B 36 (1987) 5719
- [52] Goldstein et al., Scanning Electron Microscopy and X-ray Microanalysis, Plenum, 1992
- [53] T.B. Lindemer et al., Physica C 178 (1991) 93
- [54] J.D. Jorgensen et al., Phys. Rev. B 41 (1990) 1863
- [55] G. Linker et al., Nucl. Instrum. und Meth. B 59-60 (1991) 1458
- [56] R. Schneider et al., Physica C 220 (1994) 165-171
- [57] R. Krupke et al., Physica C 279 (1997) 153
- [58] A.P. Shapovalov et al., Supercond. Sci. Technol. 5 (1992) 238
- [59] D.K. Aswal et al., Thin Solid Films 292 (1997) 277
- [60] Y. Tazoh, S. Miyazawa, Appl. Phys. Lett. 62 (1993) 408
- [61] C.C. Chang et al, Appl. Phys. Lett. 57 (1990) 1814
- [62] Z. Han, T.I. Selinder, U. Helmersson, J. Appl. Phys. 75 (1994) 2020
- [63] D. Fuchs et al., Physica C, 280 (1997) 167

-
- [64] A.A. Abrikosov, *Physica C* 317-318 (1999) 154-174
- [65] A. Goyal et al, *Appl. Phys. Lett.* 69 (12) (1996) 1795
- [66] F.A. List et al., *Physica C* 302 (1998) 87-92
- [67] Q. He et al., *Physica C* 275 (1997) 155-161
- [68] A. Gerber et al., *Phys. Rev. B* 43 (1991) 12935
- [69] W.R. Flawell et al., *J. Alloys and Compounds* 195 (1993) 535
- [70] D. Racah and G. Deutscher, *Physica C* 263 (1996) 214
- [71] Z.H. Gong et al., *Appl. Phys. Lett.* 63 (1993) 836
- [72] A.L. Vasiliev et al., *Physica C* 244 (1995) 373-388
- [73] J.M. Rowell, *Tunneling Phenomena in Solids*, 1967 NATO advanced Study Institut at Risø, Denmark, 1969 Plenum Press
- [74] R. Krupke and G. Deutscher, *Phys. Rev. Lett.* 83, 4634 (1999)
- [75] J. Geerk, X.X. Xi, G. Linker, *Z. Phys.* **73**, 329(1988)
- [76] J. Lesueur, L.H. Greene, W.L. Feldmann, A. Inam, *Physica C* **191**, 325 (1992)
- [77] M. Covington et al., *Appl. Phys. Lett.* 68, 1717 (1996)
- [78] M. Covington et al., *Phys. Rev. Lett.* **79**, 277 (1997)
- [79] M. Aprili et al., *Phys. Rev. B* 57, 57 (1998)
- [80] S. Kashiwaya et al., *J. Phys. Chem. Solids* 59, 2034 (1998)
- [81] J.Y.T. Wei et al., *Phys. Rev. Lett.* 81, 2542 (1998)
- [82] L. Alff et al., *Phys. Rev. B* 58, 1197 (1998)
- [83] J.A. Appelbaum, *Phys. Rev.* **154**, 633 (1967)
- [84] C.-R. Hu, *Phys. Rev. Lett.* **72**, 1526 (1994)
- [85] M. Fogelström, D. Rainer, J.A. Sauls, *Phys. Rev. Lett.* **79**, 281 (1997)
- [86] C.P. Bean et al., *Phys. Rev. Lett.* **12**, 14 (1964)
- [87] S. Tochihara, H. Yasuoka, H. Mazaki, *Physica C* 312 (1999) 28
- [88] K. Krishana et al., *Science* **280**, 9a (1998)
- [89] Y. Dagan, R. Krupke and G. Deutscher, 'Possible evidence for id_{xy} order in (110) YBCO films' submitted to *Europhys. Lett.* (2000)
- [90] M. Franz and Z. Tešanović, *Phys. Rev. Lett.* 80 (1998) 4763
- [91] I. Maggio-Aprile et al., *Phys. Rev. Lett.* 75 (1995) 2754
- [92] J.M. Valles et al., *Phys. Rev. B* 44 (1991) 11986
- [93] C.W. Schneider et al., *Appl. Phys. Lett.* 75, 850 (1999)
- [94] J.R. Kirtley and C.C. Tsuei, preprint (1999)
- [95] Y. Dagan, R. Krupke and G. Deutscher, submitted to *Phys. Rev. B* (2000)